Helical Magnetic Structure and Transport Properties in epitaxial B20 Fe$_{1-x}$Co$_x$Ge films

Charles Steven Bolanos Spencer

University of Leeds

School of Physics and Astronomy

Submitted in accordance with the requirements for the degree of

Doctor of Philosophy

May, 2018

Intellectual Property Statement

The candidate confirms that the work submitted is his own and that appropriate credit has been given where reference has been made to the work of others.

This copy has been supplied on the understanding that it is copyright material and that no quotation from the thesis may be published without proper acknowledgement.

The right of Charles Steven Bolanos Spencer to be identified as Author of this work has been asserted by him in accordance with the Copyright, Designs and Patents Act 1988.

Work from the following jointly authored publication is presented in chapters four and five:

Nicholas A. Porter, **Charles S. Spencer**, Rowan C. Temple, Christian J. Kinane, Timothy R. Charlton, Sean Langridge, and Christopher H. Marrows, Manipulation of the spin helix in FeGe thin films and FeGe/Fe multilayers, Phys. Rev. B **92**, 144402 (2015).

Work attributable to candidate: Growth of FeGe/Fe sample, data analysis and simulations.

Work attributable to other authors: N. Porter produced the FeGe sample (This sample is further studied in this thesis) and XRD and magnetometry. N. Porter, R. Temple, C. Kinane, T. Charlton, S. Langridge performed the PNR measurements. N. Porter and C. Marrows writing of manuscript.

Work from the following jointly authored publication is presented in chapters four and five and six:

Charles S. Spencer, Jacob Gayles, Nicholas A. Porter, Satoshi Sugimoto, Zabeada Aslam, Christian J. Kinane, Timothy R. Charlton, Frank Freimuth, Stanislav Chadov, Sean Langridge, Jairo Sinova, Claudia Felser, Stefan Blügel, Yuriy Mokrousov, and Christopher H. Marrows, Helical magnetic structure and the anomalous and topological Hall effects in epitaxial B20 $Fe_{1-x}Co_xGe$ films, arXiv:1803.03281 (2018).

Work attributable to candidate: Growth of $Fe_{1-x}Co_xGe$ samples, experimental work including structural, magnetic, PNR and electronic transport measurements. Analysis of experimental results and manuscript writing.

Work attributable to other authors: J. Gayles: theoretical studies including DFT calculations and theoretical interpretation of experimental data and writing of manuscript. C. Marrows: results analysis and manuscript writing.

Y. Mokrousov: theoretical interpretation of data and manuscript writing. N. Porter: growth of FeGe sample. S. Satoshi: PNR measurements and device fabrication. Z. Aslam: TEM measurements. C. Kinane, T. Charlton and S. Langridge: PNR measurements and data interpretation. F. Freimuth, S. Chadov, J. Sinova, C. Felser, S. Blügel: theoretical interpretation of data.

Acknowledgements

Abstract

We have grown epitaxial single-phase B20 $Fe_{1-x}Co_xGe$ films on Si (111) substrates films by molecular beam epitaxy. This method is able to produce the whole range of $Fe_{1-x}Co_xGe$ which are of high quality due to homogeneous layer growth with low surface roughness of 1-2 nm. The films grown are racemic, showing an equal mix of left-handed and right-handed chiral grains, and are strained due the lattice mismatch between the film and substrate.

Magnetic measurements showed the FeGe films grown ($\sim$ 70 nm thickness) have a saturation moment, $M_s = 0.982(7)$ μ_B, and ordering temperature, $T_c = 280(2)$ K, both close to bulk value. M_s and T_c were found to decrease monotonically with increasing x and all films were found to have an easy-plane anisotropy. A helical magnetic structure was observed using polarised neutron reflectometry and we found the helix wavelength to vary with composition. A divergence in the wavelength was found at a critical composition $x_c = 0.5$ where a transition from helimagnet to collinear ferromagnet occurred.

The temperature dependent resistivity, $\rho_{xx}(T)$, was found to be metallic for all compositions and a broad peak with magnetic origin was found to arise for intermediate compositions $0.2 \leq x \leq 0.7$. The magnetoresistance in $Fe_{1-x}Co_xGe$ with $0.1 < x < 1$ was found to behave similarly to FeGe, however many differences were observed, such as a positive linear magnetoresistance for $Fe_{0.4}Co_{0.6}Ge$ and a change in conical magnetoresistance scaling beyond $Fe_{0.5}Co_{0.5}Ge$. The Hall resistivity showed an increase as well as a sign change in the ordinary Hall effect coefficient, R_0, from 0.0122 $\mu\Omega$ cm/T for FeGe to -0.6808 $\mu\Omega$ cm/T for $Fe_{0.5}Co_{0.5}Ge$, at 5 K, indicating a large reduction in the carrier concentration and change of carrier type. The anomalous Hall effect was found to increase dramatically on the introduction of Co, increasing by an order of magnitude from FeGe to $Fe_{0.9}Co_{0.1}Ge$ at 5 K.

We find evidence of potential skyrmion structures through the measurement of the topological Hall effect, with features as large as -0.39 $\mu\Omega$ cm for $Fe_{0.6}Co_{0.4}Ge$ at 5 K. We conclude $Fe_{1-x}Co_xGe$ is a potential material for further skyrmion study, but direct observation of these topological structures are required to fully attribute the measured effect and progress further.

CONTENTS

List of Figures

List of Tables

Chapter 1

Introduction

1.1 Overview

B20 $Fe_{1-x}Co_xGe$ is a cubic chiral helimagnet that is host to the Dzyaloshinskii-Moriya interaction due to the lack of inversion symmetry in the crystal unit cell. This interaction has been observed to stabilise the formation of magnetic skyrmions which are currently of great interest [1]. These magnetic objects are topologically stable spin structures that have particle-like properties, which make them promising for applications in spintronics, such as novel racetrack memory devices [2]. To realise these skyrmion-based devices and applications, thin films are required and here we explore the possibility of $Fe_{1-x}Co_xGe$ for such applications by examining its magnetic and electron transport properties.

In this chapter we will examine the history of research into the B20 silicide and germanide materials and how the discovery of the magnetic skyrmion in these materials has generated a huge interest in them.

We will then look at how growth of films has been achieved and the effects of moving from bulk crystal to film.

1.2 History of research in B20 materials

The B20 3d transition metal (TM) silicides and germanides have been the subject of study since the late 1960's, where initial studies were conducted on the mono-silicide MnSi [3] and mono-germanide FeGe [4, 5]. The focus of this early work was to investigate the magnetic properties, to identify the type of magnetic ordering present and magnetic ordering temperatures of these newly synthesised cubic B20 materials. The interest in these materials developed from earlier work in B20 FeSi [6] which showed unusual magnetic susceptibility dependant upon a narrow band gap in the electronic structure.

After initial investigations, greater interest developed when the unusual magnetic properties seen in both MnSi and FeGe were identified as a helical spin density wave or helical magnetic state [7, 8] that was long range when compared to the crystal lattice spacing. For FeGe, Lundgren *et al.* [7] proposed a helical spin arrangement to describe the magnetisation and were able to verified the model using magnetic anisotropy measurements. Whereas, for MnSi, Ishikawa *et al.* [8] used small-angle neutron scattering (SANS) to directly measure the helix wavelength, λ_h, by observation of magnetic Bragg satellites corresponding to the periodicity of the magnetic structure within the crystal.

The origin of this helical magnetic structure was explained by using the Dzyaloshinskii-

Moriya interaction (DMI) [9, 10] to account for the canting of the magnetic moments and the formation of a helical magnetic ground state [11, 12]. Nakanishi *et al.* [11] were able to show that by minimizing the free energy the lowest energy state was a magnetic helix in MnSi and similarly Bak and Jensen [12] were able to use this more generally to describe the appearance of a magnetic helical phase in both MnSi and FeGe.

After this discovery, exploration into more features of the helical state continued with how the helix behaved under applied field [13, 14] and reorientation within the crystal [15]. From here the next step that was taken was to look at how the composition of the materials affected these magnetic properties and this continued with investigations of intermediate B20 compounds such as $Fe_{1-x}Co_xSi$ and $Co_{1-x}Mn_xSi$ [16] which showed the long range helical magnetic ordering persisted into the intermediate compositions and the helix wavelength was composition dependent. For the germanides interest continued with exploration into neighbouring materials of FeGe, such as MnGe or CoGe [17] where the Fe site was substituted with another 3d TM. Here the effective moment was found to vary with composition and a shift between the expected moment of the corresponding metal in a fcc structure. This shift was identified as a transfer of 0.7 electrons from germanium to the 3d metal in the B20 monogermanides.

The helix wavelength in FeGe was directly measured using SANS by Lebech *et al.* [18] and a detailed review of the magnetic properties of FeGe was given. They were also able to identify a change in the preferred helix axis direction at two characteristic temperatures, at high temperature T_2 the helix was found along the <100> and below at T_1 along the <111> direction where the helix reorientation was explained by a change in the anisotropy not considered before [19]. Following this, except for some general studies on the magnetic properties of MnSi and FeGe [20], interest in these materials had started to decline.

It wasn't until the seminal paper in 2009 by Mühlbauer *et al.* [21] where the experimental discovery of skyrmions in a magnetic system had been made, that the revival of interest in the B20 system happened. Magnetic skyrmions are a topologically stable spin textures that have particle-like properties [22]. The skyrmion concept was originally proposed by Skyrme in the field of nuclear physics to describe the existence of nucleons from a field [23], however, since then they have been proposed to exist in condensed matter systems [1]. Theoretical predictions of topologically stable states had been made earlier [24, 25] and in 2006, Rößler *et al.* [22] predicted the existence of skyrmions

in a magnetic metal with chiral interactions, but it was the experimental discovery of skyrmions in these magnetic systems that catalysed the recent interest.

After the discovery of skyrmions there was a huge resurgence in research in the B20 system and the helix wavelength and chirality of the magnetic helix with respect to the crystal chirality. SANS has been used extensively to directly measure λ_h [26–29].

Other aspects such as the composition were examined. A major study into $Mn_{1-x}Fe_xGe$ shows the helical wavelength diverged at a critical composition $x_c = 0.8$ [30]. The origin of this change has been identified theoretically where the cause is due to a change in the sign of the DMI. As the DMI strength crosses zero the magnetic state transitions from a helimagnetic order to a collinear ferromagnetic which effectively has a helix wavelength of infinity and thus causes the divergence. This changing DMI has been demonstrated using a simple model [31] and is due to the electronic structure. The changing of x in $Mn_{1-x}Fe_xGe$, which is altering the chemical composition, can be viewed as scanning the Fermi level as x is varied. Band structure analysis has been done in FeGe [32, 33] and identified the origin of the magnetic properties for varying the unit cell, but calculations in $Fe_{1-x}Co_xGe$ are still missing.

After the first reports of directly imaging of a topological structure were reported by Lorentz transmission electron microscopy (LTEM) [34, 34], several reports of direct imaging of skyrmions started to appear including LTEM [35], magnetic force microscopy [36] and small-angle X-ray scattering [37].

1.3   Research in thin films

After the discovery of skyrmions in chiral bulk crystals, the next step was to look at their thin film counterparts to explore if the same magnetic phases were present. The majority of the research has been conducted in MnSi [38–40] which is considered a prototypical B20 system. However, as interest in materials with possible skyrmion phases continued to grow, FeGe became an attractive system due to its near room temperature T_c and has been studied by several groups [41–43]. One of the advantages of using thin films are the compatibility with planar processing techniques, such as photolithography, allowing devices to be produced easily. There are also possibilities of producing multilayer chiral structures where two or more layers with varying composition can be deposited upon on another. Also by depositing a film on top of another interfacial effects can be explored. We have shown how the FeGe affects the magnetisation of a Fe layer through FM coupling

[44]. Also by growing on a substrate with a lattice mismatch, strain can be used to tune properties, such as the ordering temperature of FeGe was found to increase to room temperature when grown on MgO substrates [45].

1.4 Summary

In this thesis we aim to explore the magnetic and electrical transport properties of B20 $Fe_{1-x}Co_xGe$ films when transitioning from bulk crystal to epitaxial films by measuring these properties in the films. We look to study how the magnetic and electrical transport properties are affected by the introduction of defects and impurities due to this change (from single crystal to single phase film with chiral domains) and to examine if the magnetic phases are preserved. By varying the Co content x, we will alter the electronic structure of the material and this will allow us to observe how the associated properties change with composition. By studying this possible skyrmion hosting material we hope to provide further insight into the B20 TM germanides and continue on from previous compositional analysis work [29, 30]. Also as films of this material have not been explored, we hope to fill a gap in the knowledge of this material and offer the possibility of its use for further study in exotic spin structures.

From previous investigations into FeGe and similar systems we can see the kind of magnetic behaviour to expect in $Fe_{1-x}Co_xGe$. In Chapter 2 the theoretical background for the magnetic phases present in the B20 is given.

The experimental methods required to conduct this investigation are given in Chapter 3 where a summary of the methods used are given.

To accomplish this investigation into $Fe_{1-x}Co_xGe$ we first require good quality films that are representative of their B20 structure. Chapter 4 presents the sample characterisation and the samples used for further study.

From the history of the B20 materials and the current interest we can see that the helical magnetic structure is a sign of the DMI being present. In Chapter 5 we look at the magnetic properties of $Fe_{1-x}Co_xGe$ and observe the helical magnetic structure using PNR.

Finally the magnetotransport is explored in Chapter 6. Here we present the resistivity, magnetoresistance and Hall effect measurements along with the possible THE which would arise from any topological structure present.

CHAPTER 2

Magnetic phases in B20 materials

2.1 Introduction

The $Fe_{1-x}Co_xGe$ films that will be studied in this thesis belong to the B20 crystal structure, which includes other TM mono-silicides and germanides such as MnSi and MnGe. The B20 crystal structure is an example of a non-centrosymmetric (lacks inversion symmetry) lattice, which is chiral (see figure Fig. 2.1). Within this group there are magnetic varieties that are host to itinerant ferromagnetism and the combination of the magnetic and non-centrosymmetric structure properties leads to a variety of magnetic states, such as a helical magnetic ground state, and more exotic spin textures such as skyrmions that have recently been of great interest. The underlying theory that describes the origin of the magnetism and the various magnetic phases in this system will be described in this chapter while a detailed description of the crystal structure is presented later in Sect. 4.2.
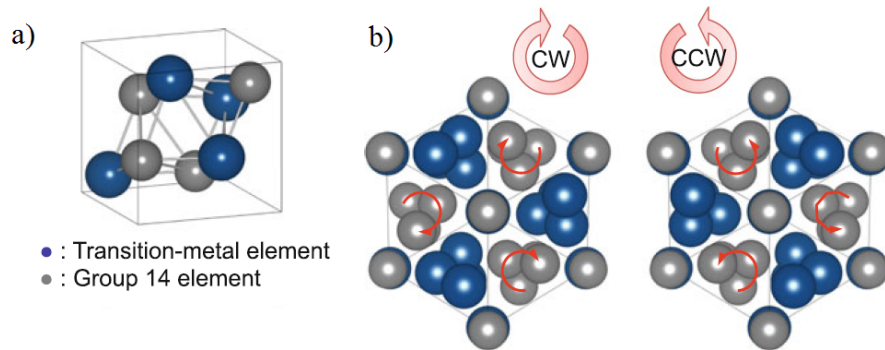
Figure 2.1: B20 crystal structure. a) B20 unit cell. b) Both clockwise (left-handed) and counter clockwise (right-handed) chiralities viewed along the [111] crystal axis. (Figure adapted from Ref. [46]).

2.2 B20 magnetic phase diagram

The chirality of the B20 crystal structure is the origin of the complex and interesting magnetic phase diagram seen in these materials. The magnetic B20 materials are generally considered to be chiral helimagnets with weak cubic anisotropy that order magnetically at cryogenic temperatures ($\sim$ 40 K for MnSi) up to just below room temperature ($\sim$ 280 K for FeGe). Experimentally the magnetic phase diagram for several B20 materials have been discovered for bulk crystals [47–49] and thin films [50] and a
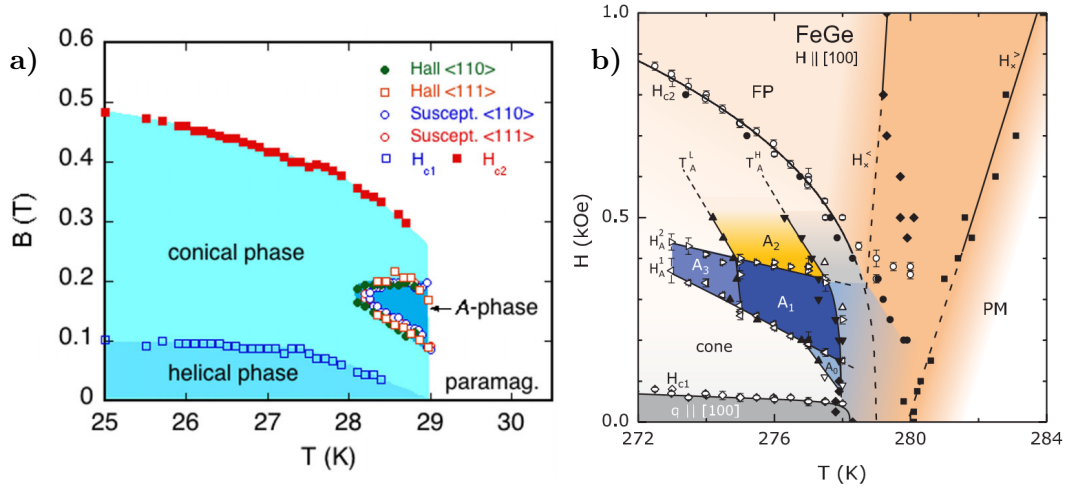
Figure 2.2: Magnetic phase diagrams as a function of temperature and applied field for bulk crystals of, a) MnSi and b) FeGe (Fig. adapted from Ref. [47, 48]).

general magnetic phase diagram has been identified for these materials. The typical one used for example is that for MnSi in Ref. [47] which is often considered the prototypical system, it is shown here in Fig. 2.2. The features shown are the helical, conical, field polarised (FP), paramagnetic and skyrmion lattice (SkL) phases (SkL originally called the A-phase due to unknown anomalous behaviour). These phases are common to the magnetic B20 materials and the magnetic phase diagram for FeGe is also shown in Fig. 2.2 for comparison. In these materials the helical structure is found as the ground state below magnetic ordering T_c and the critical field H_c. On increasing field strength the helical structure starts to deform and becomes conical, if the field is increased further to H_{c2} the magnetisation is saturated and it becomes FP. With increasing temperature, H_{c2} decreases and a crossover from FP to paramagnetic is seen at the magnetic ordering temperature T_c. The small window seen just below T_c is the SkL phase and describes an area where, for bulk samples, the skyrmion lattice is thermodynamically stable. The magnetic phases shown in these diagrams have been explained and will be described in the following sections.

2.3 Heisenberg exchange interaction

The Heisenberg or symmetric exchange interaction describes the interaction between two electrons with relation to their spin orientation and is usually the origin of magnetic ordering. The interaction is given by the Hamiltonian,

$$H_{\text{ex}} = -J \left(\mathbf{S}_1 \cdot \mathbf{S}_2 \right), \tag{2.1}$$

where J is the Heisenberg or symmetric exchange interaction between two neighbouring spins $\mathbf{S}$. The sign of J determines how the interaction energy is minimised and determines the spin alignment between nearest neighbours with $J > 0$ for a parallel, ferromagnetic (FM) and $J < 0$ for an anti-parallel, antiferromagnetic (AFM) alignment.

2.4 Dzyaloshinskii-Moriya interaction

The Dzyaloshinskii-Moriya interaction (DMI) was first introduced as a phenomenological explanation for weak ferromagnetism in α-Fe_2O_3 [10]. It was found that the due to symmetry within the structure, the energy of the magnetisation was minimised with the spins canted or perpendicular to one another leading to the expression,

$$H_{\text{DM}} = -\mathbf{D} \cdot \left(\mathbf{S}_1 \times \mathbf{S}_2 \right), \tag{2.2}$$

where $\mathbf{D}$ is the DMI vector. This was then later developed by Moriya by taking the spin orbit coupling into account and the rules for determining the direction of $\mathbf{D}$ are given by Moriya in Ref. [9].

2.5 B20 magnetic structure

The first description of the magnetic structure for B20 materials was developed by Bak and Jenson [12] for bulk MnSi and FeGe. Here they found they were able to describe the helical magnetic structure, by including the DMI, as the result of competing magnetic interactions. A simplified overview of the energy terms is given by,

$$H_{\text{bulk}} = H_{\text{ex}} + H_{\text{DM}} + H_{\text{ani}} + H_{\text{app}} \tag{2.3}$$

where H_{ex} is the Heisenberg or exchange energy, H_{DM} is the DMI energy, H_{ani} is the magnetocrystalline anisotropy and H_{app} is the Zeeman energy from an external applied

field. For the chiral magnets the competition between the exchange interaction H_{ex} and the DMI H_{DM} results in the helical magnetic structure, whereas the relatively weak magnetocrystalline anisotropy H_{ani} determines the helix direction and an applied field H_{app} acts distorts the helix structure.

This model and resulting energy hierarchy was extended to cover general noncentrosymmetric cubic helimagnets by adding additional terms such as uniaxial anisotropy allowing the model to describe thin films as well as bulk [51, 52]. In thin films it has been shown that the energy hierarchy of terms is modified due to additional uniaxial anisotropy that is generated through strain induced from the lattice mismatch between the film and substrate [40, 41, 53] and also from the change in geometry from a bulk crystal to a film. In Ref. [52] the energy hierarchy to describe these systems is given in terms of the energy density $w(M)$ for a helimagnetic film in a magnetic field applied out-of-plane ($H \parallel z$),

$$w(M) = A \left(\nabla M \right)^2 - DM \left(\nabla \times M \right) - K M_z^2 - H M_z \tag{2.4}$$

where Eq. 2.4 is the Bak and Jensen formalism [12] with an additional uniaxial term. The first term in Eq. 2.4 is the exchange interaction with exchange stiffness constant A, the second term is the DMI with constant D, the third term is the uniaxial anisotropy with constant K, here the value of $K > 0$ for films with easy-axis anisotropy and $K < 0$ for films with a hard-axis anisotropy. The final term is the Zeeman energy from the applied field. They then show that by using a magnetization vector $\mathbf{M}$ in spherical coordinates of the form,

$$\mathbf{M} = M \left(\sin \theta \cos \phi, \ \sin \theta \sin \phi, \ \cos \theta \right), \tag{2.5}$$

where M is the magnetization modulus, the magnetic phases found experimentally can be described and are shown in Fig. 2.3.

A magnetic phase diagram has been calculated for the B20 system by Rybakov *et al.* [54] using a classical spin model with the same form as Eq. 2.4 without the anisotropy. They identified the ranges of the different phases by calculating the ground state and the results are shown in Fig. 2.4 as function of reduced film thickness, L/L_{D} and reduced field, $H/H_{\mathbf{D}}$. The results show the same phases as the experimentally measured ones, shown in Fig. 2.2, with the addition of an isolated skyrmion phase shown by the dashed area.
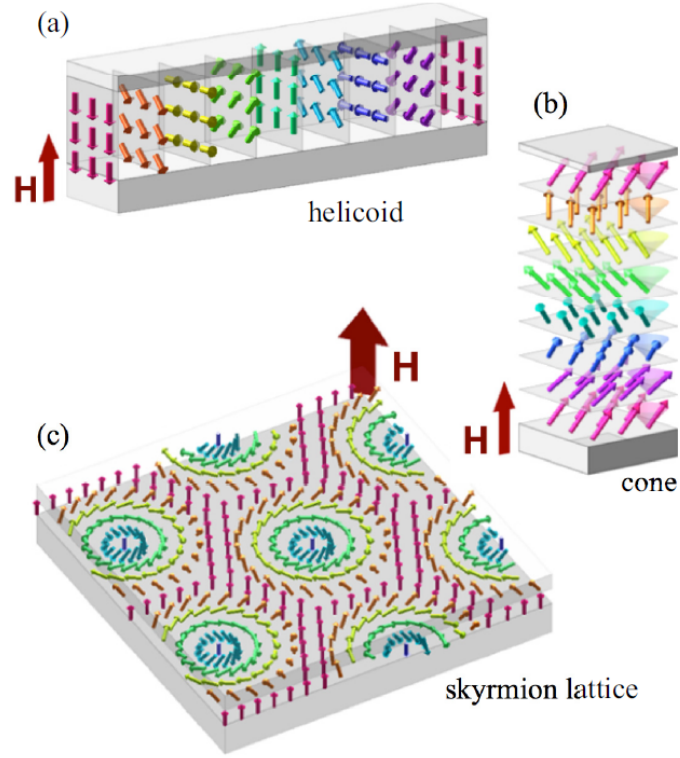
Figure 2.3: Magnetic phases in B20 films using Eq. 2.4. a) helical/helicoid phase, b) conical phase and c) skyrmion lattice (SkL) phase (Fig. adapted from Ref. [52]).
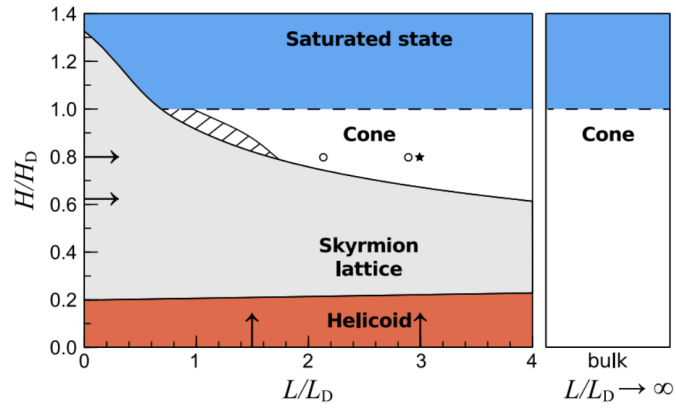
Figure 2.4: Calculated magnetic phase diagram for ground state of isotropic B20 helimagnetic film using Eq. 2.4. (Figure adapted from Ref. [54]).

11

2.5.1 Helical magnetic structure

A universal and defining feature of the magnetic B20 materials is the appearance of a spiral spin ordering or helical magnetic structure ground state. The helical structure arises due to the appearance of DMI in the system alongside the Heisenberg exchange that is present in all magnetically ordered systems.

The helical structure can be visualised, shown in Fig. 2.3 a), as a series of planes of ferromagnetically ordered moments that rotate with an angle between planes along an axis perpendicular to the plane. This is defined as the helix axis or propagation vector Q. A full rotation of the spin about this axis defines the helix wavelength and leads to the relation, $Q = 2\pi/\lambda_\mathrm{h}$ where λ_h is the helix wavelength. In turn this rotation is dependent on the relative strength between the H_ex and H_DM energies with $\lambda_\mathrm{h} \propto J/D$. It can be seen that as the DMI is reduced, $D \to 0$, λ_h tends towards infinity which results in a parallel collinear alignment and essentially returns to a normal FM phase.

2.5.2 Helicoid structure

The helicoid structure is a helix of planes about an axis and the term has been adopted to describe the magnetic structure in a helimagnet as the helix structure extends through the planes of the film [40, 44, 52]. The helicoid structure in this case refers to a helimagnet subject to an applied field perpendicular to the helical axis Q where the field acts to distort the helix, effectively unwinding it and changing the modulation period. When an external field is applied, if the anisotropy K is strong enough, the helix will be deformed in this manner rather than the helix axis changing direction [55]. A diagram of this process is shown in Fig. 2.5, with increasing field strength from panels a) to c). In a) a small applied field is too weak and the helix form remains, in b) the field is increased and the helicoid is transformed by unwinding part of the structure. As the field is increased the structure continues to deform and becomes FP as shown in c). This phenomenon was found in films of MnSi [40, 55] and we also found this to be the case in thin films of FeGe [44] where the helix wavevector Q was found to be fixed in direction, normal to the plane of the film (parallel to FeGe [111]).
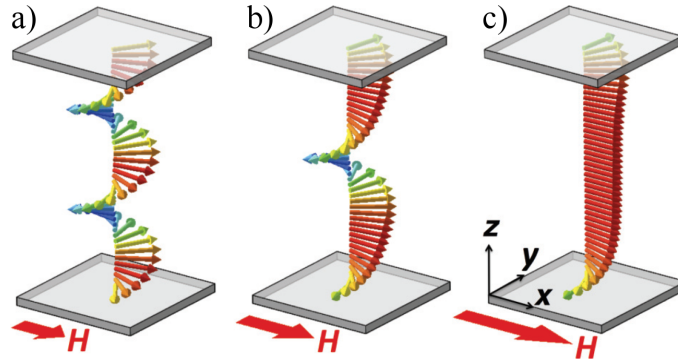
Figure 2.5: Magnetic helicoid phases for a helimagnetic thin film. When uniaxial aniso-
tropy is strong enough to fix the helix axis, the applied external field acts to distort the
magnetic helix by unwinding its structure. Panels a-c) show increasing external mag-
netic field; a) ground state magnetic helix b) magnetic helicoid under applied field and
c) field polarised. (Figure adapted from Ref. [55]).

2.5.3 Conical structure

Under application of a magnetic field parallel to Q the moments tilt towards the direction
of the field and a conical phase is formed, as shown in Fig. 2.6. On increasing the field
strength the moments continue to align with the field direction until the magnetisation
saturates and becomes uniformly magnetised.
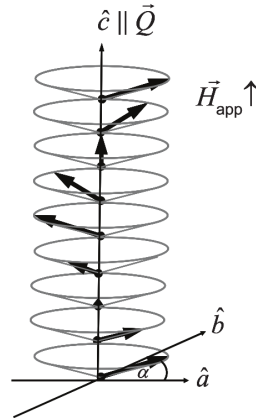
Figure 2.6: Magnetic conical structure for a helimagnetic thin film. (Figure adapted
from Ref. [56]).

2.5.4 Skyrmions

The main driving force behind the recent revival of interest in the B20 system is the discovery of magnetic skyrmions. These topological spin structures are particle-like magnetic objects, a diagram of is shown in Fig. 2.7 a). The skyrmion structure is characterised by

$$N_{sk} = \frac{1}{4\pi} \int m \cdot \left(\frac{\partial m}{\partial x} + \frac{\partial m}{\partial y} \right) dxdy, \tag{2.6}$$

where N_{sk} is the skyrmion winding number and m is a unit vector in the direction of the local magnetic moment. The presence of skyrmions leads to non-zero integer values of N_{sk} (usually ± 1) which corresponds to the magnetic moments wrapping the surface of a unit sphere [1], the value of N_{sk} is the number of times the skyrmion wraps the unit sphere, shown in Fig. 2.7 b). This structure in turn corresponds to a change in topology (from a plane to a sphere) which results in an energy barrier that provides the topological stability.
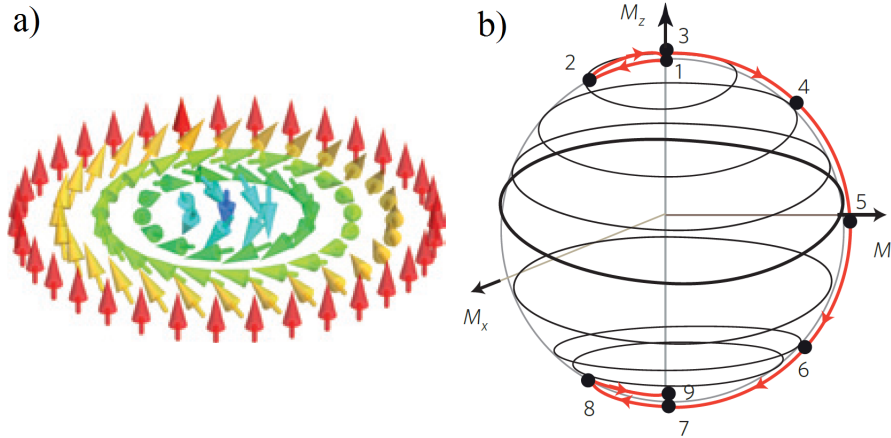
Figure 2.7: a) Diagram of a magnetic skyrmion spin texture. b) A unit sphere, the spin structure of a skyrmion wraps the entire surface. (Figure adapted from Ref. [1, 2]).

2.6 Summary

In this chapter we have introduced the background theory for the magnetic states in chiral helimagnets in both bulk crystal and thin films. The B20 systems offers a range of magnetic phases to explore due its complex interplay between magnetic interactions.

Experimental measurements have been able to identify several different magnetic phases present in these systems and the phase diagrams have been mapped for many of the materials.

The helimagnetic theory is now able to describe these phases for both bulk and film samples. In films it can be seen that the additional uniaxial anisotropy induced from film growth can play a major role in altering the energy scales resulting in different phases being accessible [52]. The previous work in Ref. [52] by Wilson *et al.* provides a detailed study which shows the skyrmion phase with an applied field along the (111) direction is accessible for films of FeGe on Si due to this uniaxial anisotropy. Their calculations predict a strong $K > 0$ aniostropy which has been observed experimentally [41, 44] and skyrmions reported by Huang *et al.* have fallen under the predicted conditions for FeGe. These results show a good starting point for the investigation into $Fe_{1-x}Co_xGe$ as the anisotropy is expected behave similarly.

By understanding how the magnetic structure is affected when transitioning from bulk to film we have a good starting point to observe how the magnetic structure is altered with composition in $Fe_{1-x}Co_xGe$ by comparison to its parent material FeGe and similarities to other compositional analysis studies in the B20 material group.

CHAPTER 3

Sample Preparation and Measurement Methods

3.1   Introduction

In this chapter the experimental methods of sample preparation and measurement are described.

The first challenge that was to be overcome was to find a suitable method to produce thin films of $Fe_{1-x}Co_xGe$ with high phase purity. Films of FeGe have been previously grown via magnetron sputtering [41, 42] that were textured and contained some impurity phases (non B20 crystal structure). At the start of the project film growth using molecular beam epitaxy (MBE) had been started as this method had already showed it was able to produce high quality films of similar B20 material, MnSi [40] and $Fe_{1-x}Co_xSi$ [53]. However the FeGe films initially produced still contained some impurity phases and had large degree of roughness. The method has been refined to improve the quality of the films produced by reducing the presence of impurity phases and improving interface quality, and also to allow the addition of Co; the details of this method are described in this chapter.

After films were grown, they were characterised to determine if the material was the correct crystal phase and the majority of the film measurements were performed at Leeds. The structural, magnetic and electron transport properties were investigated using a range of X-ray, magnetometry and magnetotransport techniques which are described in this chapter.

Further investigation into the helical magnetic structure were performed using polarised neutron reflectometry.

3.2   Sample Preparation

To study the properties of $Fe_{1-x}Co_xGe$, high quality samples are required and for this reason films have been grown using MBE. This methods utilizes very precise deposition rate control which allows epitaxial films of a chosen crystal phase to be achieved with smooth interfaces and good thickness control. Thin films also allow the material to be patterned using planar processing techniques into devices that can be used for magnetotransport studies.

3.2.1 Molecular beam epitaxy (MBE)

Molecular beam epitaxy (MBE) is an ultra-high vacuum (UHV) thin film deposition technique that can control film thickness at the atomic level by use of low flux (< 1 Å/s) thermal atomic or molecular beams. A substrate is placed in a UHV chamber ($< 10^{-9}$ mbar pressure) where source materials are heated until evaporation and a film of material is deposited upon the substrate. The UHV ensures minimal contamination and choice of substrate and deposition rate allow layer structure and thickness control. The MBE system at Leeds is equipped with *in situ* analysis tools to monitor the film growth and will be discussed in greater detail in Sect. 3.3.

3.2.2 B20 FeGe

B20 FeGe thin films were grown by MBE. A substrate of Si (111) (room-temperature resistivity of 3-5 kΩ cm) was annealed at 1200°C for 2 minutes to remove the native oxide and allow for a (7×7) surface reconstruction to ensure a clean and well ordered surface. This was verified *in situ* and will be discussed in more detail later. The substrate was allowed to cool to approximately room temperature before deposition (< 50°C). The FeGe film was grown by co-deposition from Fe and Ge e-gun sources and a quartz crystal monitor on each e-gun was used to measure and regulate the flux from each source. To start the growth approximately 1 nm of material (thickness of film before crystallization) was then deposited. The sample was then heated to 230°C to allow the layer to crystallise, forming a seed layer for growth. A further four nanometers were then deposited with intervals of 15 minutes in-between each nanometer to allow for crystallisation which was verified by RHEED. The films were then co-evaporated with a net rate between 0.3-0.6 Å/s using RHEED to monitor the structure during growth. After deposition a second LEED image was taken to verify epitaxial growth. Finally after cooling to room temperature a cap layer of Ge (~ 4 nm) was deposited on some of the samples to help prevent oxidation.
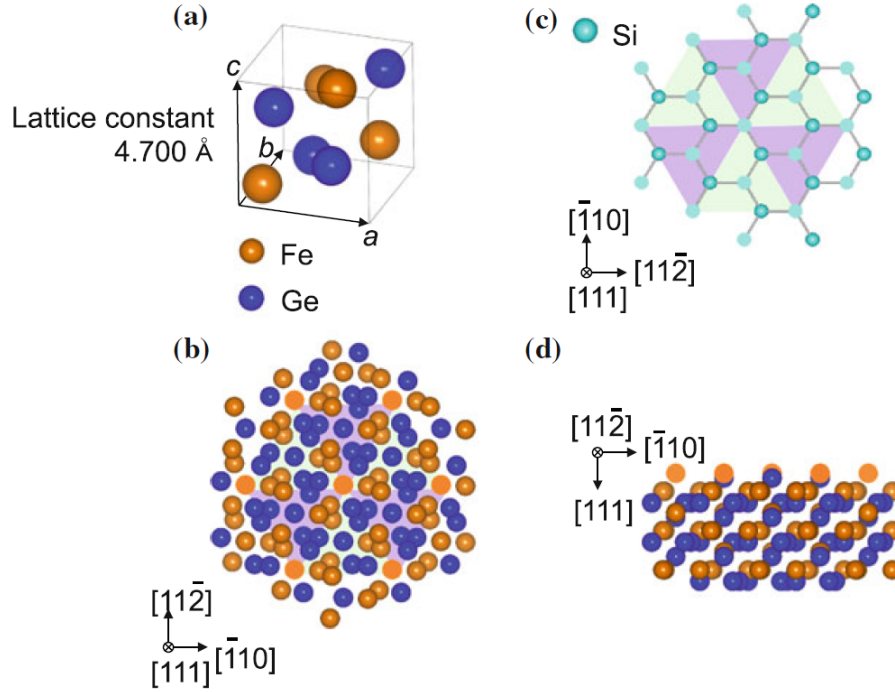
Figure 3.1: Diagram of crystal structure in B20 FeGe on Si films. a) FeGe unit cell. Crystal structure viewed along the [111] direction for b) FeGe, c) Si and viewed along the [11$\bar{2}$] direction for d) FeGe (Figure taken from Ref. [46])

3.2.3   B20 $Fe_{1-x}Co_xGe$

In the case of $Fe_{1-x}Co_xGe$ the above method was used with the addition of a Co e-gun source. The flux from the third source was measured by an additional quartz crystal monitor. To vary x the rate of Fe to Co deposition was varied with the overall transition metal (TM) to Ge ratio being kept constant at 1:1.

3.3   In situ characterisation

During sample fabrication it was necessary to monitor the film growth to ensure the correct material phase was being made. The MBE system used was equipped with two *in situ* methods; low-energy electron diffraction for surface structure analysis and reflection high-energy electron diffraction for real-time growth phase monitoring.

3.3.1   Low-energy electron diffraction (LEED)

Low-energy electron diffraction is a surface sensitive technique that allows the surface net crystal structure and orientation to be determined. A beam of low-energy (20-200 eV) electrons is applied normal to the surface plane of a sample and the diffracted electrons form a pattern which is visible on a fluorescent screen. Due to the low-energy of the electrons the penetration depth is limited a few atomic layers and so only the surface is probed.

After surface reconstruction, but before film growth, the substrate to be used was first measured by LEED, shown in Fig. 3.2. This allowed verification of the (7×7) reconstruction to ensure the substrate was suitable for growth shown in Fig. 3.2 a). After the film was deposited, LEED was then used again to measure the film surface to verify the growth, the result from a FeGe film is shown in Fig. 3.2 b). An overlay of the pattern in b) on a) is shown in c). Here the expected 30° in-plane rotation epitaxy can be seen [38, 42].
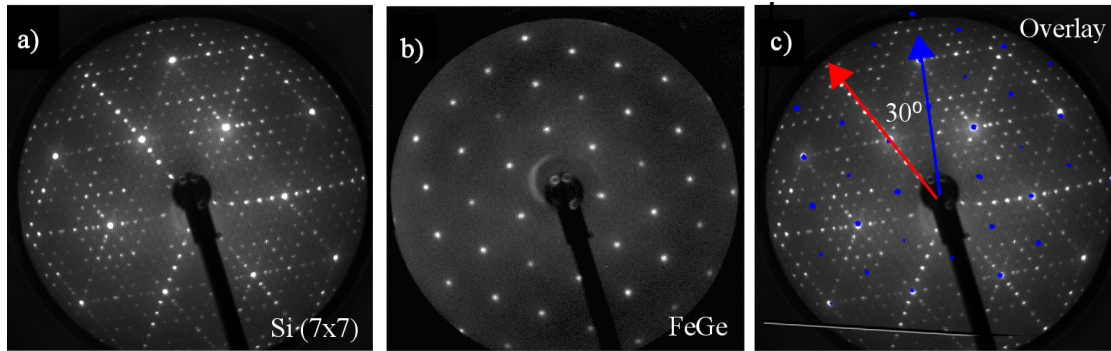
Figure 3.2: Low-energy electron diffraction patterns for a) Si (7×7) reconstruction. b) B20 FeGe film after deposition. c) Overlay of FeGe pattern on Si substrate pattern. As a) and b) were both measured in the same orientation, c) shows a direct overlay and the 30° in-plane rotation epitaxy. (FeGe pattern shown in c) was rotated 2° to correct for misalignment between measurements in a) and b))

3.3.2   Reflection high-energy electron diffraction (RHEED)

Reflection high-energy electron diffraction (RHEED) is another surface sensitive technique that allows the crystal structure of a material to be characterized, however in
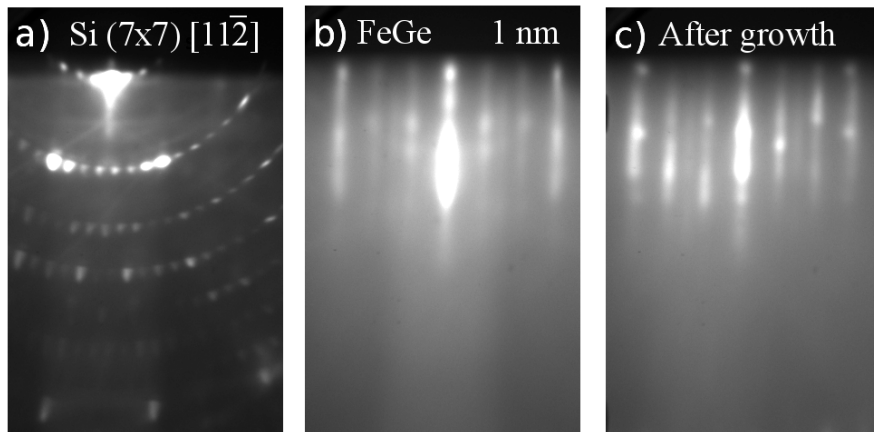
Figure 3.3: High-energy electron diffraction patterns for a) Si substrate (7×7) pattern, b) 1 nm of B20 FeGe, c) after full film deposition.

contrast to LEED it can be used during film deposition and allows the films crystal phase to be monitored in real-time. The technique, similarly to LEED, uses a beam of electrons, however this time they are high-energy (10-30 keV) and are incident at just above grazing incidence. The diffracted electrons are again shown on a fluorescent screen and the patterns formed show if a crystal structure is present.

Before film growth, but after annealing the surface of the Si substrate was measured using RHEED. Figure 3.3 a) shows the (7×7) reconstruction. Once film deposition has started, RHEED was continuously used to monitor the growth. The resulting pattern after 1 nm of deposition is shown in Fig. 3.3 b) and after growth is shown in Fig. 3.3 c).

3.4   X-ray techniques

Once a sample was deposited the structural properties were characterized using x-ray techniques. X-ray diffraction (XRD) was used to look at the crystal phases present in the film and X-ray reflectometry (XRR) was used to measure the film's thickness and layer structure.

3.4.1   X-ray diffraction (XRD)

X-ray diffraction has been an invaluable tool for identifying and characterising crystalline materials. The lattice spacing in crystals can be found using the Bragg equation which is given by

$$n\lambda = 2d\sin\theta, \tag{3.1}$$

where n is the diffraction order, λ is the wavelength of the incident X-ray, θ is the incident angle and d is the inter-planar spacing of the lattice.

XRD measurements were preformed to identify the crystal phases present in the films. The measurements were taken in a Bruker X-ray diffractometer in a $\theta - 2\theta$ (Bragg-Brentano) geometry. Here the detector is aligned to the reflection from the plane of interest within the crystal and the detector angle, 2θ, is swept over the desired range. In the case of films with a known crystal orientation with respect to the substrate, the measurement can be aligned to a known crystal plane in the substrate. Since the substrate usually produces a strong diffraction signal ($t_{\mathrm{sub}} \gg t_{\mathrm{film}}$). For epitaxial B20 $\mathrm{Fe}_{1-x}\mathrm{Co}_x\mathrm{Ge}$ on Si, the film grows along the Si [111] direction and by aligning to the Si (111) peak this allows the B20 $\mathrm{Fe}_{1-x}\mathrm{Co}_x\mathrm{Ge}$ to be easily found.

The results for a sample of FeGe are shown in Fig. 3.4. Two data sets are shown, The red line is the standard measurement with no additional optics and the black line was taken using a Ge monochromator which allows for additional resolution at the cost of beam intensity (~ 1 order of magnitude). For this sample both measurements show the film to be single phase with Bragg peaks for the FeGe film appearing at $\theta = 33.05°$ and $\theta = 69.40°$ corresponding to the (111) and (222) reflections respectively.

3.4.2   X-ray reflectometry (XRR)

To measure the film thicknesses and look at the layer structure, X-ray reflectometry (XRR) measurements were made using the same setup as for XRD (see Sect. 3.4.1).
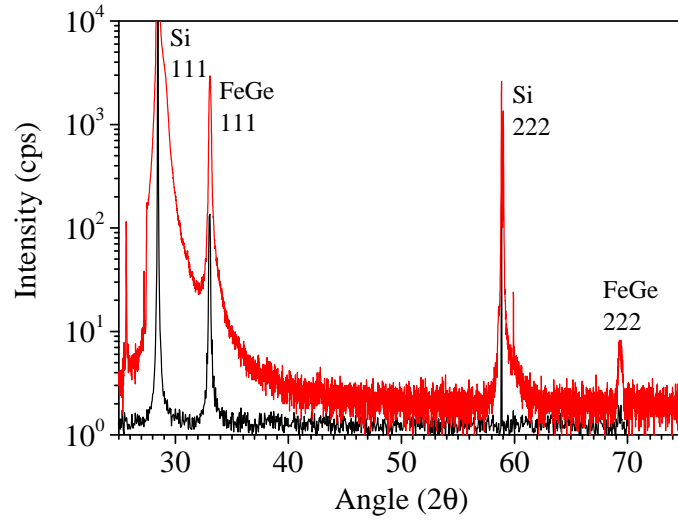
Figure 3.4: X-ray diffraction measurement for an FeGe sample. The black line shows the measurement with a Ge monochoromator and the red line shows it without.

Similarly to XRD, the sample is set in the same $\theta - 2\theta$ geometry (specular reflection), however the angle of reflection is set to a small angle (0-6° 2θ for these measurements) and the resulting interference from the film layer interfaces are measured.

A phenomenon that is important to this technique is that of total external reflection, below a certain angle θ_c, X-rays are unable to penetrate a material and this angle depends on the electron density in the material. To explain this we look at the refractive index n for a material. A detailed description can be found in Ref. [57], where n is given by

$$n = 1 - \delta, \tag{3.2}$$

with

$$\delta = \frac{2\pi\rho_e r_0}{k^2}, \tag{3.3}$$

where ρ_e is density of electrons, r_0 is the scattering amplitude per electron and k is the associated wave vector related through $k = 2\pi/\lambda$ where λ is the wavelength of the incident radiation. Through the use of Snell's law

$$\cos\theta = n\cos\theta', \tag{3.4}$$

the critical angle θ_c can be found by setting $\theta' = 0°$, which results in the following

$$\theta_c = \sqrt{2\delta} = \frac{\sqrt{4\pi\rho_e r_0}}{k}, \tag{3.5}$$
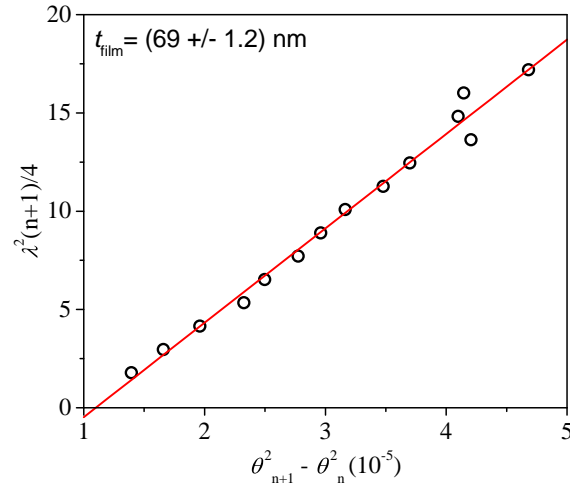
Figure 3.5: Thickness of FeGe film determined using Eq. 3.6 by plotting spacing of Kiessig fringes.

showing the critical angle θ_c is proportional to the electron density ρ_e.

From a low angle XRR measurement, the main features that can be seen are θ_c and the oscillations in the reflected intensity which are known as Kiessig fringes, these fringes arise from interference between the reflections at each interface. The thickness of a film can be determined using the spacing of the Kiessig fringes with the following equation:

$$n\lambda = 2t_{\text{film}}(\sin^2\theta_n - \sin^2\theta_c)^{1/2}, \tag{3.6}$$

where n (not to be confused with the refractive index) is the diffraction order, t_{film} is the film thickness, θ_n is the angular position of the nth interference (Kiessig) fringe and θ_c is the critical angle. This method offers a quick determination of a film thickness and is useful for calibration films and single layer films. By plotting the spacing between fringes t_{film} can be found, an example for a FeGe layer is shown in Fig. 3.5.

For more detailed information and multilayer structures, a more complex method is required. The fits for XRR (and later polarised neutron reflectometry) were performed using the GenX [58] software package. This method utilizes the Parratt recursive method [59] to describe the film as a series of layers atop a substrate. Each layer has an associated scattering length density (SLD) that is dependant on the electron density in that layer. This depends on the elements present and the crystal structure in the layer. The method can be extrapolated to any number of layers and allows a film's layer structure to be determined.

24
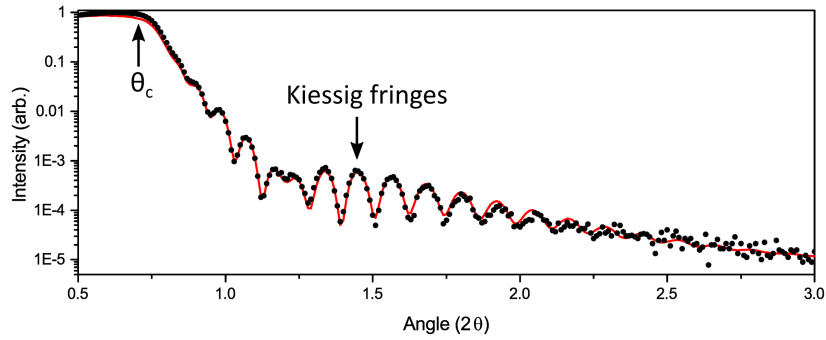
Figure 3.6: X-ray reflectivity measurement for a $Fe_{0.6}Co_{0.4}Ge$ film (circles) and fit (line). Arrows show the critical edge θ_c and presence of Kiessig fringes.
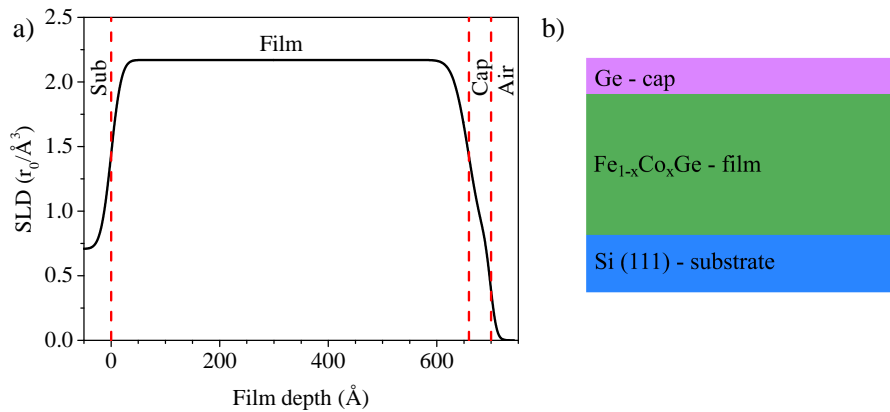
Figure 3.7: Layer structure determined from XRR fitting, a) scattering length density as a function of film thickness and b) resulting layer structure, a single homogeneous layer of $Fe_{1-x}Co_xGe$ with Ge cap.

The reflectivity measurement and fit for a $Fe_{0.6}Co_{0.4}Ge$ epilayer is shown in Fig. 3.6 and the SLD and layer structure for the best fit is shown in Fig. 3.7. The resulting thickness for the $Fe_{1-x}Co_xGe$ layer is (65.8 ± 0.1) nm and for the cap layer (4.08 ± 0.09) nm, showing fairly good agreement with the chosen growth values of 70 nm for the $Fe_{1-x}Co_xGe$ film and 4 nm for the cap. All the films grown had a layer thickness to within 10 % of the chosen values.

3.5   Polarised Neutron Reflectometry (PNR)

Polarised neutron reflectometry is a technique used to examine the magnetic depth profile of a magnetic film or multilayer. The principle of operation is similar to XRR, except that a beam of neutrons are reflected from a film at near grazing incidence and the reflected intensity is measured. Due to the neutron's magnetic moment, magnetic information can also be observed. The reflected intensity of the neutron beam depends on neutron scattering length density

$$\rho_n = \sum_i b_i, \tag{3.7}$$

where ρ_n is the neutron scattering length density and b_i is neutron scattering length for layer i. This is the equivalent in PNR as the electron density ρ_e is for XRR, shown in Sect. 3.4.2. However, unlike ρ_e which scales directly to the electron number Z, this value depends on the neutron scattering length b, which is element specific.

The PNR measurements shown in this thesis were taken at ISIS, STFC Rutherford Appleton Laboratory, UK, using time-of-flight PNR on the PolRef instrument. Nominally 20 mm $\times$ 20 mm samples were mounted in a helium flow cryostat in a $\theta - 2\theta$ configuration. A magnetic field was applied in plane with the film, and the sample was aligned such that this was parallel to the FeGe [110] direction. A diagram of the set-up and the sample orientation is shown in Fig. 3.8. A beam of polarised neutrons was then reflected from the sample and the intensities of the up (I_+) and down (I_-) reflections were measured as a function of scattering vector $q_z = (4\pi/\lambda)\sin\theta$, where θ is the incident angle and λ is the wavelength of the incident neutron. The variation in q_z is provided by the distribution of velocities (and hence wavelengths) within the neutron beam and two values of θ were used to provide a range of 0.01 - 0.15 Å^{-1}. As there is limited information at the higher wavevector transfers and for experimental expediency a compromise was reached between the measurement time and the statistical error of the high q_z data and so the PNR data presented here is shown with a range of q_z up to 0.1 Å^{-1}. Finally, the data were rebinned to a constant resolution of $\Delta q_z/q_z$ of 3% consistent with the selected measurement resolution.

Before looking at the helical structure it was important to verify the chemical structure and to check magnetic properties of the films. First the sample was measured at room temperature (above T_c) and at the maximum available field (667 mT) to determine the structure of the sample without any magnetic component and to compare this with
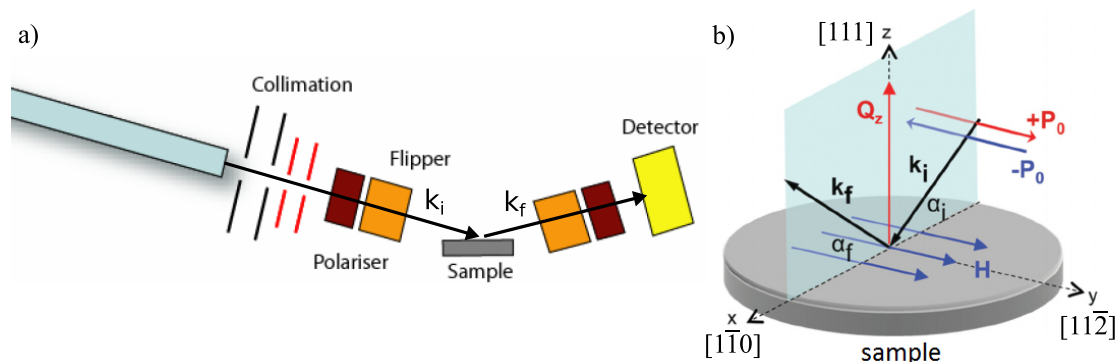
Figure 3.8: a) schematic of the PolRef beamline, b) close-up of sample space showing the neutron plane of incidence with neutron polarisation directions and the magnetic field orientation. Figure adapted from Ref. [60]

the XRR results. The sample was then field cooled to below T_c and another measurement was taken to obtain the saturation moment. Figure 3.9 shows the measured PNR from a $Fe_{0.6}Co_{0.4}Ge$ film with an applied field of 667 mT. Figure 3.9 a) shows the results at 300 K (above T_c) and here it can be seen there is almost no splitting. In Fig. 3.9 b) at 50 K (below T_c) a large splitting between the two polarisations resulting from the sample now being magnetically saturated can be seen. The insets in each figure show the scattering length density (SLD) as a function of the film depth with the substrate (Si) at 0 Å. Both profiles have the same shape, with just the one at 50 K having a slightly larger value for the $Fe_{1-x}Co_xGe$ layer due to the additional magnetic component. Figure 3.9 c) and d) show the spin asymmetry (SA) for 300 K and 50 K respectively. It can be seen in c) that above T_c where there is essentially no magnetic signal, there is no splitting and so the SA shows a flat line. In d), due to the large moment and splitting seen in b) there is an oscillating 'fin' structure seen in the SA which is characteristic of a FM material. From these fits the moment as a function of film depth can be plotted and is shown in the insets in Fig. 3.9 c) and d).

This technique was applied to each composition of $Fe_{1-x}Co_xGe$ to identify the helical magnetic structure at low fields and the results for this method will be given in Chapter 5.
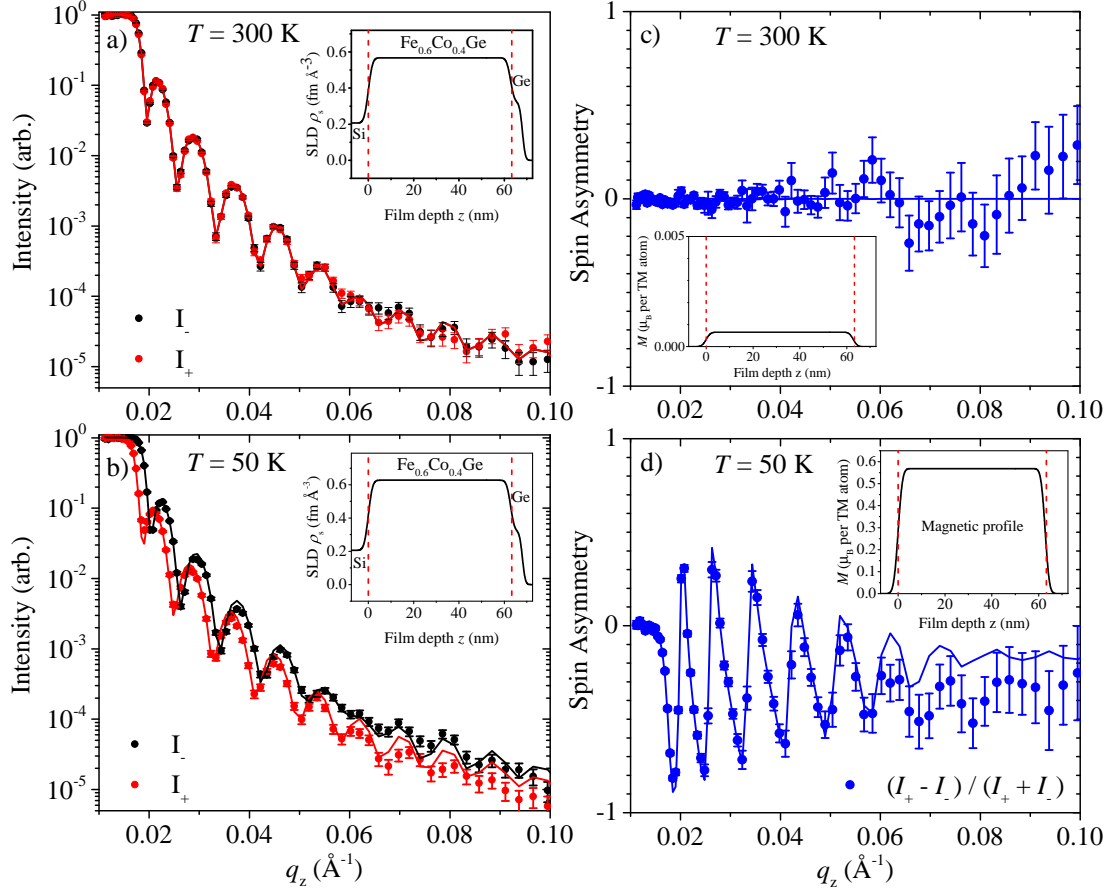
Figure 3.9: PNR reflectivity data (circles) and fits (lines) for up, I_+ (red) and down, I_- (black) neutron polarisation reflections from a $Fe_{0.6}Co_{0.4}Ge$ film measured at a) 300 K and b) 50 K in a 650 mT field and spin asymmetry (SA) (circles) and fits (lines) with magnetic depth profile for each temperature in c) and d). a) At 300 K the sample is above T_c and almost no splitting is seen between the two polarisations. b) At 50 K that sample is below T_c and a large splitting between I_+ and I_- can be seen resulting from the magnetisation in the film. The insets in a) and b) each figure show the scattering length density for the total film as a function of film depth. c) Where there is no splitting seen in a) the SA shows a flat line about zero and only a negligible moment in the magnetisation profile. d) When a large splitting is seen in b) an oscillating SA can be seen which is characteristic of a FM ordered material. Insets in c) and d) show the magnetic depth profile obtained from the fits.

3.6 Magnetometry

Magnetic measurements were taken using a Quantum Design MPMS superconducting quantum interference device vibrating sample magnetometer (SQUID-VSM). This type of magnetometry allows the magnetic moment with respect to the applied field to be measured and makes use of the SQUID's high sensitivity allowing measurements as low as 10^{-8} emu. In the instrument a sample is placed between a set of coils that are inductively coupled to the SQUID and a superconducting magnet is used to provide the applied field to magnetize the sample. The sample is then vibrated between the coils and through Faraday's law of induction the sample is used to induce an EMF and thus a current in the loop. The SQUID then converts this current into a voltage and the time-varying signal due to the sample is separated and amplified using lock-in amplifier techniques.

As the samples are thin films, they were mounted either with the applied field parallel to the plane (in-plane) or normal to the plane (out-of-plane) of the film. Samples were cut from the films into small squares with a surface area varying from approximately 2 mm^2 to 3 mm^2. The surface area was measured by taking an optical image of the cut sample and using an image processing software package (ImageJ [61]) to measure the dimensions digitally. The film volume of the cut sample, used to normalise the magnetisation of each sample, was calculated using this surface area along with the film thickness determined by XRR (see Sect. 3.4.2). The holders that were used depended on the orientation of the sample: for in-plane measurements a flat paddle quartz holder; and for out-of-plane a brass tube holder with quartz blocks to secure the sample. Both holders required a small amount of low-temperature resin to keep the sample fixed in place. For each orientation of measurement a correction for the background signal produced by the holder and the Si substrate was required. To do this a linear fit of the measured values at high field (above the films saturation) was averaged over both directions of applied field and subtracted from the data.

An example of the background subtraction is shown in Fig. 3.10. Here the in-plane magnetization of a FeGe sample is shown, above saturation (> 1 T) a linear decrease is seen due to the diamagnetic contribution of the Si substrate and by subtracting this linear component, the saturation moment can be found. As the SQUID-VSM measures the total moment of the sample the magnetization was found by dividing by the total volume of the film present in the measured sample.
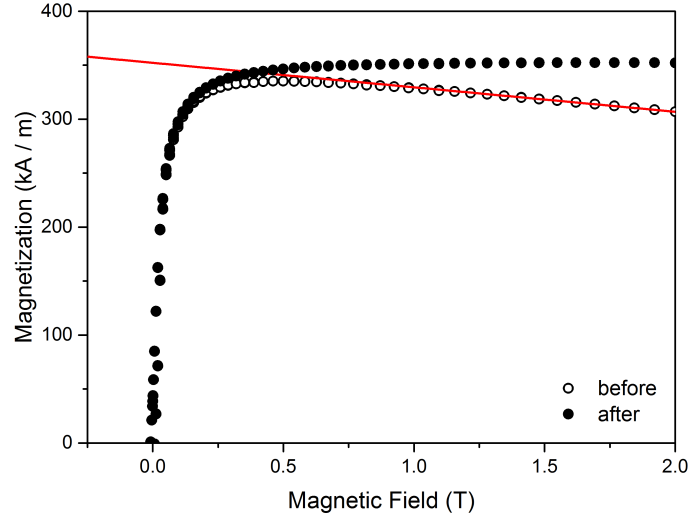
Figure 3.10: In-plane magnetization of FeGe sample showing diagmagnetic background from Si substrate (open circles). The linear background is subtracted and the saturation magnetization is determined from the intercept. The corrected data is shown as solid circles.

For the FeGe sample in Fig. 3.10 the saturation magnetisation M_s is found to be (360 ± 10) kA/m with the major source of error arising from the measurement of the sample area. To convert this to magnetisation per Fe (TM) atom the following relation was used $M_s = M_s(\mu_B)n_{TM}\mu_B$, where $M_s(\mu_B)$ is the magnetisation in μ_B per TM atom, n_{TM} is the density of Fe (TM) atoms per unit cell (4 Fe $/\alpha_{FeGe}^3$) and μ_B is the Bohr magneton. Using this relation a value of (0.982 ± 0.007) μ_B per Fe atom is found.

To determine the magnetic ordering temperature T_c, SQUID-VSM measurements were used. Figure 3.11 a) shows the magnetisation M as a function of temperature T and dM/dT for a $Fe_{0.6}Co_{0.4}Ge$ sample. T_c can be estimated from the minimum in dM/dT as indicated by the dashed line in Fig. 3.11 a), this minimum corresponds with the onset of magnetic ordering and has been used to identify T_c in bulk $Fe_{1-x}Co_xGe$ [29]. Figure 3.11 b) shows a measurement of the AC susceptibility χ_{ac} for a $Fe_{0.6}Co_{0.4}Ge$ sample. For these measurements the temperature position of the peak corresponding to a divergence in the susceptibility, shown by the dashed line, was used to identity T_c. This peak corresponds to a change in magnetic phase from the paramagnetic to helimagnetic phase and has been shown to identify T_c in B20 materials [42, 48, 62].
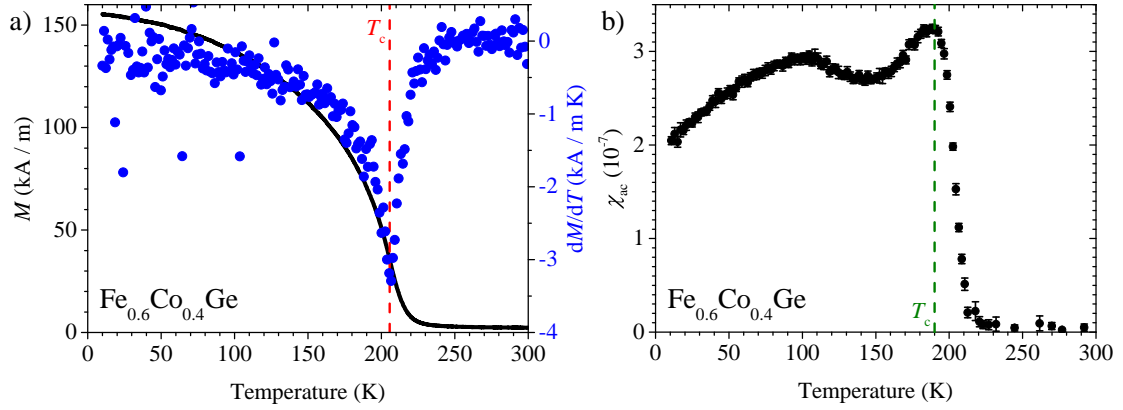
Figure 3.11: a) Magnetisation M measured with applied field of 100 mT as a function of temperature and dM/dT for a $Fe_{0.6}Co_{0.4}Ge$ sample. b) AC susceptibility χ_{ac} measured with applied DC field of 2 mT with 1 mT AC field at 23 Hz as a function of temperature for a $Fe_{0.6}Co_{0.4}Ge$ sample. Dashed line indicates T_c for each measurement.

3.7 Magnetotransport measurements

Magnetotransport measurements characterize the behaviour of a material's longitudinal and transverse (Hall) conductivity when under an applied magnetic field and with respect to the orientation of the applied field to the current direction.

The measurements were performed using an Oxford Instruments cryostat between temperatures of 5 K and 300 K. The setup of the cryostat consists of a variable temperature insert (VTI) submerged in a liquid helium reservoir which in turn is surrounded by a liquid nitrogen jacket. The sample is attached to a measurement stick which is inserted into the VTI and a vacuum is maintained within the VTI using a rotary pump. A needle valve connects the inside of the VTI or sample space to the He reservoir and regulates the flow of He. Temperature within the sample space is regulated by the incoming flow of He, the vacuum pump and a heater placed at the base of the VTI. Temperature is measured independently by sensors placed at both the base of the VTI and at the sample location. At the base of the cryostat, a superconducting magnet is able to produce fields up to ± 8 T, thus allowing a large range of temperatures and field conditions.

The measurements presented here use a 4-point probe DC setup. Current was provided using a Keithley 6221 current source and measurements were made using a Keithley 2182A and 182 nano-voltmeter. In general, measurements were made using a DC current reversal to account for any zero voltage bias due to thermal EMF.

3.7.1 Hall bar fabrication

For accurate longitudinal and Hall resistivity measurements a well defined current path and known contact separation is required. For thin films this can be achieved to nano-scale accuracy with thin film lithography. Hall bar devices were fabricated using ultra-violet (UV) photolithography allowing μm scale features. An 8-contact bar with 20 μm width and 10 μm contact spacing was chosen. The Hall bars were fabricated within the Leeds condensed matter physics group by S. Sugimoto and C. Morrison with the following procedure. S1813 resist was coated onto the sample at 4 krpm for 40 s. It was then soft baked at 115°C for 3 min. A pattern mask was used with an exposure dose of 13.7 mW/cm^2 for 3.5 s. It was then developed with MF319 for 90 to 105 s and de-ionised water was used to rinse. Ar ion milling was used to remove the unwanted material. Finally the sample was cleaned with acetone at 60°C for 10 min to remove the resist. An electron micrograph image of a finished Hall bar device is shown in Fig. 3.12.
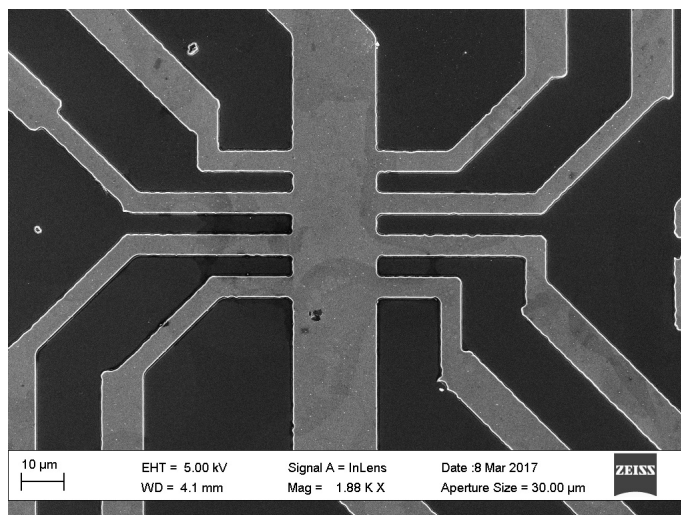
Figure 3.12: Scanning electron microscope image of 20 μm width Hall bar device (Image taken by G. Stefanou).

3.7.2 Longitudinal resistivity

Longitudinal resistivity was measured on both sheet films and pattered Hall bar samples. For sheet films the van der Pauw method [63] was used. This method allows the resistivity of an arbitrary shaped film to be found by measuring two temperature dependent resistances along different edges of a sample [63]. Aluminium wires were bonded to the corner edges of a square cut from the parent film and a four-point resistance measurement was taken as a function of temperature with current applied along one edge. The sample was cooled from room-temperature to 5 K at which point the current path was switched to another edge and the resistance was again measured on warming back to room temperature. An example of measurements taken using this method are shown for three FeGe samples in Fig. 3.13. Here each film, $t_{\text{film}} \sim 90$ nm has a residual resistivity ratio of ~ 8, this is an indication of film quality and consistent with reported values [41, 42] and also shows consistency between film growths.

For the patterned Hall bar samples, aluminium wires were bonded to the designated pads on the devices and current was applied along the bar, while voltage measurements were made using two contacts from a single side spaced 30 μm apart.
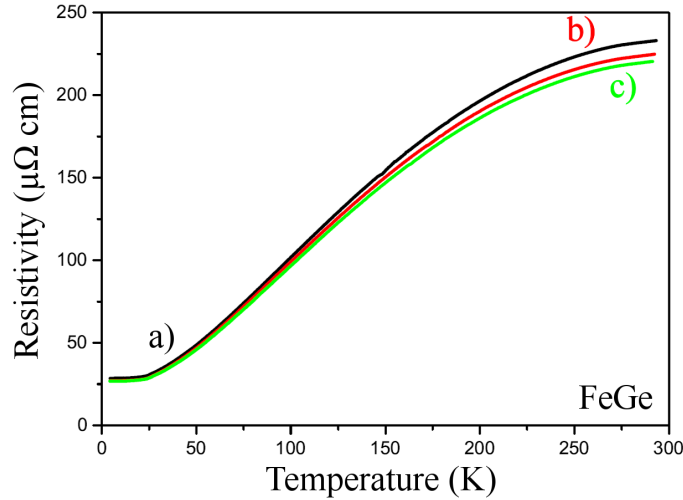
Figure 3.13: Resistivity as a function of temperature for three FeGe films with $t_{\text{film}} \sim$ 90 nm. Each film has a similar residual resistivity ratio of a) 8.17, b) 8.34 and c) 8.24 indicating consistent growth quality between films.

3.7.3   Magnetoresistance and Hall effect measurements

Magnetoresistance (MR) describes the change in resistivity when a magnetic field is applied to a material. MR measurements were performed using the Hall bar devices with an applied field perpendicular to the plane of the film. Figure 3.14 shows the orientation of a Hall bar device and the resistivity ρ_{xx} was measured using the relation

$$\rho_{xx} = \frac{V_{xx}}{I}\frac{wd}{l},\tag{3.8}$$

where V_{xx} is the longitudinal voltage, I is the applied current, w is the Hall bar width, d is the film thickness and l is the contact separation.
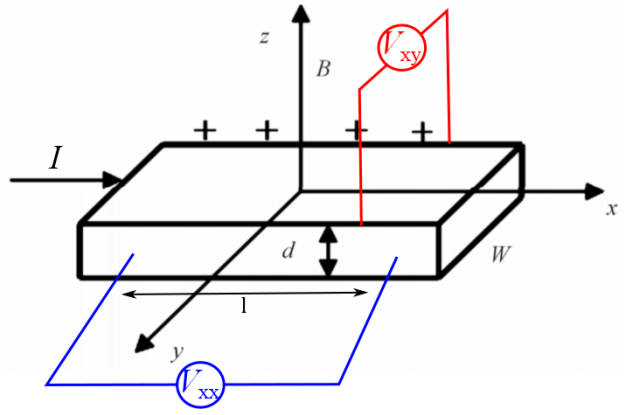
Figure 3.14: Diagram of Hall-bar orientation with applied magnetic field perpendicular to the film plane. Longitudinal resistivity is measured along the current direction I using V_{xx} and transverse Hall voltage is measured perpendicular to this direction using V_{xy}. (Figure adapted from Ref. [64])

The Hall effect measurements were performed simultaneously with the MR. The Hall voltage was measured transverse to the current using a pair of terminals opposite one another as shown in Fig. 3.14. The transverse voltage is used to measure ρ_{xy} and is given by

$$\rho_{xy} = \frac{V_{xy}d}{I},\tag{3.9}$$

where V_{xy} is the Hall voltage. This voltage is due to the action of the Lorentz force which acts to deflect charge carriers moving through a perpendicular magnetic field. The Hall voltage is proportional to the applied field through

$$V_{xy} = \frac{I\mu_0 H}{nde},\tag{3.10}$$

where H is the applied field, n is the charge carrier density and e is the electron charge. The Hall coefficient gives a measure of the Hall effect and is given by

$$R_0 = \frac{-1}{ne}. \tag{3.11}$$

3.8 Summary

In this chapter the experimental methods that will be used in this thesis to explore the physical properties of $Fe_{1-x}Co_xGe$ have been presented.

As the material we have chosen to investigate requires a specific crystal structure to observe the magnetic properties that are of interest, each step required in the film growth up to the sample characterisation is important to verify the material we are using is of good quality and representative of the B20 $Fe_{1-x}Co_xGe$ for the subsequent magnetic and transport studies.

CHAPTER 4

Sample Characterisation

4.1   Introduction

In this chapter the structural characterisation of the $Fe_{1-x}Co_xGe$ films used for this study will be discussed. Over the course of this project many samples were grown and the quality of the films produced was improved. High quality samples were defined as films that showed an epitaxial B20 crystal phase with little or no impurity phases with low surface roughness ($\sim$ a few nm) and good interface quality (presence of interference fringes for XRR and PNR). For the FeGe films, in addition to the qualities mentioned, samples that showed a magnetic ordering temperature close to the bulk crystal value and resistivity responses close to what has been shown in literature were additional criteria. From the samples produced, films that showed the best of these properties were chosen for further study.

The sample sets chosen were a range of FeGe films with varying thickness and a collection of $Fe_{1-x}Co_xGe$ films with $0.1 \leq x \leq 0.8$ and CoGe ($x = 1$). The thickness chosen for the $Fe_{1-x}Co_xGe$ films was $\sim$ 70 nm, to remain consistent with the initial growth thickness chosen for the FeGe films, where 70 nm is $\sim$ 1 period of the helix wavelength (λ_h). For the pure FeGe studies the films with varying thickness contained films of thickness t_{film} = 23.2 nm, 40.0 nm, 67.8 nm, 93.3 nm, 140 nm, 186 nm and 280 nm. The 67.8 nm sample was the film used in Ref. [44]. For the $Fe_{1-x}Co_xGe$ films the 67.8 nm film from the FeGe set was used as $x = 0$ to complete the range of x for the composition study.

First we discuss the crystal structure to be investigated and look at its associated properties. We then look at the difficulties encountered while growing epitaxial B20 films on Si. Next the X-ray results, revealing the structure of our films, are presented and finally a summary of the sample sets used for this thesis are given.

4.2 B20 crystal structure

The focus of this thesis is on materials that crystallise in the B20 crystal structure, which is a classification belonging the Strukturbericht (structure report) system. This corresponds to the space group $P2_13$, which is No. 198 in the International Tables for Crystallography and cP8 in the Pearson symbol notation. For consistency with previous literature the structure of the $Fe_{1-x}Co_xGe$ presented here will be referred to as B20.

The B20 structure for FeGe and other transition metal (TM) mono-germanides and silicides (e.g. MnSi, MnGe, etc.) is composed of TM elements and Group 14 (Group IV) elements (most notably Si, Ge) in a 1:1 ratio. The unit cell is cubic and contains eight atoms, four TM atoms and four Group 14 atoms and a diagram of the B20 unit cell is shown in Fig. 4.1 where the TM atoms are shown in red and the Group 14 atoms are shown in blue. The relative position of the atoms (Wyckoff 4a) are given by $(x, x, x); (\frac{1}{2} + x, \frac{1}{2} - x, x); (x, \frac{1}{2} + x, \frac{1}{2} - x); (\frac{1}{2} - x, x, \frac{1}{2} + x)$ where $x_{Fe} = 0.135(1)$ and $x_{Ge} = 0.842(1)$, which have been determined experimentally [18]. The lattice constants have been well measured for the parent materials of $Fe_{1-x}Co_xGe$ in bulk samples and are FeGe 4.700 Å [4] and CoGe 4.631 Å [17].

However, the most notable property of this structure is that it is chiral. The chirality is the basis of what is often described in this material as lacking inversion symmetry or being non-centrosymmetric. When the crystal structure is inverted it changes from one chirality to the other, e.g. going from a right-handed spiral to a left-handed one. This asymmetry in the crystal leads to the Dzyaloshinskii-Moriya interaction, which produces the many interesting magnetic features.

Due to the recent interest in the B20 materials, thin films have been grown to allow control over the composition of the material and allow fabricated devices to be produced to investigate the magnetic and transport properties. The growth of B20 films on Si substrates began with MnSi [38] and the procedure was then used at Leeds to produce FeSi and $Fe_{1-x}Co_xSi$ [53, 65]. Thin films of B20 FeGe have been grown previously at Leeds by DC magnetron sputtering [42] following the method used in [41] and using this method textured films of B20 FeGe were produced, however to produce epitaxial films a MBE growth method was adopted as used in $Fe_{1-x}Co_xSi$.
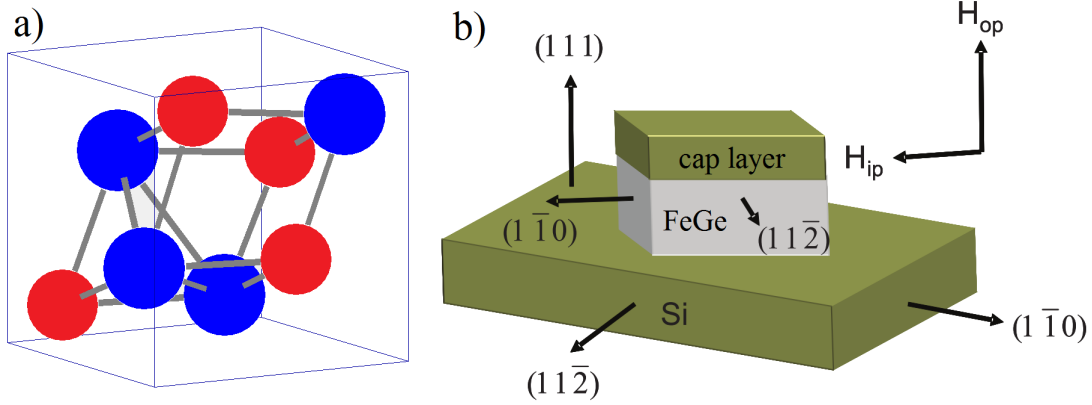
Figure 4.1: a) Diagram of B20 unit cell. TM atoms shown in red and Group 14 (Group IV) atoms shown in blue. b) Diagram of FeGe on Si substrate (Figure adapted from Ref. [56]).

To grow epitaxial films a suitable substrate is required. Using Si(111) substrates, B20 FeGe (and other B20 silicides and germanides) grow along the [111] direction with a 30° in-plane rotation with respect to the Si surface [38, 42] as seen in Fig. 3.2 c). The following lattice relationships are expected: FeGe[111]‖Si[111] and FeGe[1$\bar{1}$0]‖Si[11$\bar{2}$], as found in MnSi [66].

Si has a lattice constant α_{Si} of 5.431 Å which for epitaxial growth would produce a lattice mismatch of $(\alpha_{Si}- \alpha_{Si} \cos(30°))/\alpha_{FeGe} = $ -0.07%.

Additionally the semiconductor properties of the substrate allowed the resistivity to be tailored to allow transport measurements of the films grown by having an insulating substrate.

4.3 Film growth optimisation

The binary alloy Fe-Ge has a very complex phase diagram [67] and B20 FeGe forms at 50 atomic % Fe to Ge. At 50% composition there are three possible FeGe polymorphs that can crystallise: monoclinic, cubic B20 and hexagonal B35 FeGe [18]. As we are interested in studying only B20 FeGe these other phases are considered impurities in our films. Additional impurity phases can also occur from off-stoichiometric growth, such as Ge crystallite formation. As these impurity phases can be produced if the correct growth conditions are not met, the growth procedure had to be optimised to produce

single phase films. The individual techniques used to optimise the growth procedure are detailed here and the final growth method used was given in Sect. 3.2.2.

4.3.1   RHEED results

The RHEED technique allows the crystal growth to be monitored in real-time allowing for determination of crystal phase and quick adjustments to growth parameters. For our films one of the most important qualities required, in addition to crystal phase, was interface quality to use techniques such as PNR for later magnetic studies.

Results are shown for two compositions of x, $Fe_{0.7}Co_{0.3}Ge$ and $Fe_{0.3}Co_{0.7}Ge$ in Fig. 4.2, with various stages within the growth procedure shown. During the initial stages of growth, small quantities of material were deposited in steps to encourage crystallisation at the interface. It was found previously that the B20 RHEED pattern emerged naturally during growth, assuming the correct stoichiometry, however this was usually after several nm of deposition and was reflected in poor XRR measurements. By using this procedure it was found that with additional time at the early stages of growth, the B20 pattern was able to emerge immediately and formed a seed for the subsequent layers. Approximately 1 nm of material as deposited was used for each step, after crystallisation this corresponded to slightly less. One step was defined as a monolayer (ML) due to this amount being consistently repeatable, however this does not correspond to 1 atomic ML. Fig. 4.2 a) shows the reconstructed Si (7×7) pattern before deposition, this process takes places at elevated temperatures and the substrate was cooled to approximately room temperature ($< 50°C$) after verification of this pattern 1 ML was deposited and the substrate was heated. The observed pattern is shown in b), this was then monitored to ensure no change in phase until the growth was finished and a final image is shown in c). Figure 4.2 shows a similar process for $Fe_{0.3}Co_{0.7}Ge$, where d) shows after 1 ML of deposition, e) after 3 ML and f) after growth. What can be seen for both $Fe_{0.7}Co_{0.3}Ge$ and $Fe_{0.3}Co_{0.7}Ge$ is the emergence of a RHEED pattern after the first ML of deposition and the transition from a 'spotty' pattern in b) and e) to the well defined streaks in c) and f) indicating a change from 3D islands to a flat surface with small domains [68].

Fe$_{0.7}$Co$_{0.3}$Ge   Fe$_{0.3}$Co$_{0.7}$Ge
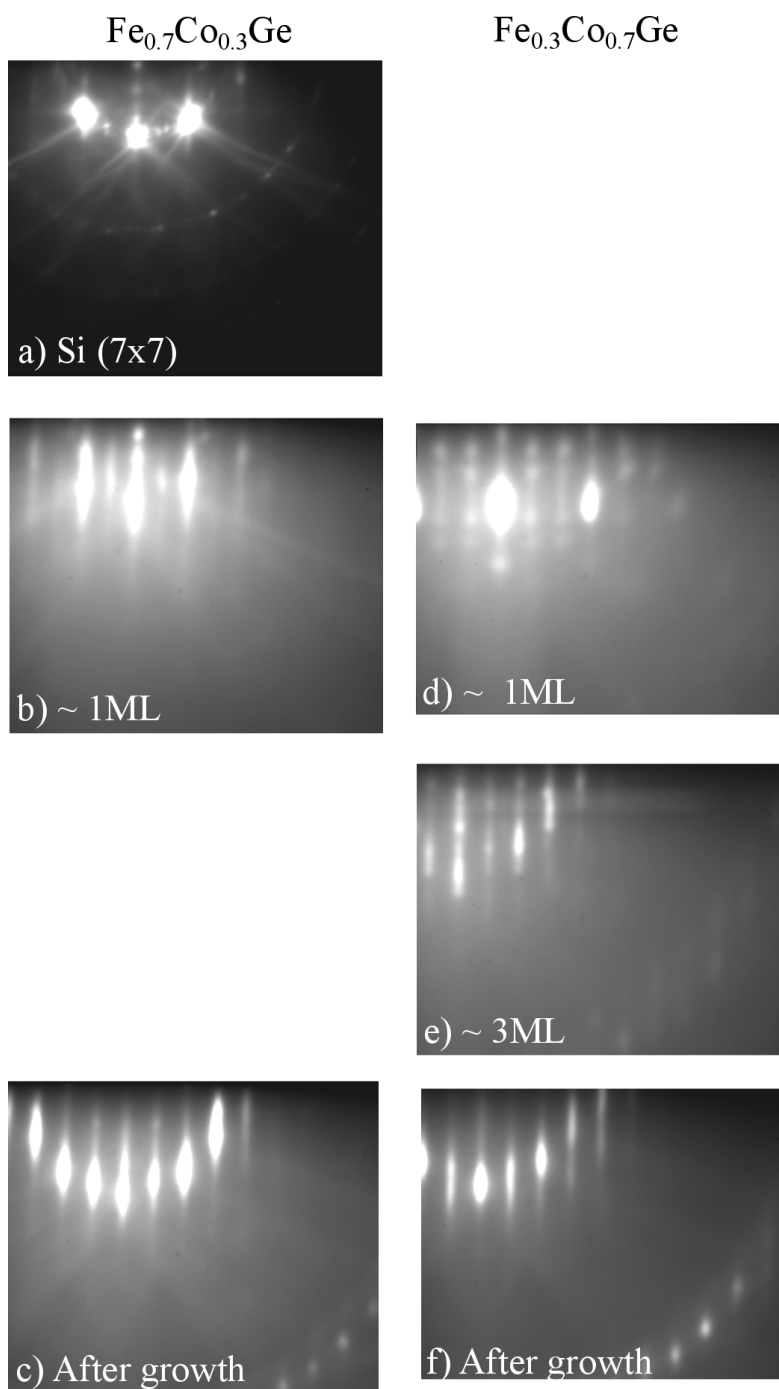
Figure 4.2: RHEED patterns taken from a Fe$_{0.7}$Co$_{0.3}$Ge and a Fe$_{0.3}$Co$_{0.7}$Ge film before, during and after growth. For Fe$_{0.7}$Co$_{0.3}$Ge a) Si (7×7) reconstruction of the film surface before deposition, b) formation of pattern after 1 ML (~ 1 nm of deposited material), c) after growth. For Fe$_{0.3}$Co$_{0.7}$Ge a) after ~ 1 ML of deposition, b) after ~ 3 ML and f) after growth. For both samples the after growth images, c) and f) show sharp streaks indicative of an ordered surface.

4.3.2 LEED results

One of the *in situ* methods used to identify the material grown was LEED. This was used before and after film deposition to verify the crystal phase grown and the epitaxy of the layer. Results from a reconstructed Si (7×7) surface and after film deposition for various compositions of x are given in Fig. 4.3 a) and b-f) respectively. The LEED technique uses an electron beam fired directly normal to the sample surface and the beam emitter and mounting arm can be seen by the obscuring shadow. In Fig. 4.3 a) the Si (7×7) reconstruction is shown and indicates a clean and well ordered surface. In b) the result for an FeGe film is shown, this pattern was shown in Ref. [44] and is consistent with previous B20 LEED patterns, such as for MnSi [69] and $Fe_{1-x}Co_xSi$ [53], which is expected due to the consistent crystal structure and growth medium. For c) to f) the results for $Fe_{0.7}Co_{0.3}Ge$, $Fe_{0.5}Co_{0.5}Ge$, $Fe_{0.3}Co_{0.7}Ge$ and and CoGe are shown, each result shows the same pattern structure and the same orientation indicating a consistent phase between the samples, which shows the B20 phase is maintained with varying x and also implies the crystal epitaxial relation is preserved.
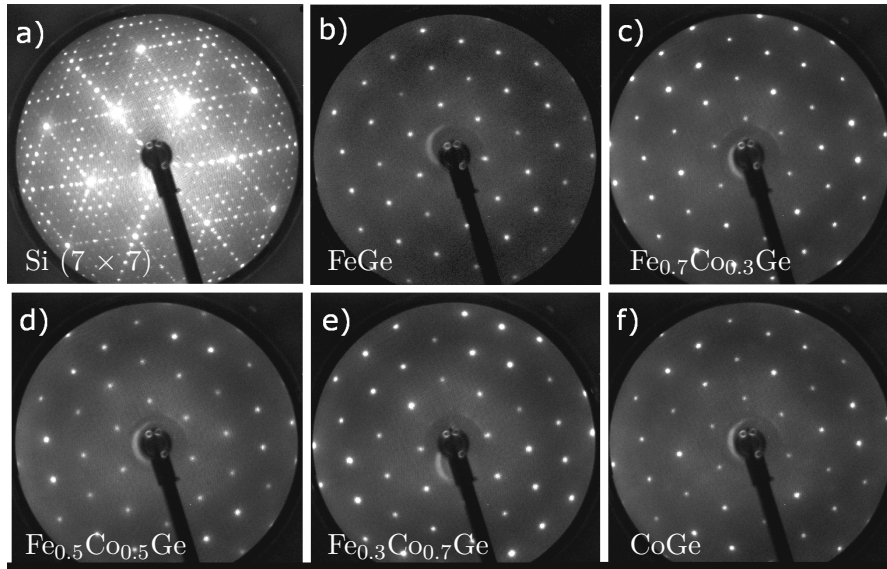
Figure 4.3: Low-energy electron diffraction images taken at 100 eV from; a) reconstructed Si (7×7) surface prior to film deposition and b-f) surface of $Fe_{1-x}Co_xGe$ film after deposition for b) FeGe, c) $Fe_{0.7}Co_{0.3}Ge$, d) $Fe_{0.5}Co_{0.5}Ge$, e) $Fe_{0.3}Co_{0.7}Ge$ and f) CoGe. Results for $Fe_{1-x}Co_xGe$ films, b-f), show consistent surface LEED pattern indicating crystal phase is maintained throughout the group.

Quantitative analysis to identify the lattice parameter was attempted, however the results appeared to be unreliable when comparing between samples due to misalignment between measurements of the substrate and grown film and the final structure measurements were made using XRD as shown later in Sect. 4.4.1. However, LEED proved to be an invaluable tool in the early stages of growth by allowing quick identification of the surface structure present.

4.3.3   TEM results

Transmission electron microscopy (TEM) was used to directly image the atomic structure in the films grown in both cross-section and plan view orientations. In the cross-section orientation the epitaxy of the film grown and the spacing between the lattice plane could be directly observed. The cross-section image for an early FeGe film (sample not used for further study in this thesis) is shown in Fig. 4.4, viewed along the FeGe [110] direction. Although the sample was grown before optimisation of the growth method, epitaxy of the FeGe layer can be seen with respect to the Si substrate, planes within the FeGe can be seen to lie parallel to the Si which is expected for growth along the [111] direction. By using a linescan, as shown in Fig. 4.4 c) and estimate for the lattice constant could be found using $\alpha_{\text{FeGe}} = \sqrt{3}d_{111}$. For this sample the value of $\alpha_{\text{FeGe}} = (4.6 \pm 0.15)$ Å.

Plan view TEM was used to examine the chiral grain structure found in the films produced. The film is expected to be composed of both right- and left-handed chiral grains due to crystal growth along the Si [111] axis, as with this method, neither grain chirality is favoured [38, 44, 65]. Grains corresponding to each chirality can be identified using dark field imaging by observing a particular crystal axis where the difference in chirality produces a splitting in the position of the associated diffraction spot [38]. Figure 4.5 a) shows the diffraction pattern along the [111] direction and in b) by looking along the [321] direction, splitting can be seen, corresponding to the [111] direction for each chirality. By taking a dark field image isolating each single spot the crystal grains associated to each chirality can be detected.
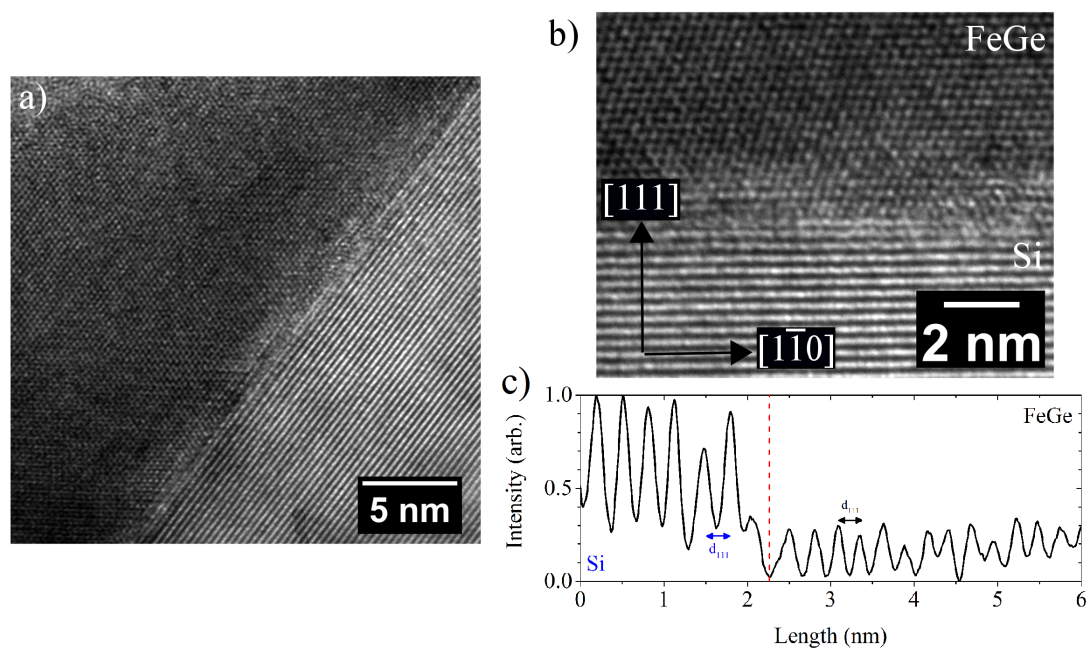
Figure 4.4: a) Cross-section transmission electron micrograph of an early FeGe film viewed along Si $[11\bar{2}]$ direction. b) Close-up of FeGe/Si interface taken from a). c) Vertical linescan from b) showing inter planar spacing. Contrast shows FeGe as darker regions and Si substrate as lighter region. (Images taken by M. Mclaren).

Figure 4.6 shows the resulting dark field images when aligned to each chirality, the left-handed and right-handed structures for FeGe are shown in a) and b) and for $x = 0.5$ in d) and e) respectively. Using each chirality image an overlay of the two is shown in c) for FeGe and f) for $x = 0.5$ showing the chiral grain structure. The grain size appears to vary considerably across the image with some up to ~ 500 nm in diameter, however the average size appears to be closer to ~ 200 nm.
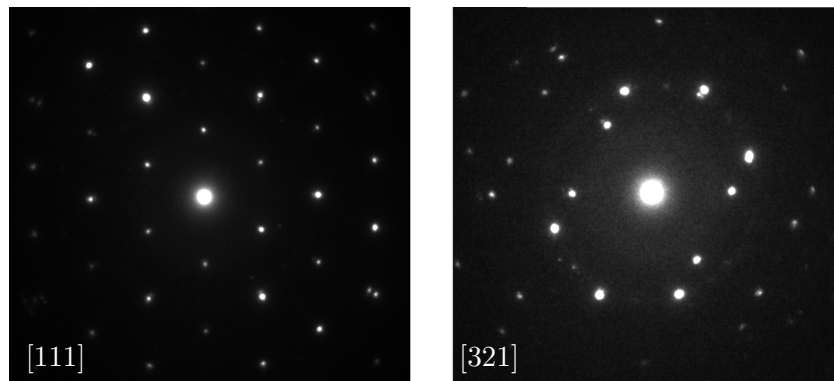
Figure 4.5: Plan view transmission electron micrographs of diffraction patterns taken from an early FeGe sample along the a) [111] direction and b) [321] direction. (Images taken by M. McLaren).
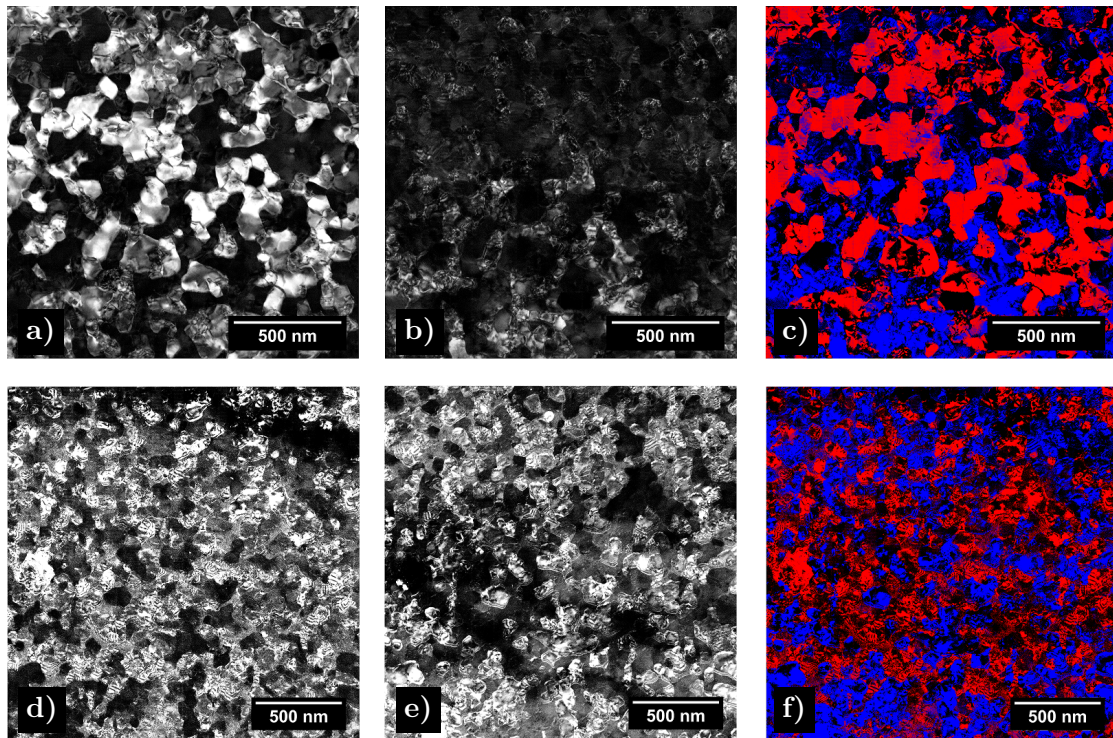
Figure 4.6: Plan view dark-field transmission electron micrographs aligned to split diffactions spots for left-handed and right-handed chirality for a,b) FeGe and and d,e) $x = 0.5$ films. Colorised overlay of both chiralities showing chiral grain structure is shown in c) for FeGe and f) for $x = 0.5$. Short horizontal lines are artefacts from the image capture. (Images taken by Z. Aslam).

4.3.4   X-ray analysis

To determine the expected diffraction peaks produced by a $Fe_{1-x}Co_xGe$ film and identify the peaks produced by possible impurity phases, diffraction simulations were performed using the PowderCell [70] software package. Figure 4.7 shows the expected peak positions for the Si substrate, B20 FeGe and neighbouring phases as well as three XRD data sets from FeGe films showing various impurities. All three data sets show the expected substrate peaks Si(111) $2\theta = 28.44°$, Si(222) $2\theta = 58.86°$ and the film peak B20 FeGe (111) $2\theta = 32.98°$ and in a) (blue) the B20 FeGe (222) $2\theta = 69.19°$ can also be seen. However in addition to these additional impurity peaks are seen. In a) a peak corresponding to the B20 FeGe (201) $2\theta = 43.00°$ is seen indicating some texture in the film. In b) (red) the impurity peak of a Ge (111) $2\theta = 27.28°$ peak is seen showing an off-stoichiometric growth. In c) (black) a mixed film is seen with a peak corresponding to the B35 FeGe (110) $2\theta = 35.87°$ is seen.
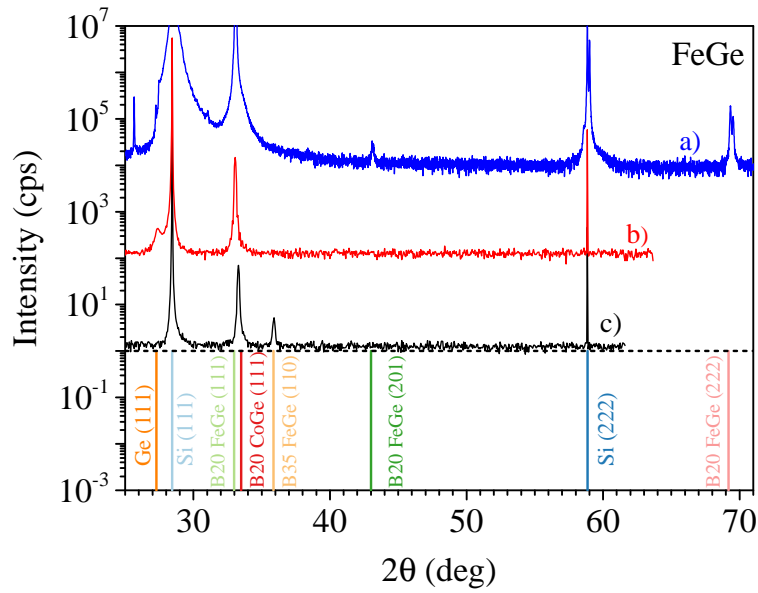
Figure 4.7: X-ray diffraction measurements for FeGe films containing impurity phases with simulated expected peak positions for Si substrate, B20 FeGe and the most common impurity phases. Data sets have been offset vertically for clarity. a) (blue) Textured FeGe film containing (111) and (201) orientations. b) (red) B20 FeGe film containing Ge (111). c) Mixed phase film containing B20 and B35 FeGe. Data set a) was acquired without a Ge-monochromator and shows higher intensity peaks.

4.4 Characterisation results for sample sets

From the samples produced a small number were chosen for further study. These samples were chosen based on their composition and quality as defined earlier in Sect. 4.1. The structural characterisation by X-ray techniques for these sample sets are given in the following sections.

4.4.1 X-ray diffraction

To verify the crystal phases present in the films, X-ray diffraction (XRD) measurements were used. A range of 25° to 75° was used to cover the range of the $Fe_{1-x}Co_xGe$ (111) plane reflections and broad enough to cover any peaks produced from nearby impurity phases shown in section 4.3. Since the growth is along the (111) direction, for FeGe, a Bragg peak corresponding to the B20 (111) peak was expected at $2\theta = 32.98°$. Figure 4.8 shows the measured (111) Bragg peak for FeGe at varying film thickness. For the thinnest film, 23.2 nm, a broad peak can be seen, as the film thickness is increased the centre peak becomes sharper. The arrows indicate the appearance of Laue oscillations due to reflections from the surface and substrate interface showing parallel interfaces. The spacing of the Laue oscillations, which like Kiessig fringes shown before, are inversely proportional to the layer thickness and the frequency can be seen to increase with the film thickness which is consistent.
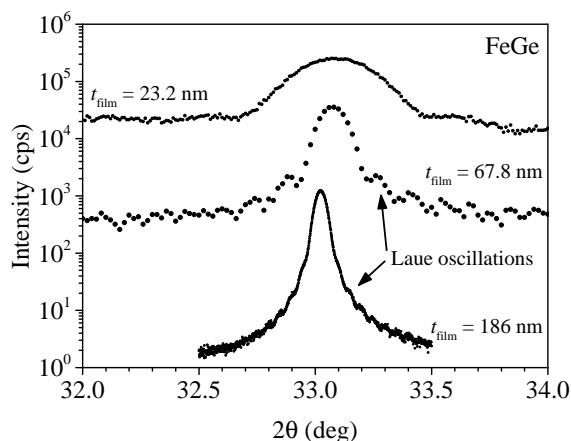
Figure 4.8: X-ray diffraction measurements for FeGe films with varying thickness. Arrows indicate appearance of Laue oscillations. Data sets have been offset vertically for clarity.
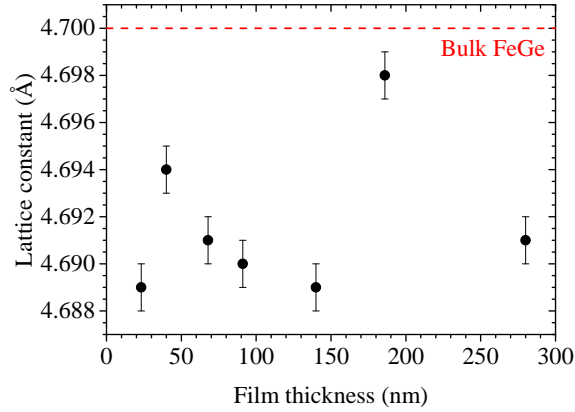
Figure 4.9: Cubic lattice constants α_{FeGe} for FeGe films with varying thickness. Bulk crystal value for FeGe shown by dashed line.

The resulting cubic lattice constant α_{FeGe} for the FeGe films are given in Fig. 4.9 including films not shown previously. The measured out-of-plane lattice plane spacing d_{111} was calculated using Eq. 3.1 using the angular position of the FeGe (111) peak and converted to the cubic constant through $\alpha_{\text{FeGe}} = \sqrt{3}d_{111}$. Due to the induced strain on the film from the substrate the lattice constant is found to be reduced when compared with the bulk value of 4.700 Å [7]. The expected trend for epitaxial films deposited on a substrate with a lattice mismatch is for thinner films the induced strain is expected to be at its greatest and as the film thickness is increased the lattice is able to relax and the strain to reduce. From the lattice constants shown in Fig. 4.9 no discernible trend could be seen. The average is found to be (4.692 ± 0.003) Å which is a reduction of $\sim$ 2% indicating compressive strain.

The XRD data for each $\text{Fe}_{1-x}\text{Co}_x\text{Ge}$ film composition is shown in Fig. 4.10. A single peak in the vicinity of 33 $^\circ$ indicates the B20 (111) reflection which for $\text{Fe}_{1-x}\text{Co}_x\text{Ge}$ using bulk values varies from; FeGe $2\theta = 32.98°$ to CoGe $2\theta = 33.49°$. For each film a single Bragg peak corresponding to the B20 phase is seen, showing each film is single phase. As for FeGe, a cubic lattice vector is assumed due to the small strain induced by the substrate and the lattice constants are shown in Fig. 4.11. α_{FeCoGe} is found to decrease with increasing x as expected from the Vegard's law [71] approximation shown by the dashed line. The values are also found to be lower than the expected values indicating there is strain present in the system.
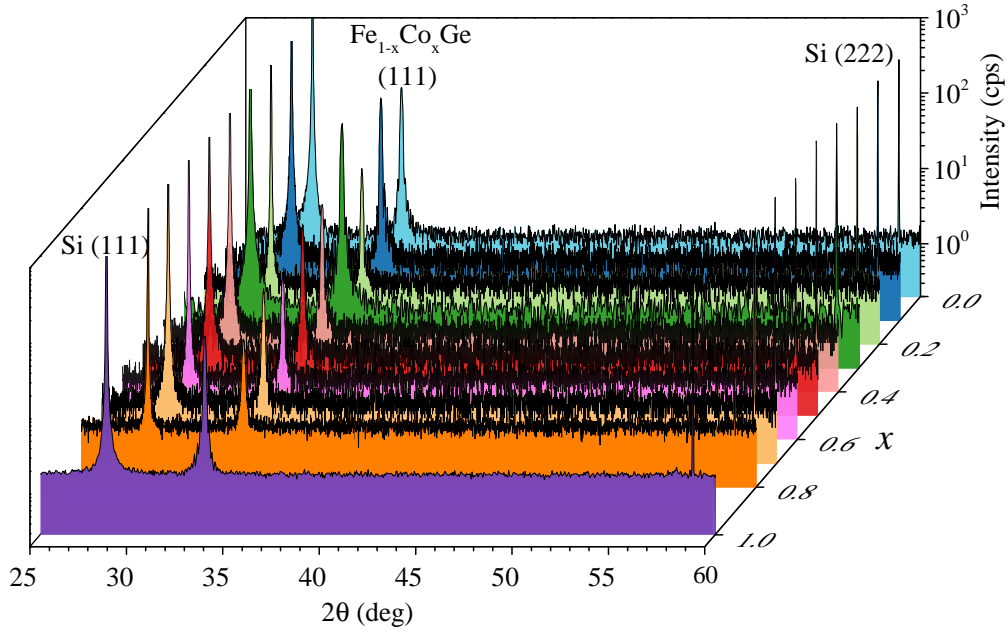
Figure 4.10: Summary of X-ray diffraction spectra for ~ 70 nm $Fe_{1-x}Co_xGe$ films with $0 \leq x \leq 1$ used in this study. For each data set of x only a single B20 $Fe_{1-x}Co_xGe$ (111) reflection peak is seen along with the substrate Si (111) and (222) reflections indicating a single phase film. The position of the B20 peak in 2θ is found to shift from $\sim 33°$ to $\sim 33.5°$ for FeGe to CoGe showing a reduction in the lattice constant.
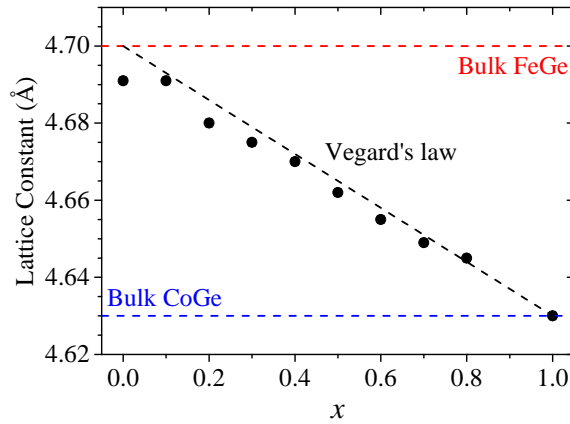
Figure 4.11: Resulting lattice constants for ~ 70 nm $Fe_{1-x}Co_xGe$ films with $0 \leq x \leq 1$. Cubic lattice constants calculated using out-of-plane lattice spacing from B20 reflection peak positions in Fig. 4.10 assuming a cubic unit cell. Dashed line shows Vegard's law approximation between bulk crystal values.

4.4.2 X-ray reflectometry

Film thickness, layer structure and interface quality were measured using XRR. The XRR data for FeGe films with varying thickness is shown in Fig. 4.12. Here a selection of films from 23.2 nm to ~ 140 nm are shown. The thicknesses for these films, with the exception of the 67.8 nm film, were calculated using the Kiessig fringe spacing. As the oscillation frequency of Kiessig fringes are inversely proportional to the film thickness, Kiessig fringes can be seen in all data up to 91 nm thickness, however for thicker films the fringes could not be resolved and so only an estimate for the film thickness is shown, calculated from the growth method. The dashed line in Fig. 4.12 shows the approximate θ_c taken from the data, each data set shows approximately the same θ_c indicating a uniform electron density (from Eq. 3.5) across the film thickness range.
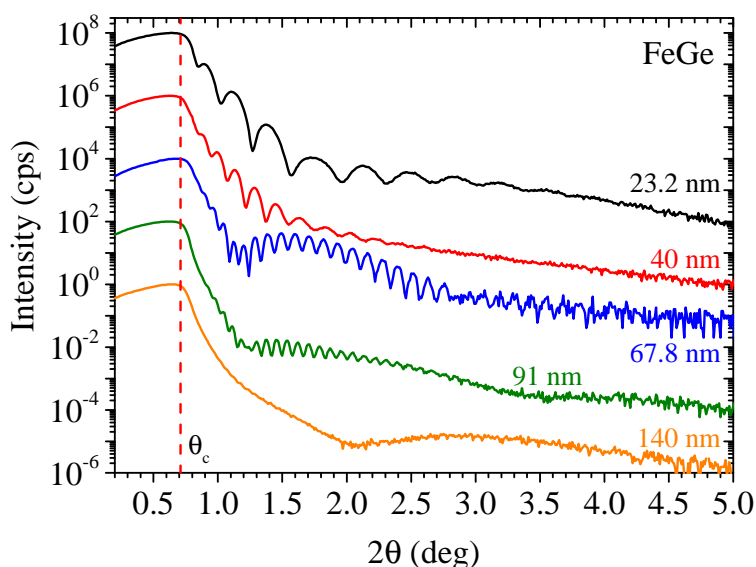
Figure 4.12: Summary of X-ray reflectometry measurements for FeGe films used in this study with varying thickness. Each film shows approximately the same θ_c, shown by the dashed line, indicating a constant electron density. After ~ 100 nm the Kiessig fringes become unresolvable and film thickness cannot be directly measured using this method. Data sets have been offset vertically for clarity.
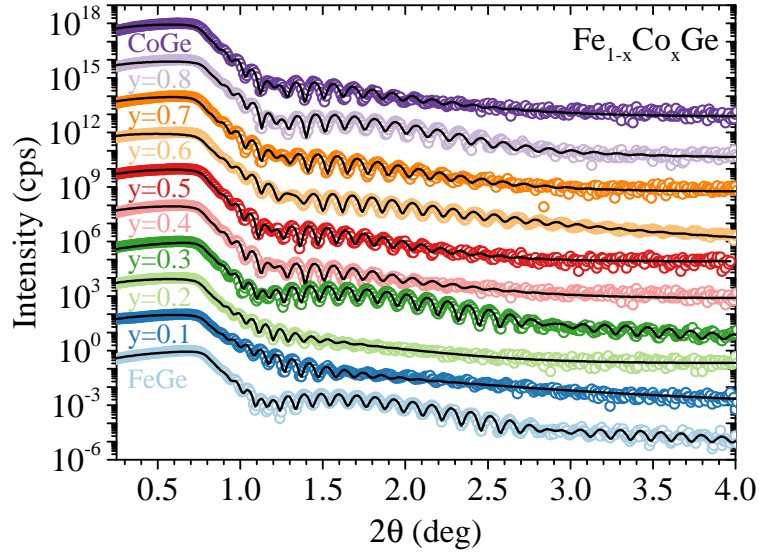
Figure 4.13: Summary of X-ray reflectometry measurements (open circles) for ~ 70 nm $Fe_{1-x}Co_xGe$ films used in this study with $0 \leq x \leq 1$ and corresponding fit (line). Data sets have been offset vertically for clarity.

The XRR data sets and corresponding fits (performed using GenX, see Sect. 3.4.2) for the $Fe_{1-x}Co_xGe$ films are shown in Fig. 4.13 for $0 \leq x \leq 1$, including the 67.8 nm FeGe film from Fig. 4.12. Excellent fits are produced using a single layer of homogeneous density material for each of the $Fe_{1-x}Co_xGe$ compositions and a cap layer where necessary.

4.5 Sample sets summary

A summary of the samples sets chosen for this thesis are presented here. Table 4.1 shows the film properties for the FeGe samples and Table 4.2 shows the film properties for the $Fe_{1-x}Co_xGe$ set. The α_{FeGe} and α_{FeCoGe} values are taken from the XRD data shown in Fig. 4.9 and Fig. 4.11 respectively. For the FeGe t_{film} the values shown are taken from Kiessig fits of the data shown in Fig. 4.12. For $Fe_{1-x}Co_xGe$ the various parameters; t_{film}, σ_{film}, t_{cap} and σ_{cap} are taken from the fits to the data shown in Fig. 4.13.

Table 4.1: FeGe sample set. Summary of values from XRD and XRR measurements for FeGe: lattice constant α_{FeGe}, film thickness t_{film} and film roughness σ_{film}.

α_{FeGe} (Å)	t_{film} (nm)	σ_{film} (nm)
4.689 (1)	23.2 (8)	0.6 (1)
4.694 (1)	40 (1.4)	2.0 (1)
4.691 (1)	67.8 (1)	2.6 (1)
4.690 (1)	91 (2)	0.7 (1)
4.689 (1)	140 (14)	-
4.698 (1)	186.0 (0.6)	-
4.691 (1)	280 (30)	-

Table 4.2: Fe$_{1-x}$Co$_x$Ge sample set. Summary of values from XRD measurements and XRR data fits for Fe$_{1-x}$Co$_x$Ge: lattice constant α_{FeCoGe}, film thickness t_{film}, film roughness σ_{film}, cap thickness t_{cap} and cap roughness σ_{cap} from $x = 0$ to 1. Samples $x = 0.1$, 0.2 and 0.3† were grown without cap layers. (⋆sample used for magnetometry and PNR measurements, †sample used for magnetotransport measurements).

x	α_{FeCoGe} (Å)	t_{film} (nm)	σ_{film} (nm)	t_{cap} (nm)	σ_{cap} (nm)
0	4.691 (1)	67.8 (2)	0.6 (1)	4.7 (1)	0.8 (0.1)
0.1	4.691 (1)	70.6 (4)	2.0 (1)	-	-
0.2	4.680 (1)	76.6 (8)	2.6 (1)	-	-
0.3⋆	4.675 (1)	64.1 (1)	0.7 (1)	4.7 (1)	0.9 (1)
0.3†	0.4676(1)	116(4)	-	-	-
0.4	4.670 (1)	63.3 (4)	2.2 (2)	4 (1)	0.7 (1)
0.5	4.662 (1)	65.9 (2)	2.2 (1)	4.1 (1)	0.9 (1)
0.6	4.655 (1)	63.6 (3)	1.9 (1)	3.7 (2)	0.5 (1)
0.7	4.649 (1)	61.8 (4)	2.1 (2)	3.8 (1)	0.7 (1)
0.8⋆	0.4644(1)	64.9(2)	0.8(2)	3(1)	1(1)
0.8†	4.645 (1)	62.2 (2)	0.6 (1)	4.5 (2)	1.4 (1)
1	4.630 (1)	63.3 (4)	2.2 (1)	4.0 (1)	0.6 (1)

4.6   Summary

The results presented in this chapter show epitaxial films of $Fe_{1-x}Co_xGe$ have been grown on Si substrate that display consistent single phase crystalline and homogenous layer structure. The films presented here show an improvement over the films grown previously via magnetron sputtering [42] as they are completely epitaxial. The growth by MBE has shown it is possible to control the presence of any impurity phases and also the addition of Co allowing a full range of $Fe_{1-x}Co_xGe$ films to be produced.

The XRD results confirm an epitaxial growth and the lattice constant expected for FeGe, they also show the films are under compressive strain. The results for the $Fe_{1-x}Co_xGe$ are similar and show the B20 phase is maintained throughout the group.

The XRR results show the films have a single layer structure and the B20 layer is homogenous indicating a good quality film. The $Fe_{1-x}Co_xGe$ films also show good interface quality from the XRR data with the presence of clear interference fringes, they also have and an average surface roughness of $\lesssim 2$ nm. These features show the films are suitable for magnetic characterisation by polarised neutron reflectivity which is presented in Chapter 5. In this chapter a summary of the results taken during sample growth were presented. From these results we can conclude that the films produced are the correct material and we are able to tune the composition and film thickness while maintaining good film quality. This shows the films are suitable for further study and we can continue in the subsequent chapters with the magnetometry and electrical transport properties.

CHAPTER 5

Magnetic Properties

5.1 Introduction

In this chapter the magnetic properties of epitaxial B20 $Fe_{1-x}Co_xGe$ films will be explored. The parent material B20 FeGe is a well known cubic chiral helimagnet [18] that is host to non-collinear magnetic phases due to the presence of DMI which is produced by its non-centrosymmetric crystal structure, whereas B20 CoGe is not ferromagnetic and has a diamagnetic ground state [33]. The group of compounds $Fe_{1-x}Co_xGe$ is able to maintain the same B20 crystal structure (see Sect. 4) and the magnetic properties are expected to evolve with increasing x.

First we investigate the magnetisation properties and look at how the magnetic ordering temperature and saturation magnetisation depend on x, the Co concentration. Then the helical magnetic structure is explored, first with indirect evidence using features in the measured magnetisation hysteresis and second using PNR to directly identify the helical structure.

5.2 Magnetic properties

Magnetic measurements were performed using a Quantum Design MPMS with temperatures ranging from 5 K to 300 K and with applied fields up to ± 6 T. Measurements were made with two different sample orientations; with the field applied in-plane (IP), parallel to FeGe [110] ($H \parallel [1\bar{1}0]$) and with the field applied out-of-plane (OOP), parallel to FeGe [111] ($H \parallel [111]$). Samples of approximately 2.5 mm × 2.5 mm from each film composition were cut from the parent film and used for the measurements.

5.2.1 Magnetic ordering temperature

The temperature dependence of the magnetic ordering temperature T_c was determined using two methods, using the static (DC) susceptibility $\chi_{dc} = dm_{dc}/dT$ and the dynamic (AC) susceptibility $\chi_{ac} = dm_{ac}/dT$. This was due to some features appearing in χ_{ac} that did not occur for each x value and so both methods were required to observe T_c for all compositions. The magnetisation as a function of temperature with field applied IP is shown in Fig. 5.1 at 10 mT and the T_c was taken from the minimum in χ_{dc}.

Figure 5.2 shows the AC susceptibility χ_{ac} for $Fe_{1-x}Co_xGe$ with field applied IP. A static field of 2 mT and an alternating field of 1 mT at 23 Hz was used, with the exception of a 5 mT field used for $x = 0.4$ to produce a clearer peak. The susceptibility
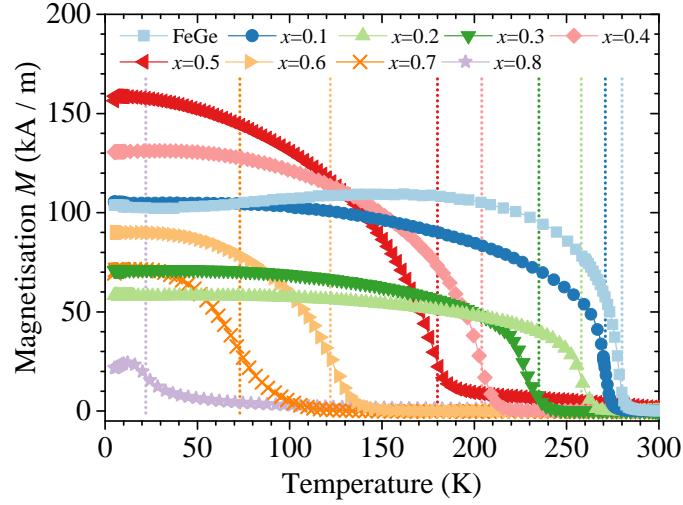
Figure 5.1: Magnetisation M as a function of temperature dependence for $Fe_{1-x}Co_xGe$ with applied in-plane field at 100 mT. Dotted lines with corresponding colour show T_c for each composition determined from minimum in $\chi_{dc} = dM/dT$.

shown for FeGe ($x = 0$) in Fig. 5.2 is consistent with literature and shows a narrow peak as expected. The shape of the χ_{ac} curve shows a peak followed by a decreasing susceptibility with temperature which is indicative of a non-collinear magnetic phase and in this case the onset of the helical phase. The temperature at which the peak occurs is define as the ordering temperature for this method. For the remaining $Fe_{1-x}Co_xGe$ films $0.1 \leq x \leq 0.6$ a similar form can be seen, however the behaviour becomes more complex with increasing x. For $x > 0.4$ and 0.5, a small dip is seen after the initial peak and a second broad peak is seen. The position of the highest temperature peak was used to determine the T_c for the $Fe_{1-x}Co_xGe$ films and in the case of $x = 0.6$ the inflection point seen at ~ 130 K.

A comparison of the T_c determined from the two methods, the minimum in the peak from dM/dT of the data shown in Fig. 5.1 and the temperature position of the peak in χ_{ac} from the data shown in Fig. 5.2 is given in Fig. 5.3. It can be seen that T_c decreases monotonically with x. The values extracted using the first dM/dT method usually gave a slightly higher value than the χ_{ac} values although the difference is small and the trend is very clear. Later in the chapter the exchange energy J will be estimated using these values of T_c and the larger values provide by the first method are used to give a maximal value for J.
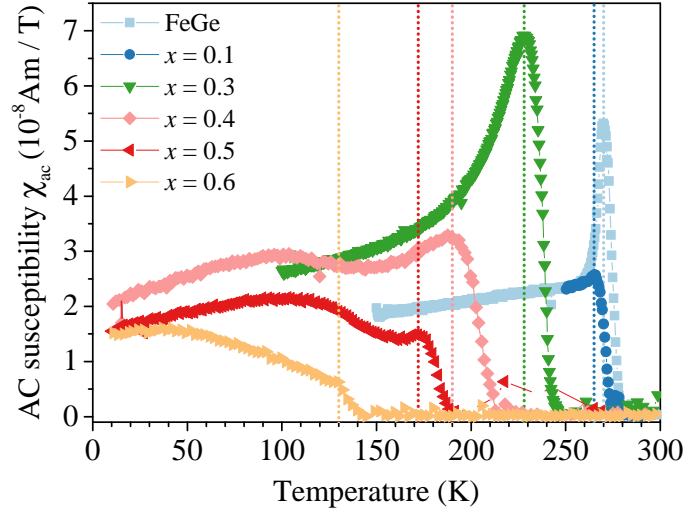
Figure 5.2: AC susceptibility χ_{ac} for $Fe_{1-x}Co_xGe$ with static DC field applied in-plane at 2 mT and AC field at 1 mT with frequency 23 Hz. Points with significant error have been removed for clarity. Dotted lines with corresponding colour show T_c for each composition determined from peak in χ_{ac}.
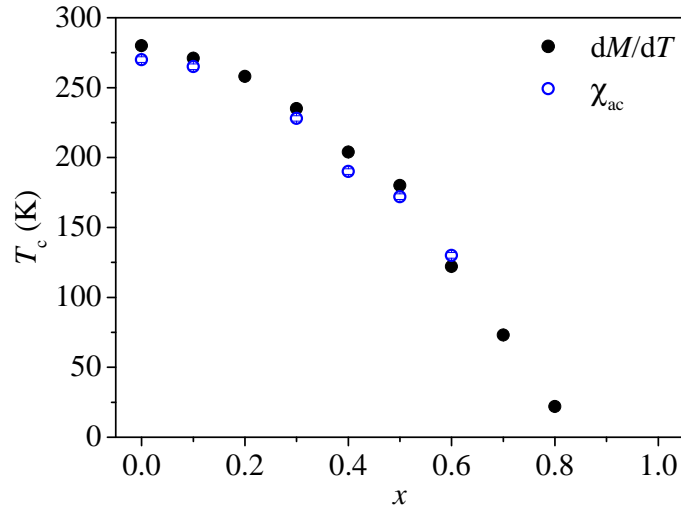
Figure 5.3: Magnetic ordering temperature T_c for $Fe_{1-x}Co_xGe$ as a function of composition x determined using minimum in $\chi_{dc} = dM/dT$ (filled circles) and peak in χ_{ac} (open circles).

5.2.2 Magnetisation

To determine the saturation magnetisation M_s for each film, four quadrant hysteresis loop measurements (comprising of both positive and negative applied field) $M(H)$ were taken at 5 K with the applied field IP up to 6 T to ensure full saturation. The results are shown in Fig. 5.4 along with the values taken using PNR described later in this chapter. For FeGe a magnetisation of (360 ± 10) kA/m was found which corresponds to a moment per Fe atom of (0.982 ± 0.007) μ_B. This agrees well with previous measurements of 1 μ_B per Fe atom found in bulk FeGe [18] and also similar values found in other thin films [41, 53]. As the composition is altered with increasing x the magnetisation is found to decrease. The values provided by the PNR (from the fits presented in Sect. 5.3.3) compare well to within error with the values found using SQUID magnetometry.
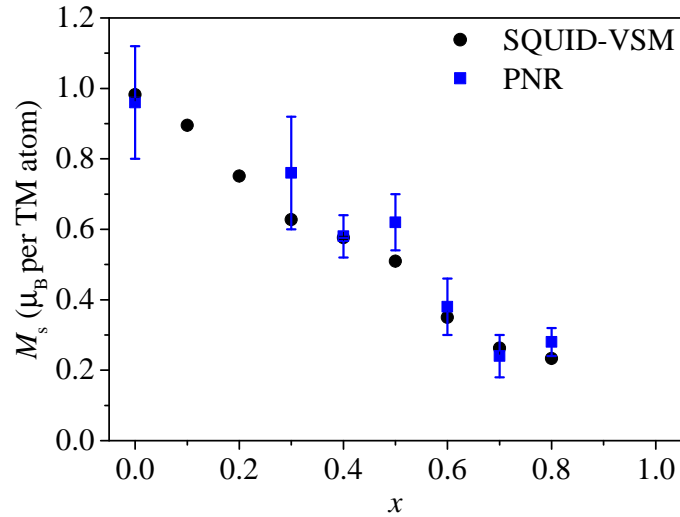
Figure 5.4: Saturation magnetisation M_s for $Fe_{1-x}Co_xGe$ as function of composition x measured using SQUID-VSM (circles) and PNR (squares).

5.2.3 Anisotropy in $Fe_{1-x}Co_xGe$ films

B20 TM silicide and germanide structure films grown on Si substrate have been shown to have additional uniaxial anisotropy that acts to induce an easy-plane anisotropy in these films [40, 44]. To investigate the influence in $Fe_{1-x}Co_xGe$ films we have measured the samples in both IP and OOP orientations. The hysteresis loop measurements $M(H)$ were made to determine the magnetisation for all of the $Fe_{1-x}Co_xGe$ samples and the IP (filled circles) and OOP (open circles) results for each film, at 5 K unless otherwise stated, are shown in Fig. 5.6. It can be seen that each film exhibits an easy-plane anisotropy. The hysteresis seen in the IP orientation shows complex behaviour which will be discussed below in Sect. 5.3, whereas the OOP measurement shows little to no hysteresis.

The OOP data for each composition show a linear increase of magnetisation until a critical field H_{c2} is reached at which point it saturates sharply. For this system and other helimagnets, H_{c2} is the field at which the magnetic structure is saturated from a conical phase into a field polarised state and the values for H_{c2} are given in Fig. 5.5. The saturation point was determined from the position of the minimum in dM/dH and in Fig. 5.5 H_{c2} is seen to decrease with increasing x which corresponds to the decreasing magnetisation seen in Fig. 5.4.
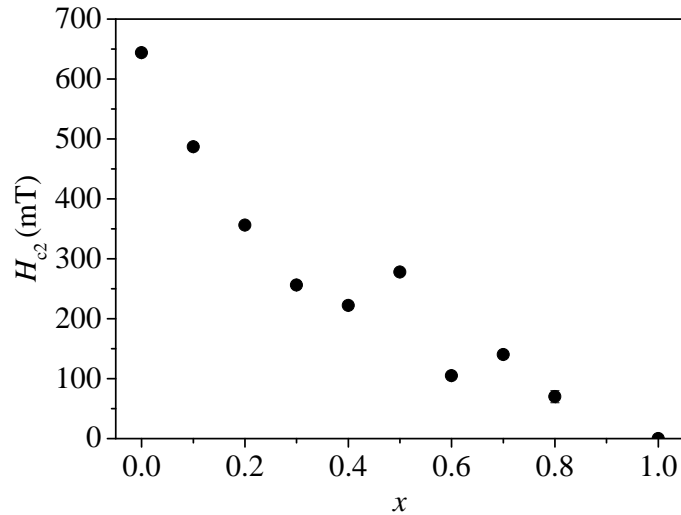
Figure 5.5: Critical field H_{c2} for $Fe_{1-x}Co_xGe$ with applied field out-of-plane. Values taken from saturation point at minimum in dM/dH from data in Fig. 5.6.
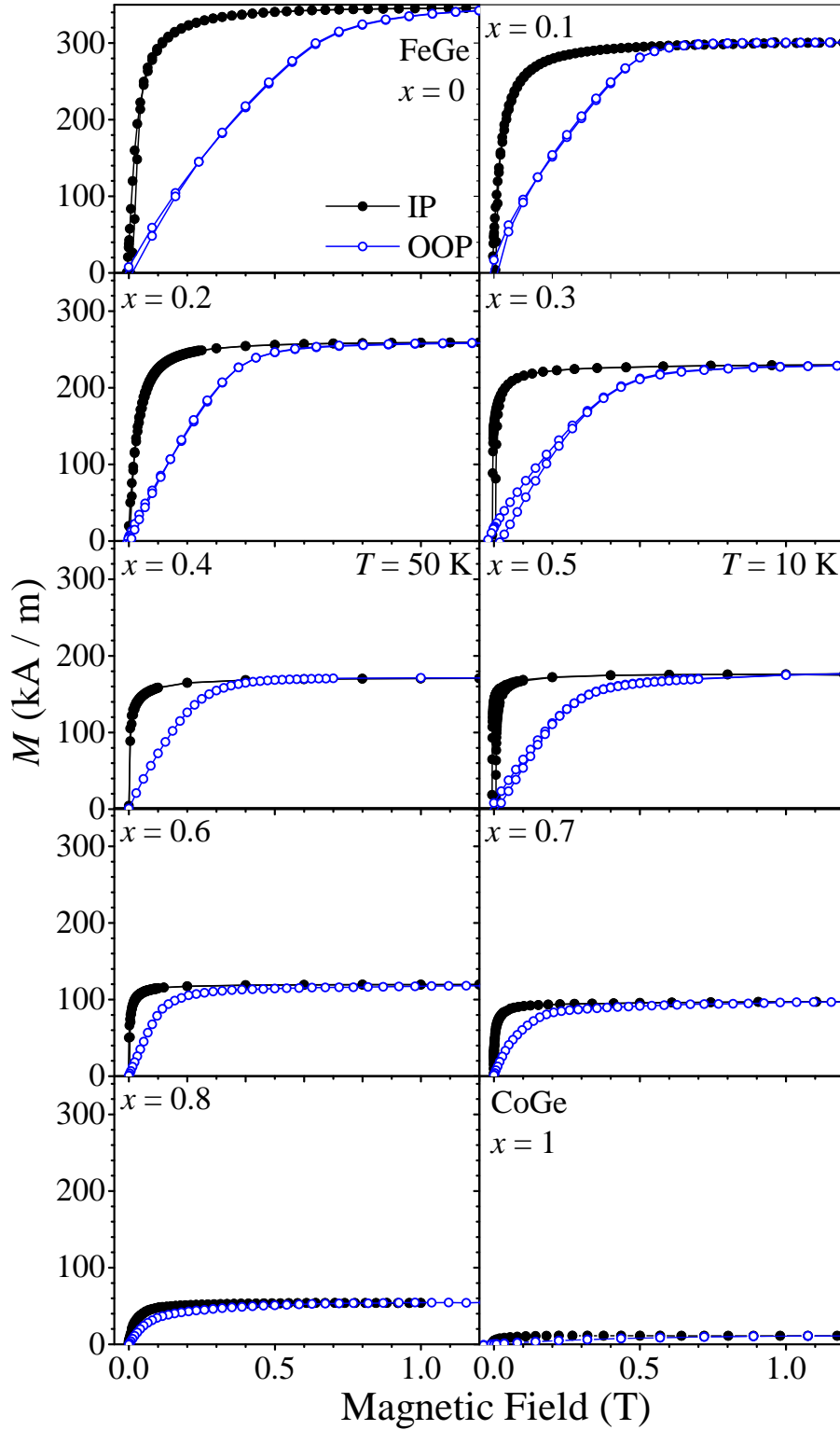
Figure 5.6: First quadrant $M(H)$ loops measured at 5 K, unless otherwise stated, for Fe$_{1-x}$Co$_x$Ge with x = 0 to 1. Each panel shows the in-plane (filled circles) and out-of-plane (open circles) measurement. Only a paramagnetic signal is seen from CoGe.

5.3   Helical magnetic structure in Fe$_{1-x}$Co$_x$Ge

To investigate a possible helical magnetic structure, low-field $M(H)$ measurements of Fe$_{1-x}$Co$_x$Ge films with a field applied in-plane were examined to identify any possible evidence.

5.3.1   Magnetic helicoids in FeGe

Figure 5.7 shows $M(H)$ measurements taken with an applied field in-plane at 5 K on FeGe films with varying thickness t_{film}. The measurements show that the behaviour of the IP magnetisation is greatly influenced by the film thickness. By assuming a helical magnetic structure with the helix axis normal to the plane this can be explained by comparing the helix wavelength to the film thickness. Looking at the samples with t_{film} < 70 nm, as both of these films are thinner than the expected helix wavelength, the magnetic structure within these films is anticipated to be almost ferromagnetic and so no exaggerated features are expected [39], from the data this is the case. In Fig. 5.9 the results for the 67.8 nm FeGe film are shown. Here the shape changes dramatically and a step-like feature can be seen. Here the film is now of the order of the helix wavelength, and so as the applied field strength is increased the helix is deformed and becomes a helicoid [52]. The step feature is produced as a 'node' of the helix is pushed out of the film [44]. On further increasing the thickness in Fig. 5.7 the shape continues to change and the sharpness and number of steps increases. As these films are now thicker than the expected wavelength there is now more than one period of the helix present. At t_{film} = 186 nm clear steps in the magnetisation can be seen that show little hysteresis. With this concept in mind this further reinforces the picture that with varying the field the helix is unwound and on reversing the field direction the small hysteresis shows the state is easily recovered. Finally at t_{film} = 280 nm ($\sim 4\lambda_{\text{h}}$) the shape no longer shows this structure. Since this film is now thick and due to the small range of applied field required to deform the helix, any unwinding of the helix or deformation may be obscured.

Another aspect to investigate is the remanent magnetisation M_{r}. The variation in M_{r} with changing film thickness is expected in the case of a helimagnetic thin film. Karhu *et al.* (Ref. [39]) showed that for such a film with the magnetic moments lying in plane and the helical propagation vector normal to that plane the remanent magnetisation will oscillate as function of film thickness with the remanence reaching a minimum value

61
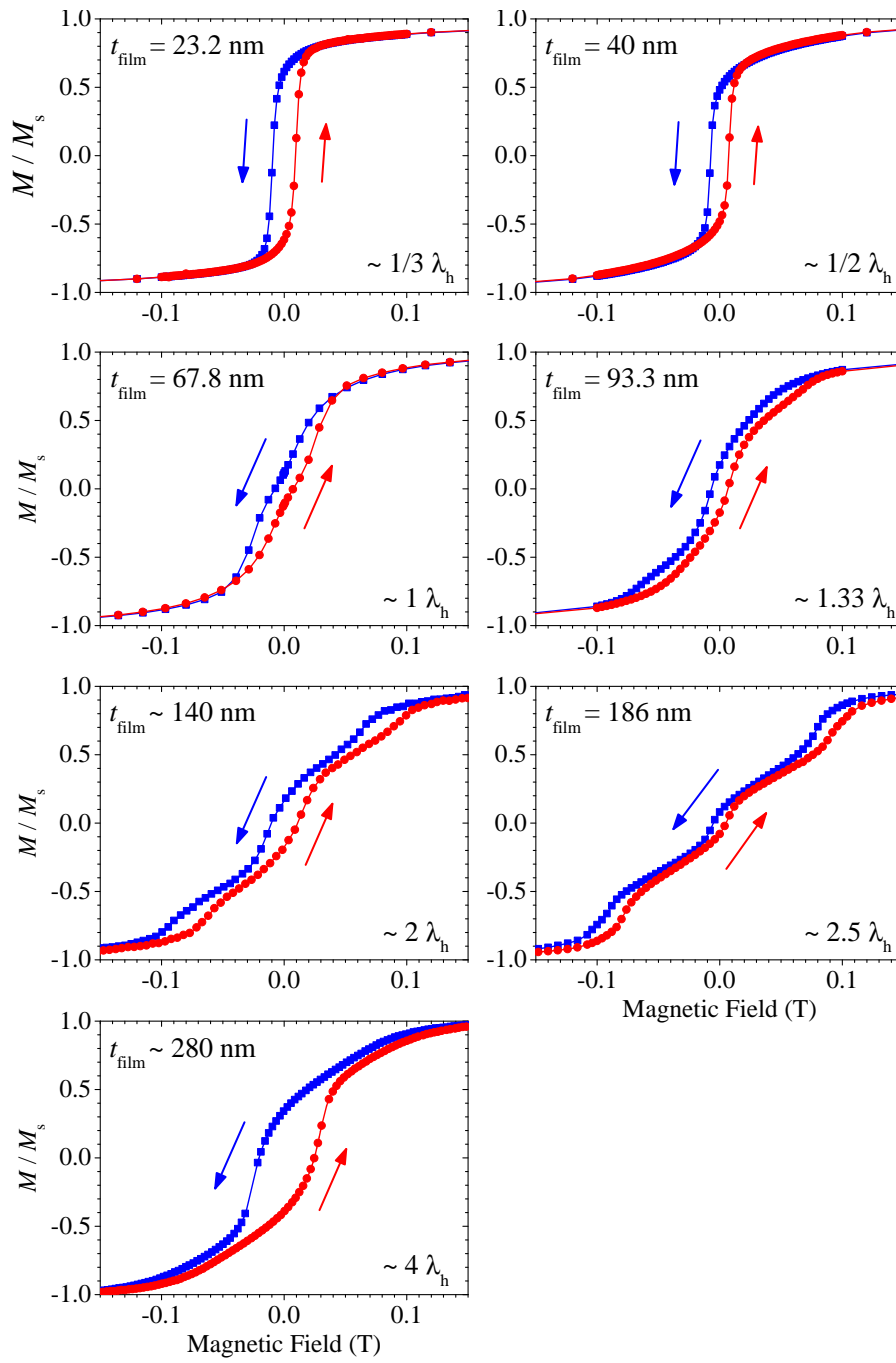
Figure 5.7: In-plane $M(H)$ hysteresis loops for FeGe with varying film thickness. Data has been normalised to highlight low field behaviour.
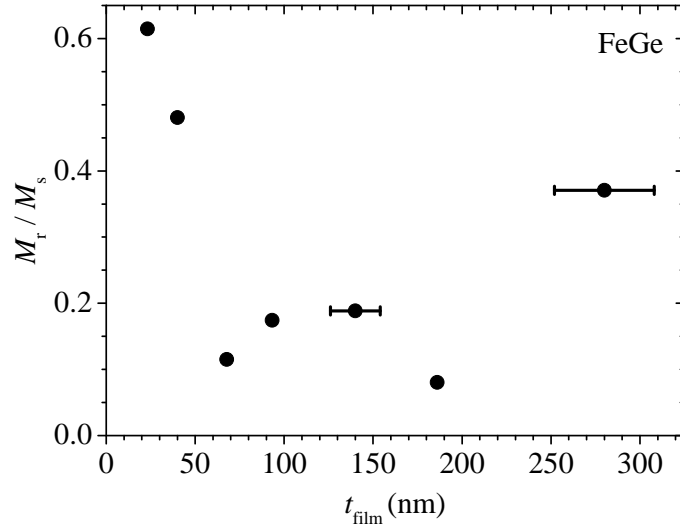
Figure 5.8: Remanent magnetisation as a function of film thickness for FeGe films.

at film thicknesses of integer periods of the helix wavelength and a maximum value at thicknesses of 1/2 integer periods. Figure 5.8 shows the remanent values obtained from the FeGe films. The large error for t_{film} = 140 nm and 280 nm is due to the films thickness being too thick to measure using XRR and so the estimated deposited thickness is used, which has an error of $\sim$ 10 % for films over 100 nm (the t_{film} = 186 nm film was measured using PNR and the thickness was accurately determined). The inital data 0 nm $< t_{film} <$ 100 nm show a decreasing remanence which has a minimum at t_{film} = 67.2 nm and then increases again. For $t_{film} >$ 100 nm the trend is not so clear, here we see another minimum at t_{film} = 186 nm, which is close to $\sim$ 3 λ_h (210 nm), but there is no clear minimum at t_{film} = 140 nm. This data hints at the possibility of a helical structure due to the oscillations in M_r, but unfortunately without more film thicknesses it is not possible to accurately determine the helix wavelength using this method.

5.3.2 Magnetic helicoids in Fe$_{1-x}$Co$_x$Ge

In Fe$_{1-x}$Co$_x$Ge films the helical magnetic structure shown for FeGe in Sect. 5.3.1 is expected to be present due to the continued B20 structure and the helimagnetic phase has been observed in bulk Fe$_{1-x}$Co$_x$Ge samples [29]. However the effect that can be observed in these $M(H)$ measurements depends on ratio of the helix wavelength and the thickness of the film. For our Fe$_{1-x}$Co$_x$Ge samples we have kept the thickness of the films relatively constant ($\sim$ 70 nm) and so we expect to see a change in magnetic behaviour due to a reduced amount of the helix structure being contained in the film, rather than from multiple periods of the spin helix as seen in the FeGe before (see Fig. 5.7). The IP $M(H)$ data measured for Fe$_{1-x}$Co$_x$Ge at 5 K are shown in Fig. 5.9, with the exceptions of $x = 0.5$ and 0.8 at 10 K due to measurement constraints, however this is far below T_c for these values of x and still comparable to the other samples. Here the shape of the hysteresis varies significantly with composition.

If we again assume a helical magnetic structure, the explanation for the change in response is given as follows: with varying x the λ_h is expected to vary as seen in other B20 compounds, so if each film is the same thickness $\sim$ 70 nm, and if the λ_h varies significantly, the magnetic structure of the film will vary between a helical and a collinear ferromagnetic (FM) state. As the wavelength is given by the ratio of $\sim J/D$, if the DMI goes to 0 a FM state will be reached. The measurements shown in Fig. 5.9 reflect this to a degree. Starting with FeGe ($x = 0$) the $M(H)$ measurement is explained as above, on increasing x the $M(H)$ loop starts to lose the step features. On further increase of x the $M(H)$ loop starts to become more square and at $x = 0.5$ an almost completely square loop is seen which would signify a collinear FM state. As we increase x beyond 0.5 the $M(H)$ shape of the lower x values is recovered. The measure of squareness, M_r/M_s, is given for Fe$_{1-x}$Co$_x$Ge in Fig. 5.10. Here the trend is clearer and the peak is seen at $x = 0.5$.
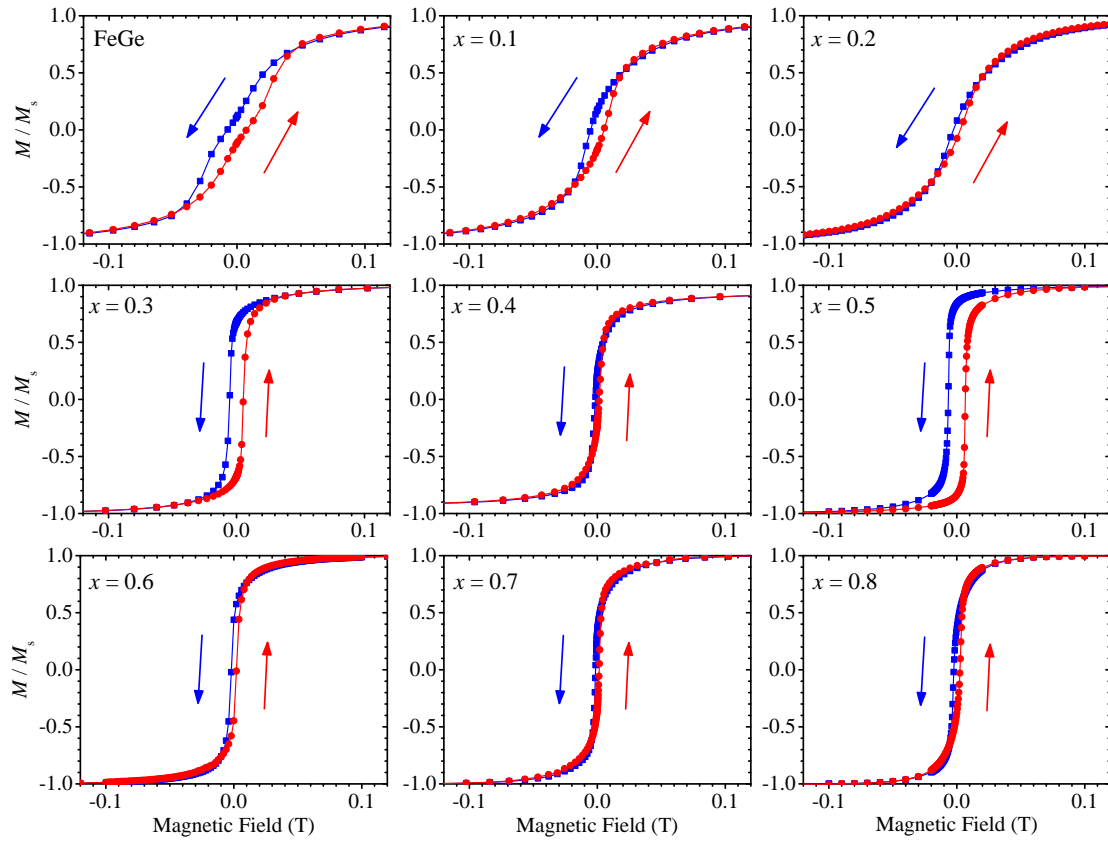
Figure 5.9: In-plane $M(H)$ hysteresis loops for $Fe_{1-x}Co_xGe$ films measured at 5 K, (10 K for $x =$0.5, 0.8). Note the magnetisation scale decreases with each row and the applied field range is reduced for the bottom row.
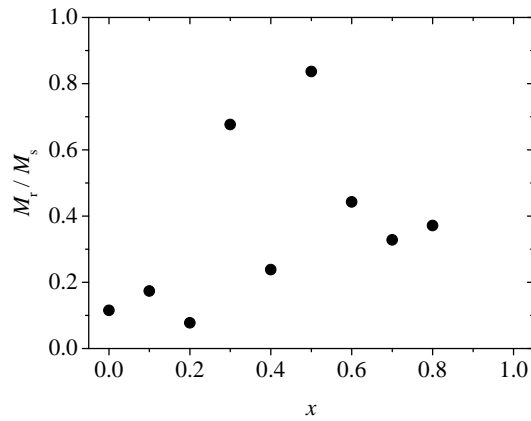
Figure 5.10: Squareness of $M(H)$ data showing ratio of M_r/M_s as for $Fe_{1-x}Co_xGe$ as a function of x.

5.3.3 Helical magnetic structure observed using polarised neutron reflectivity

To directly observe the helical magnetic structure in these films the method presented by Monchesky *et al.* [40, 52, 55] using PNR to fit a helicoid to the magnetic depth profile was used. The magnetic scattering length density (SLD) depth profile provided by PNR is the sample averaged moment aligned in the field direction as function of thickness. In these $Fe_{1-x}Co_xGe$ films there are grains of both chiralities, similar to the MnSi epitaxial films [39, 40], which produces both left- and right-handed helix structures. This leads to cancellation of the moments not parallel to the applied field and thus the measured depth profile is a 2D representation of the helix structure. Once the applied field is strong enough this profile is then distorted into a helicoid [52] and the magnetisation profile of the sample using this helicoid model is given by:

$$M(x) = M_1 \sin\left(\frac{2\pi x}{\lambda_h} + \phi\right) + M_2 \cos^2\left(\frac{2\pi x}{\lambda_h} + \phi\right), \tag{5.1}$$

where M is the magnetisation, M_1 and M_2 are fitting parameters, x is the depth in the film, λ_h is the helical wavelength and ϕ is a fitting parameter allowing adjustment of the phase of the helicoid. This profile was used in conjunction with the GenX [58] software to fit the data. The $Fe_{1-x}Co_xGe$ samples were field cooled in a small field of 5 mT to 50 K for $0 \leq x \leq 0.6$ and cooled to 5 K for $x = 0.7$ and 0.8. For $x = 0.7$ and 0.8, the higher Co concentration samples, the magnetic moment is smaller and T_c is lower, so a reduced temperature was used. Once cooled, the field was reduced to 1 mT (the smallest possible before de-polarisation of the neutrons) to reduce distortion of the magnetic profile and a measurement was made. The results of the measurements are shown in Figure 5.11 and the magnetisation extracted from these fits are given above in Fig. 5.4. The spin asymmetry and resulting fits from the reflectometry are shown in the left panels (a-g) and the resulting magnetic depth profiles are shown on the right in (h-n). a) and h) show a second fit to the data presented in Ref [44]. For $x = 0.3$ to 0.6 (i-l) each magnetic profile showed a nearly uniform profile with a curve about the centre due to the helical structure. For $x = 0.7$ and 0.8 a helicoid could be fitted and a wavelength less than that in FeGe was observed.
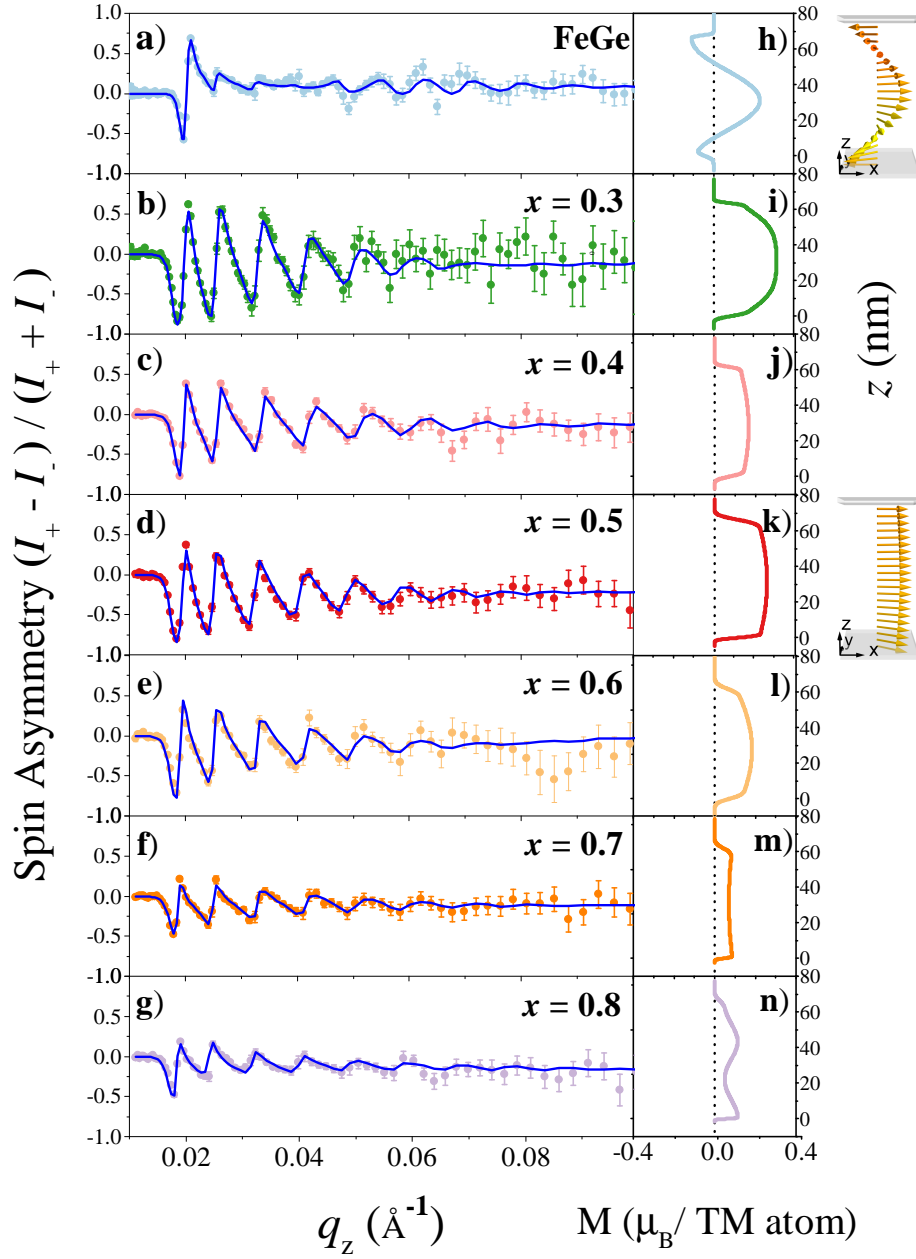
Figure 5.11: PNR results showing spin asymmetry and magnetic depth profiles for $Fe_{1-x}Co_xGe$ films with x from 0 to 0.8 at 50 K (a-e) and 5 K (f,g) with a 1 mT field applied in-plane. a-g) Spin asymmetry (circles) and fits (lines). h-n) Magnetic depth profiles extracted from fits to the reflectivity at each composition. a,h) for FeGe, the helical structure can be clearly seen in the magnetic profile. On increasing the Co content for i-k) the profile becomes flatter and a uniform magnetisation is seen at k) $Fe_{0.5}Co_{0.5}Ge$. Upon further increase of Co in m-n) the initial helical shape is recovered. Diagrams show 3D helix structure in h) FeGe and uniformly magnetised state in k) $Fe_{0.5}Co_{0.5}Ge$.
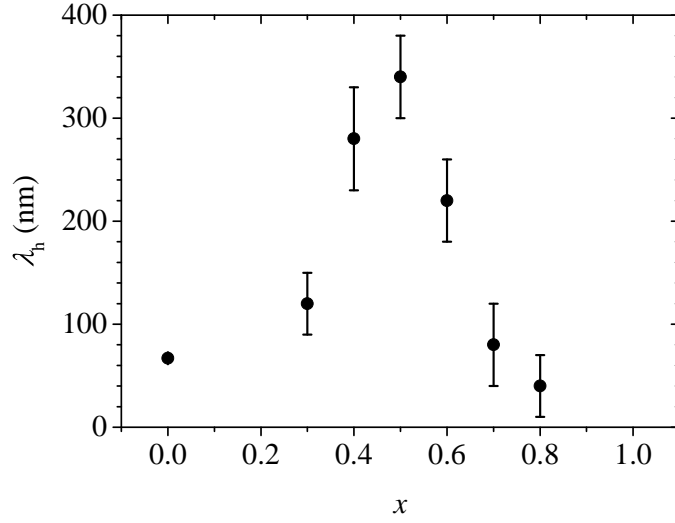
Figure 5.12: Extracted helix wavelength λ_h from PNR data for $Fe_{1-x}Co_xGe$ films.

From these fits the helix wavelength could be measured and the extracted values for each film are shown in Figure 5.12. The resulting helix wavelength is found to increase with x up to a turning point at $x_c = 0.5$ where the magnetic SLD profile is almost flat indicating a uniform magnetisation profile, on further increasing x the curvature is regained and a the wavelength is found to decrease up to $x = 0.8$. This behaviour has been seen before in bulk $Fe_{1-x}Co_xGe$ and $Mn_{1-x}Fe_xGe$ and has been explained as the magnetic state transitioning from a helix structure to a collinear ferromagnetic structure as the DMI changes sign and passes through zero [29, 30]. The values shown for $0.3 \leq x \leq 0.8$ have a reasonably large error which is associated with the method in which they were extracted. Due to the films of these x being of a thickness less than the wavelength, the value measured could be seen as the lower boundary in which decreasing the value any more affected the curvature of the magnetic SLD profile such that it no longer fitted the experimental data. In the case of $x = 0.5$ the value shown for λ_h is the longest possible as the magnetisation profile was essentially uniform indicating a collinear FM state. The values measured here are also shown in Fig. 6.23 for comparison with other B20 compounds.

5.3.4   Exchange energy and DMI estimation in $Fe_{1-x}Co_xGe$

The helix wavelength is defined by the ratio of the exchange energy J and the DMI constant D given by $\lambda_h = 2\pi J/D$, by knowing the helix wavelength and the exchange energy the DMI constant can be found. In previous work two approaches have been used, the work by Maleyev [72] showed that using the critical field H_{c2} between the conical and ferromagnetic phase as a measure for the energy between the helical and ferromagnetic state, J could be found using $g\mu_B H_{c2} \approx A k_s^2$, where A is the exchange stiffness and k_s is the helix wavevector $(2\pi/\lambda_h)$. This method has been used to describe MnSi [26] well, however when applied to intermediate B20 materials such as $Fe_{1-x}Co_xGe$, the model diverges around x_c and is not applicable [73].

Another approach is the work by Shibata *et al.* [30] where they showed that by using an approximation of the exchange energy $J \approx k_B T_c$ with the experimental values of λ_h, a value for D can be estimated using the same ratio. Using this method, the values for J and D estimated for our $Fe_{1-x}Co_xGe$ films with the λ_h values obtained from our PNR study are shown in Fig. 5.13. As $J \propto T_c$ a smooth decrease in J with increasing x is seen which is consistent with the decreasing T_c and M_s as we move across the group. For D, the values calculated using this method show a decrease as $x \to x_c$ and an increase after the inflection point due to the inverse relationship with λ_h. The values beyond x_c are set to be negative as it is assumed there is a change in sign as has been shown in previous B20 materials [30, 31].
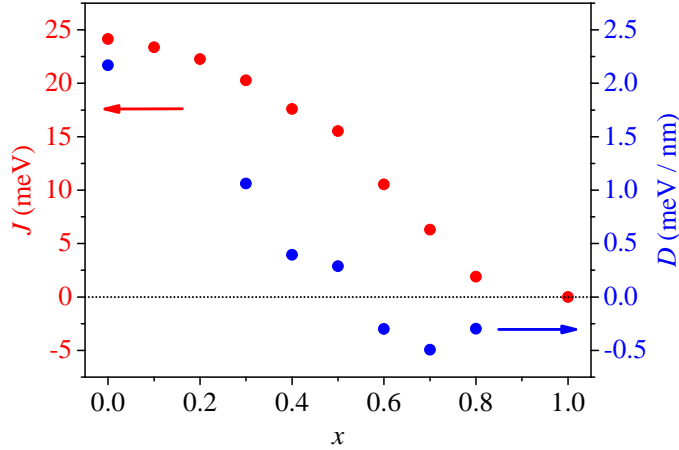
Figure 5.13: Exchange energy J and DMI constant D for $Fe_{1-x}Co_xGe$ films. Values estimated using λ_h measured from PNR.

5.4 Summary

In this chapter the magnetic properties of $Fe_{1-x}Co_xGe$ have been explored and a helical magnetic structure has been observed within these films. The magnetometry has shown the general trend of reduced magnetic interaction as the Co content is increased as FeGe $\rightarrow$ CoGe.

The helical magnetic structure is consistent with what was expected for a B20 system and current literature. The helix wavelength is found to increase as $x \rightarrow x_c$. The helical magnetic structure of $Fe_{1-x}Co_xGe$ has been measured previously in bulk samples by Grigoriev *et al.* and the PNR values obtained here compare well to those presented by them in Ref. [29]. We take the inflection point at which the helix wavelength diverges, $Fe_{0.5}Co_{0.5}Ge$, to be x_c whereas it was seen previously by Grigoriev *et al.* for $Fe_{0.4}Co_{0.6}Ge$. Our measurements were taken with the same x steps of 0.1 as in Ref. [29], however due to our method of assuming the helix form by measuring λ_h from a helicoid model we can only infer this is the x_c from the lack of curvature in the magnetisation profile shown in Fig. 5.11 k), however Grigoriev *et al.* used small angle neutron scattering to measure the helix wavevector k_s directly from diffraction. As such we cannot say for certain that $x_c = 0.5$ and it may lie in between $0.4 \leq x \leq 0.6$ due to the choice of our compositions.

By exploring the intermediate compositions of $Fe_{1-x}Co_xGe$ we were able to investigate the magnetic transition from helimagnet to FM to helimagnet of opposite chirality and in the next chapter, in conjunction with the transport measurements, the effect of the helical magnetic structure on the transport properties will be examined.

CHAPTER 6

Transport properties in B20 $Fe_{1-x}Co_xGe$ epitaxial films

6.1   Introduction

The magnetotransport measurements on FeGe and $Fe_{1-x}Co_xGe$ films on Si substrates are presented in this chapter. Magnetotransport measurements have been performed previously on bulk B20 materials [47, 74, 75] and epitaxial films [52, 76] including FeGe [41–43]. However $Fe_{1-x}Co_xGe$ has only been explored in a small composition range in bulk polycrystalline samples [77] previously and not in epitaxial films. At first we start with resistivity measurements as a function of temperature to characterise the general behaviour and then move onto the magnetotransport. The longitudinal magnetoresistance is first explored before the Hall effect is examined. This is broken into its constituent components, the ordinary Hall effect, the anomalous Hall effect and the topological Hall effect and each is looked at individually. The measurements presented here were taken using Hall bar devices fabricated from the same samples used in the previous chapters with the exception of $Fe_{0.7}Co_{0.3}Ge$. This was due to insufficient material left to be processed into a Hall bar from the previous measurements, and so a second sample for $Fe_{0.7}Co_{0.3}Ge$ as detailed in Sect. 4.5 was used.

6.2   Resistivity

The measured zero-field resistivity as a function of temperature $\rho_{xx}(T)$ for $0 \leq x \leq 1$ is shown in Fig. 6.1. The values shown here are measured from 20 μm width Hall bars at individual temperature steps with the exception of $x = 1$, where the measurement was taken using a sheet resistivity measurement with sweeping temperature. The parent materials FeGe and CoGe both show decreasing resistivity as the sample is cooled indicating metallic behaviour, consistent with previous measurements [42, 78]. The FeGe shows a residual resistivity of ~ 50 $\mu\Omega$ cm and a residual resistivity ratio (RRR) of ~ 7 which is consistent with other epitaxial films [41] and indicates a high film quality. For CoGe a residual resistivity of ~ 140 $\mu\Omega$ cm and RRR of 1.3 is seen. Although lower than FeGe, this RRR is comparable to measurements in bulk polycrystalline samples where a RRR of 1.8 is observed in Ref. [33] and ~ 2 in Ref. [78] which shows films resistivity scaling is close to the bulk crystal value and is of good quality. For intermediate compositions, $0.1 \leq x \leq 0.8$, all samples deviate from this simple behaviour and show a broad peak ρ_{peak} in the resistivity below their respective T_c. In Fig. 6.1 the T_c for each composition is shown by a vertical line and ρ_{peak} occurs just below T_c, the temperature when ρ_{peak}

occurs shows a dependence on T_c and decreases with increasing x.

To clarify this feature a comparison between the measured $\rho_{xx}(T)$ and M as a function of temperature is shown for a selected sample, $x = 0.5$, in Fig. 6.2 a). The first derivatives for each data set dM/dT, $d\rho/dT$ and the second derivative for $\rho_{xx}(T)$, $d^2\rho/dT^2$ are shown in Fig. 6.2 b) and c) respectively. In b) the minimum in dM/dT shows a clear correspondence with the minimum in $d\rho/dT$ indicating the onset of ρ_{peak} occurs as the film passes through a magnetic transition. In c) the minimum of $d^2\rho/dT^2$ is shown, identifying the position of ρ_{peak}. Two dashed lines are shown across Fig. 6.2 which show the position of ρ_{peak} and T_c (taken from the minimum in dM/dT, as shown in Sect. 5.2.1).
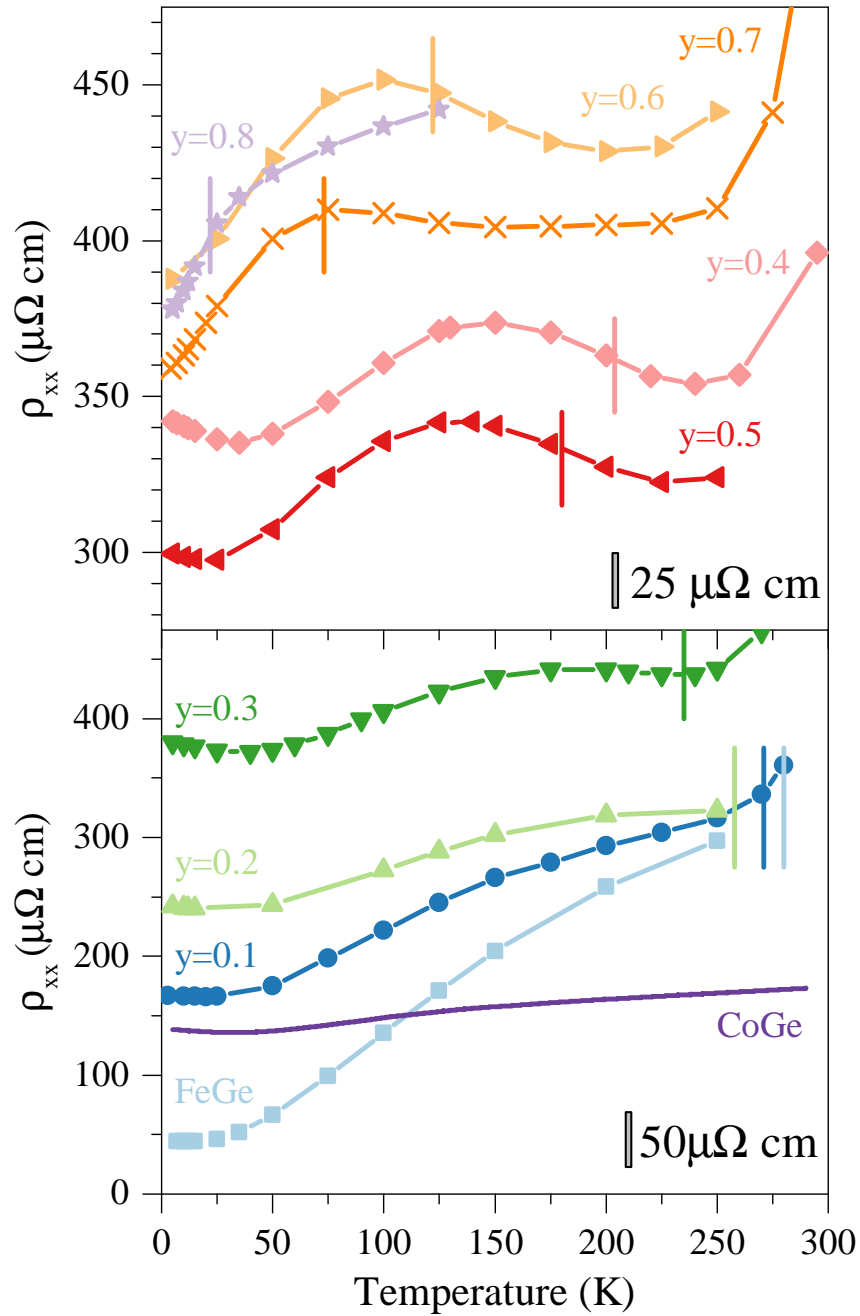
Figure 6.1: Resistivity as a function of temperature $\rho_{xx}(T)$ at zero magnetic field for all concentrations of x. The data are separated into two panels to highlight the details in $\rho_{xx}(T)$. The bottom panel shows $0 \leq x \leq 0.3$ and $x = 1$, whereas the top panel shows $0.4 \leq x \leq 0.8$. Vertical lines show T_c for the respective concentration x. The data points for $0 \leq x \leq 0.8$ show measurements taken at fixed temperature and the lines are a guide for the eye. The data shown for $x = 1$ was taken using a sweeping temperature. Note the change in scale between panels indicated by the marker in the bottom right corner.
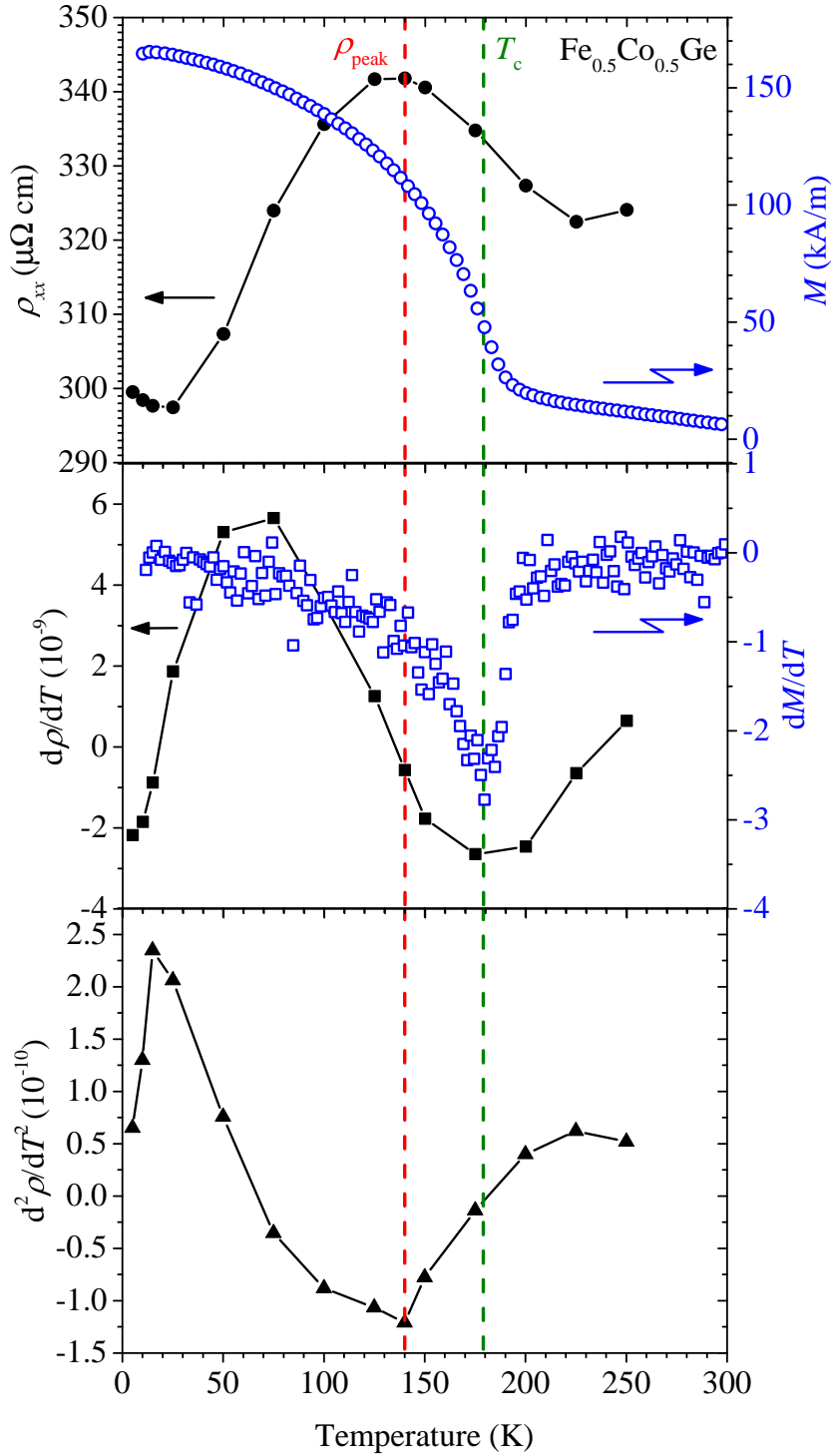
Figure 6.2: a) Temperature dependent resistivity $\rho_{xx}(T)$ and magnetisation M (with IP applied field of 10 mT) for $Fe_{0.5}Co_{0.5}Ge$. First derivative dM/dT, $d\rho/dT$ and second derivative $d^2\rho/dT^2$ shown in b) and c) respectively. Dashed lines correspond to ρ_{peak} position and T_c, the extremum in dM/dT.

To attempt to identify the origin of the ρ_{peak} observed in Fig. 6.1 films of disordered amorphous $Fe_{1-x}Co_xGe$ were grown (~ 70 nm) as a control and the resistivity measured from a sheet film of each compositions are shown in Fig. 6.3. For $0 \leq x \leq 0.7$ the resistivity shows a semiconductor like behaviour with an increasing resistivity with decreasing temperature and a sharp up-turn in resistivity below ~ 25 K. In $x = 1$ a similar behaviour to $0 \leq x \leq 0.7$ is seen for temperatures above ~ 100 K, however below this temperature, the opposite behaviour is seen as the resistivity decreases with lowering temperature. The lack of features near T_c, as seen in Fig. 6.1, confirms the resistivity peak is associated with the B20 structure.

The onset of this feature is clearly linked to the magnetic ordering in these films, however behaviour like this is not observed in the any of the neighbouring B20 compounds such as $Mn_{1-x}Fe_xGe$ or $Fe_{1-x}Co_xSi$. In $Mn_{1-x}Fe_xGe$ bulk polycrystalline samples $\rho_{xx}(T)$ is found to have metallic behaviour similar to FeGe which is consistent across the range to MnGe [46]. $Fe_{1-x}Co_xSi$ undergoes a semiconductor to metal transition with increasing x, however no sign of a resistivity peak feature is seen in the metallic region around T_c [79]. $\rho_{xx}(T)$ behaviour has been measured previously in $Fe_{1-x}Co_xGe$ for a small range of x towards the Co-rich side ($0.7 \leq x \leq 1$). All of the samples show a similar behaviour to the CoGe measured here, with the exception of $x = 0.7$ where a small peak near ~ 75 K is seen as we see in our data.

Anomalies in the resistivity as T_c is approached are expected in ferromagnetic materials and is caused by additional scattering due to spin fluctuations. Fisher and Langer [80] showed that in the case of short-range interactions $d\rho_{xx}/dT$ should vary as the magnetic specific heat. This is seen very clearly for MnSi [62, 81], however for FeGe a similar curve is seen for the magnetic specific heat, but the shape of $d\rho_{xx}/dT$ is different. Another theoretical model by Suezaki and Mori [82] examines the effects of long-range interactions and has been used to describe the periodic magnetic structures found in rare-earth materials and predicts a peak in the resistivity just below T_c which may be applicable to the situation here.

Another case of similar behaviour has been observed in $HoMn_{12-x}Fe_x$ alloys which order antiferromagnetically and a pronounced peak in resistivity can be seen as the material passes through its Néel temperature T_n. [83]. The feature is explained as spin disorder scattering caused by random substitution of Mn by Fe atoms. Although a different system, both share non-collinear magnetic ordering and the effect is found to
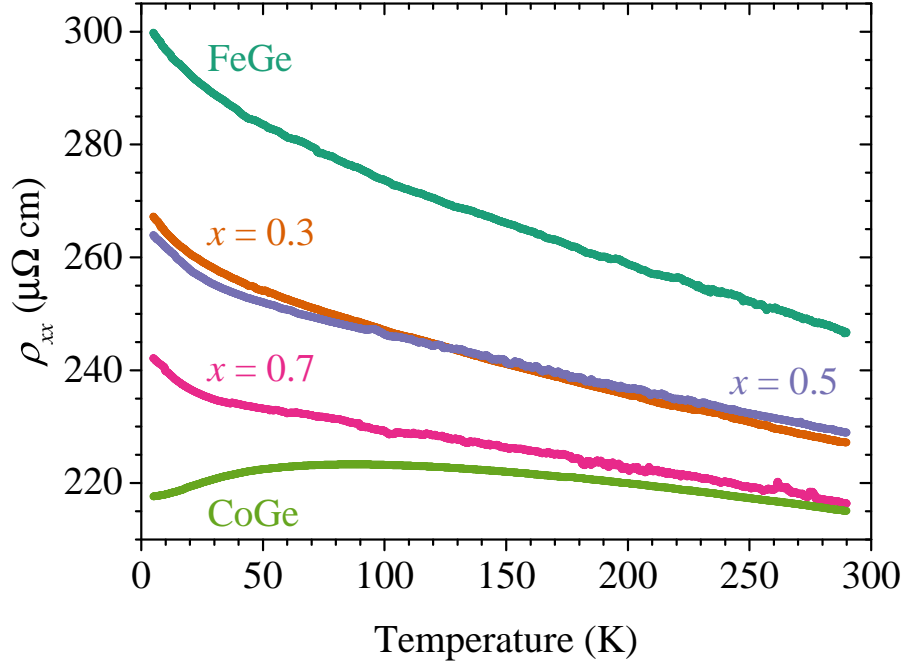
Figure 6.3: Resistivity as a function of temperature for disordered amorphous $Fe_{1-x}Co_xGe$ films.

strongest at the middle compositions, this could offer a possible avenue of research.

Although the origin of ρ_{peak} remains unknown, we find the inflection points shown in $\rho_{xx}(T)$ identify different regions in the magnetoresistance and Hall effect resistivity scaling that will be discussed later in Sect. 6.4.3.

6.3 Magnetoresistance

Magnetoresistance (MR) is defined as "The dependence of the electrical resistance of a body on an external magnetic field". MR measurements were performed using Hall bar patterned devices of bar width 20 μm with an applied field perpendicular to the film plane. The samples were measured at temperatures from 5 K to room temperature and applied fields of ± 8 T. The results shown here were taken using a sweeping magnetic field with rate 0.25 T/min at fields <1 T and up to 2 T/min for fields >1 T with an applied DC current source of ± 100 μA using a current reversal method to average over 4 periods for each measurement. The MR $\Delta\rho_{xx}/\rho_{xx} = (\rho_{xx}(H) - \rho_{xx}(0))/\rho_{xx}(0)$ for each composition of $Fe_{1-x}Co_xGe$ at 5 K is shown in Fig. 6.4.
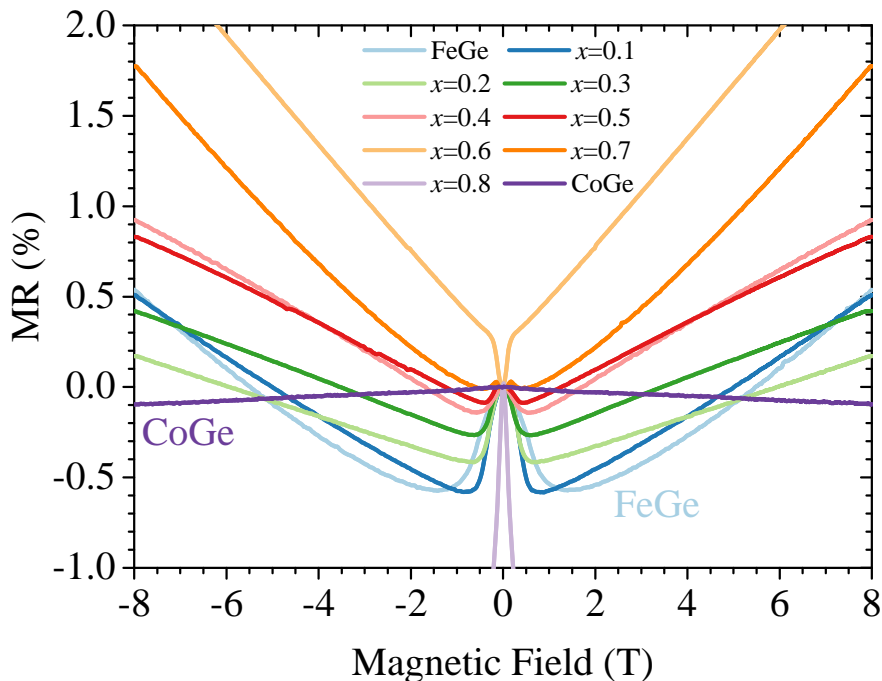
Figure 6.4: Magnetoresistance with field applied out-of-plane for ± 8 T for 20 μm Hall bars of $Fe_{1-x}Co_xGe$ for all concentrations of x at 5 K.

In this orientation, with the magnetic field applied out-of-plane, the applied field is parallel to the helix axis in $Fe_{1-x}Co_xGe$ films and increasing the field acts to distort the helix into a conical phase up to a critical field H_c where the magnetization becomes fully field-polarised [42]. In Fig. 6.4 the MR shown for FeGe shows an initial resistivity ρ_{cone} which decreases with applied field up to H_c at which point the magnetization becomes uniform and a background MR is seen. First we will discuss the background MR at high-fields (H > H_c) and then move onto the low-field MR (H < H_c) due to the change in helix structure.

For an overview the data for all compositions and temperatures are shown in Fig. 6.5 each temperature data set is offset for clarity.
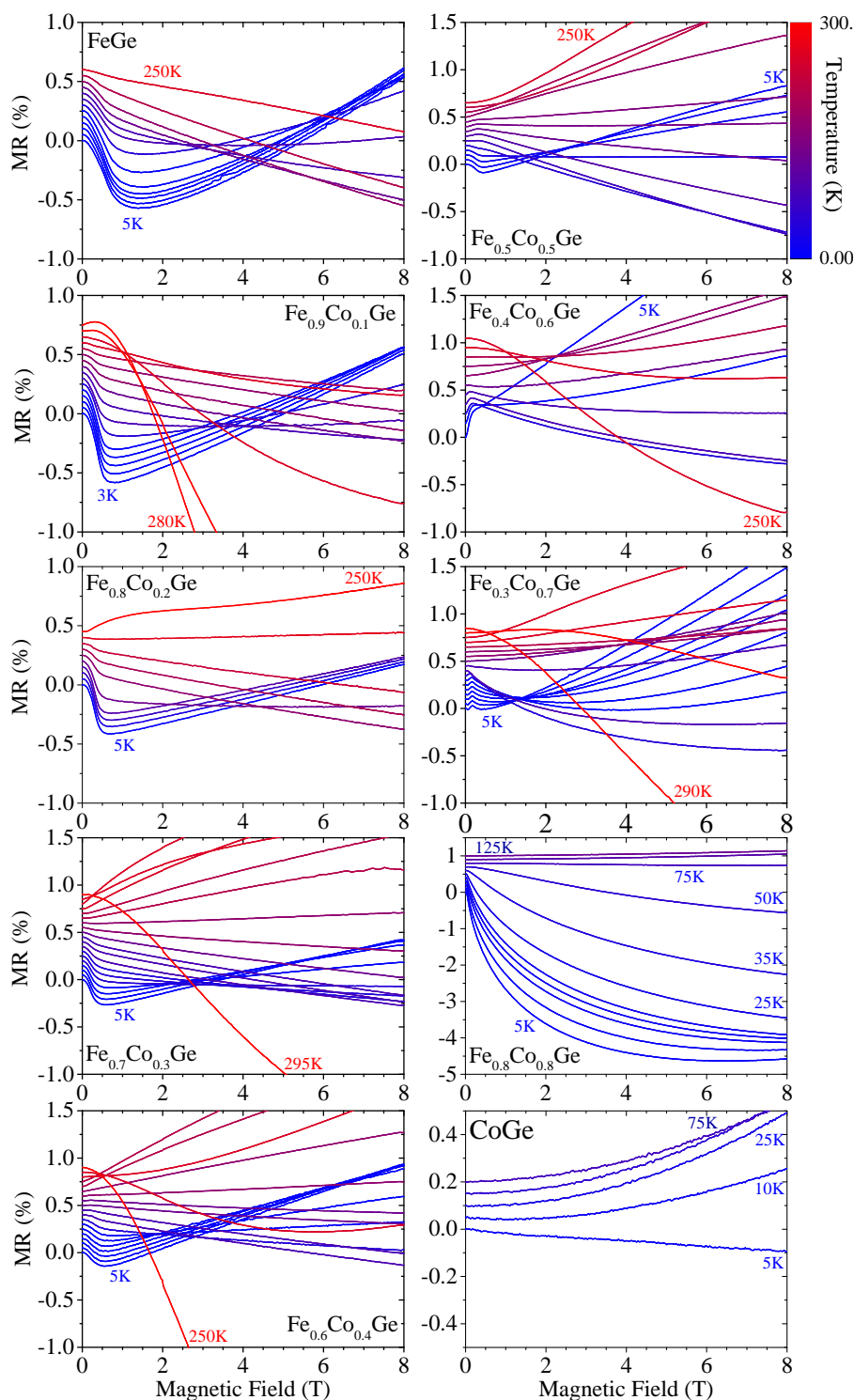
Figure 6.5: Magnetoresistance with field applied out-of-plane for ± 8 T at varying temperature from 5 K to 295 K for 20 μm width Hall bars of $Fe_{1-x}Co_xGe$ films with all concentrations of x. Note the data is offset by 0.05% for clarity. There is a significant change in scale for $Fe_{0.2}Co_{0.8}Ge$ and CoGe.

79

6.3.1 High-field (above H_c) background MR

For FeGe three temperature regimes for the MR with respect to the magnetic ordering temperature have been identified in Ref. [42]. For temperatures $T < 80$ K ($\sim T_c/4$) the orbital MR is expected to dominate at high fields and the resistivity is given by

$$\Delta\rho_{xx}(H) = \Delta\rho_{\text{cone}} + \rho_{xx}(0)(\mu_0 H)^q, \tag{6.1}$$

where $\rho_{xx}(0)$ is the resistivity at zero-field and q is the power law exponent. For temperatures $80 \leq T \leq 200$ K ($\sim 2T_c/3$) a linear negative MR is observed and is given by

$$\Delta\rho_{xx}(H) = \Delta\rho_{\text{cone}} - c_1\mu_0 H, \tag{6.2}$$

where c_1 is the fitting parameter for the negative MR due to electron-magnon scattering which is dominant at high-field. At temperatures approaching the ordering temperature, spin fluctuations become important and the MR for $T > 200$ K is given by

$$\Delta\rho_{xx}(H) = \Delta\rho_{\text{cone}} - b_1\ln[1 + (b_2\mu_0 H)^2], \tag{6.3}$$

where b_1, b_2 are fitting parameters for the semiempirical formula of Khosla and Fischer for local moment scattering [42]. The MR for each composition x at temperatures varying from 5 K to 290 K are shown in Fig. 6.5. The temperature dependent relations for FeGe shown in Eq. 6.1 to 6.3 have been applied to the Fe$_{1-x}$Co$_x$Ge data and are generally sufficient to explain the data, however there appear to be several discrepancies.

In the low-temperature regime <80 K ($T \sim T_c/4$) the relation shown in Eq. 6.1 is found to describe compositions $0 \leq x \leq 0.7$ with the high-field resistivity attributed to orbital MR. The MR for $x = 0.1$, 0.4 and 0.6 fitted using this equation is shown in Fig. 6.6 a). With increasing x, the background MR is found to change, as $x \rightarrow 0.6$ the MR dependence is found to become linear. The exponent q as a function of composition is shown in Fig. 6.6 b). For FeGe the orbital MR relation was found to have an exponent q < 2 which is expected experimentally and seen previously in Ref. [42]. With increasing x the q value extracted from the fits actually dips below 1 after Fe$_{0.8}$Co$_{0.2}$Ge, which can be seen in Fig. 6.6 for Fe$_{0.6}$Co$_{0.4}$Ge in the curvature of the data, and becomes l at Fe$_{0.4}$Co$_{0.6}$Ge. This linearity at high field has been observed in the Fe$_{1-x}$Co$_x$Si system previously and has been associated with its half-metallicity [76, 84, 85], also recent progress in theoretical studies have shown a prediction of a half-metallic state for Fe$_{0.4}$Co$_{0.6}$Ge [86]. On further increase of x to Fe$_{0.3}$Co$_{0.7}$Ge the linearity is lost and

background similar to FeGe is observed. For $Fe_{0.2}Co_{0.8}Ge$ the MR seen does not obey this rule.
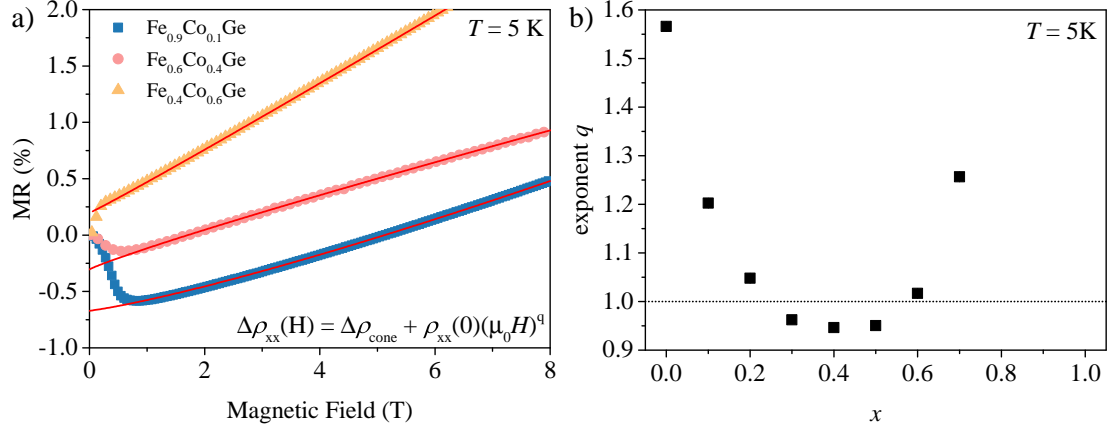
Figure 6.6: a) Magnetoresistance at $T < T_c/4$ for $Fe_{0.9}Co_{0.1}Ge$, $Fe_{0.6}Co_{0.4}Ge$ and $Fe_{0.4}Co_{0.6}Ge$ at 5 K fitted using Eq. 6.1. b) exponent q from fits in a) as a function of x.

At higher temperatures $T < T_c/2$ the negative linear MR seen in FeGe is observed up to $x = 0.5$. Figure 6.7 shows the data for $Fe_{0.9}Co_{0.1}Ge$ at $T = 150$ K, $Fe_{0.6}Co_{0.4}Ge$ at $T = 100$ K and $Fe_{0.4}Co_{0.6}Ge$ at $T = 75$ K which correspond to $T \sim T_c/2$ for each x concentration respectively.

At temperatures $T = T_c/2$ and above, the relation shown in Eq. 6.3 applies to compositions up to $x = 0.6$ and the fits are shown in Fig. 6.8 for $Fe_{0.9}Co_{0.1}Ge$ at $T = 250$ K, $Fe_{0.6}Co_{0.4}Ge$ at $T = 260$ K and $Fe_{0.4}Co_{0.6}Ge$ 0.6 at $T = 250$ K.
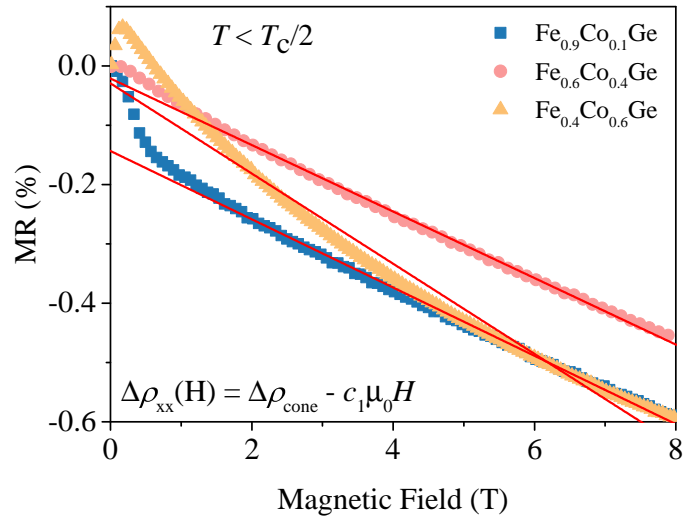
Figure 6.7: Magnetoresistance at $T < T_c/2$ for $Fe_{0.9}Co_{0.1}Ge$ at $T = 150$ K, $Fe_{0.6}Co_{0.4}Ge$ at $T = 100$ K and $Fe_{0.4}Co_{0.6}Ge$ at $T = 75$ K fitted using Eq. 6.2.
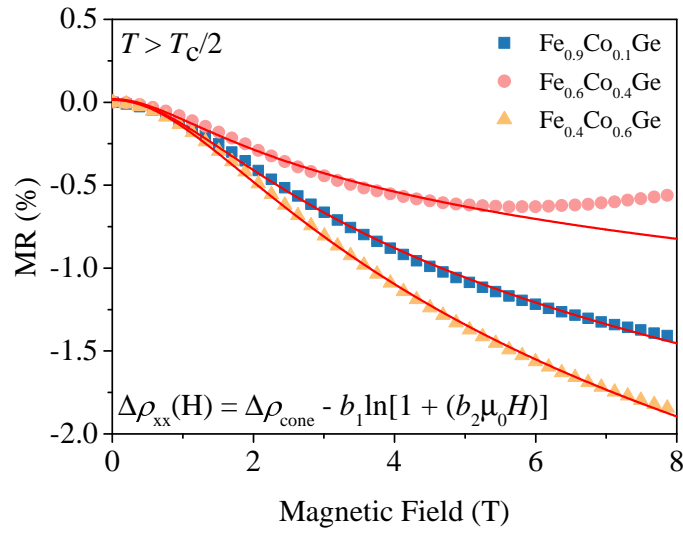
Figure 6.8: Magnetoresistance at $T > T_c/2$ for $Fe_{0.9}Co_{0.1}Ge$ at 250 K, $Fe_{0.6}Co_{0.4}Ge$ at 260 K and $Fe_{0.4}Co_{0.6}Ge$ at 250 K, fitted using Eq. 6.3.

6.3.2 Low-field (below H_c) conical MR

The conical MR at low-field ($H < H_c$) ρ_{cone} has been described using a giant magnetoresistance type model in Ref. [42] given by

$$\frac{\Delta\rho_{cone}}{\rho_{xx}} = -\left(\frac{\Delta\rho_{max}}{\rho_{xx}}\right)\frac{1}{2}[1 + \cos\psi], \tag{6.4}$$

where ψ is the angle between neighbouring spins and $\Delta\rho_{max}$ is the change in resistivity between spins being aligned parallel and antiparallel. The full derivation is given in Ref. [42] and results in

$$-\left(\frac{\Delta\rho_{cone}(H)}{\rho_{xx}}\right) = \left(\frac{\Delta\rho_{max}}{\rho_{xx}}\right)\frac{1}{2}\left[1 + \left\{f + (1-f)\left(\frac{M(H)^2}{M_s}\right)\right\}\right], \tag{6.5}$$

where ρ_{max} is the peak resistivity due to the conical phase (the maximum resistivity difference is when the helix structure is unperturbed), f gives a measure of the reduction in MR due to the helix winding, $M(H)$ is the out-of-plane magnetization and M_s is the saturation magnetization. The main result is Eq. 6.5 shows an expected relation of the conical resistivity $\rho_{cone} \propto M^2$.

The MR of the conical phase ρ_{cone} for $0 \leq x \leq 0.5$ at 5 K as a function of M^2 is shown in Fig. 6.9. The linear fits to the data indicate this proportionality is present and shows this model is able to describe these compositions.
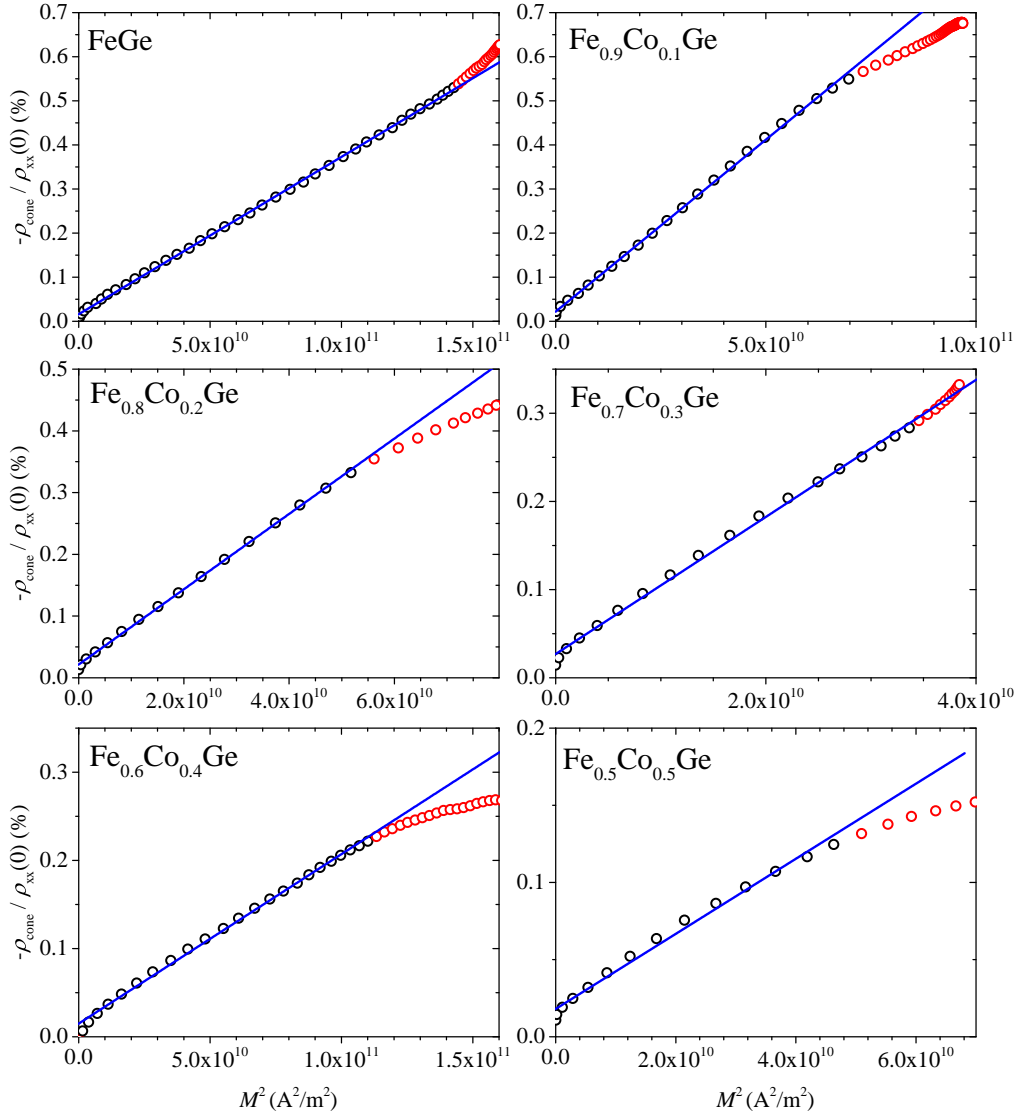
Figure 6.9: Conical magnetoresistance ρ_{cone} as a function of M^2 for $\mathrm{Fe}_{1-x}\mathrm{Co}_x\mathrm{Ge}$ with $0 \leq x \leq 0.5$ at 5 K. Linear fit to data points below H_c (black circles) shown by solid line (blue) show proportionality $\rho_{\mathrm{cone}} \propto M^2$. Data above H_c (red circles) deviates from this scaling relation.

6.4 Hall effect

The Hall effect is produced by several contributions and for B20 helimagnets the Hall resistivity ρ_{xy} takes the form:

$$\rho_{xy} = \rho_{xy}^{\text{OHE}} + \rho_{xy}^{\text{AHE}} + \rho_{xy}^{\text{THE}}. \tag{6.6}$$

The first term is the ordinary Hall effect (OHE) which occurs in any material where a current is subject to a perpendicular magnetic field and this term depends on the strength of the applied field. The second term is the anomalous Hall effect (AHE) which occurs in ferromagnetic materials and depends on the magnetization of the sample. Generally the first two terms are sufficient to describe ρ_{xy} and this is given by

$$\rho_{\text{xy}} = R_0 \mu_0 H + R_s M, \tag{6.7}$$

where R_0 is the Hall coefficient, R_S is the anomalous Hall coefficient and M is the magnetization along the direction of the applied field. The final term is the topological Hall effect (THE) and is present in systems that exhibit non-trivial spin textures such as skyrmions, which have been shown to be present in B20 structure materials [47].

6.4.1 Ordinary Hall effect

Hall resistivity ρ_{xy} measurements were taken simultaneously with the longitudinal MR at various temperatures from 5 K to room temperature in out-of-plane applied fields of up to ± 8 T. The measured ρ_{xy} for all compositions of x at 5 K are shown in Fig. 6.10 and the results for all temperatures are shown in Fig. 6.13. From Fig. 6.10 for FeGe a positive OHE is seen with a small AHE at low temperature, consistent with previous measurements [42]. With the introduction of Co (increasing x) the OHE becomes negative and a large increase in the AHE resistivity is seen. As $x \to 0.5$ the OHE is found to increase to a maximum at $x = 0.5$ and as $x \to 0.7$, the OHE decreases. At $x = 0.8$ the OHE becomes positive and for CoGe a large positive OHE is seen with no sign of any other contributions.

The ρ_{xy} data was examined using a linear fit at high field (well beyond magnetic saturation) with Eq. 6.7 where the gradient of ρ_{xy} gives R_0 and the intercept at zero-field gives $R_s M_s$ where M_s is the saturation magnetisation. An example of the fitting for two x values 0 and 0.4 is shown in Fig. 6.11.
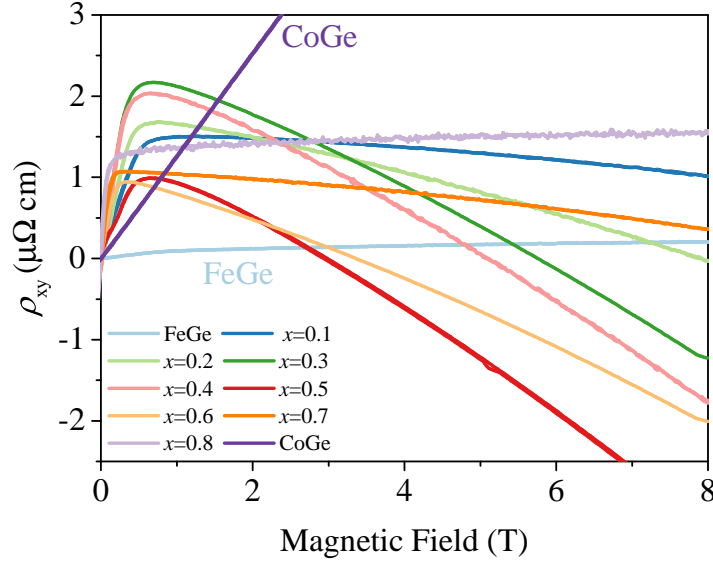
Figure 6.10: Measured Hall resistivity with applied field ± 8 T for 20 μm Hall bars of $Fe_{1-x}Co_xGe$ for all concentrations of x at 5 K.

From the measured ρ_{xy}, R_0 is shown for all concentrations up to 200 K in Fig. 6.12. The values shown in Fig. 6.12 are taken using fit of ρ_{xy} at high fields between 4 and 8 T and averaged across both the positive and negative field directions. Here it can be seen that from $x = 0$ to 0.5, R_0 increases by an order of magnitude, peaking at $x = 0.5$. For FeGe the value for R_0 at 5 K is found to be 0.0122(2) $\mu\Omega$ cm/T and the maximum at $x = 0.5$ is found to be -0.681(2) $\mu\Omega$ cm/T. For CoGe R_0 is found to be 1.2812(6) $\mu\Omega$ cm/T.

Figure 6.12 also shows R_0 is temperature dependence and is found to decrease for all x with increasing temperature. At 200 K, $0 \leq x \leq 0.3$ fall to zero and a change in gradient starts, indicating a change in carrier type. For higher x this happens at lower temperatures, corresponding to the reduced T_c.

In FeGe at increased temperature, ~ 200 K and above, a non-linearity is seen in the OHE at high field (above H_c), which is not shown here. This effect can occur when there are two or more types of carriers with different mobilities and has been identified previously in FeGe films [42]. This effect can also be seen in the $Fe_{1-x}Co_xGe$ films, for example in Fig. 6.13 and occurs for $0.1 \leq x \leq 0.8$ with the temperature threshold decreasing from ~ 200 K as x is increased which corresponds to the reduction in T_c. Due to this effect, analysis has been focused on temperatures 200 K and below in the following sections.
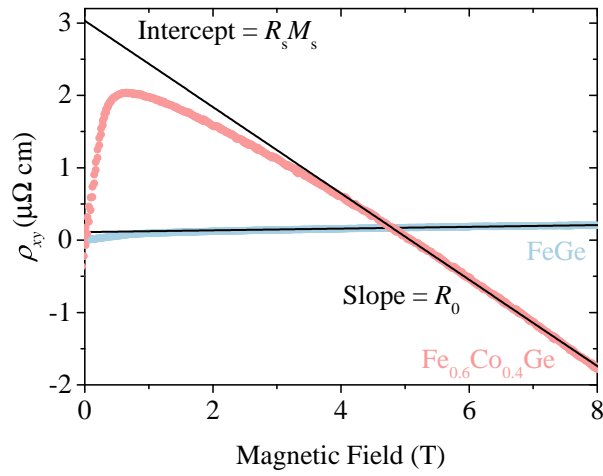
Figure 6.11: Measured Hall resistivity with applied field ± 8 T for 20 μm Hall bars of $Fe_{1-x}Co_xGe$ for all concentrations of x at 5 K.
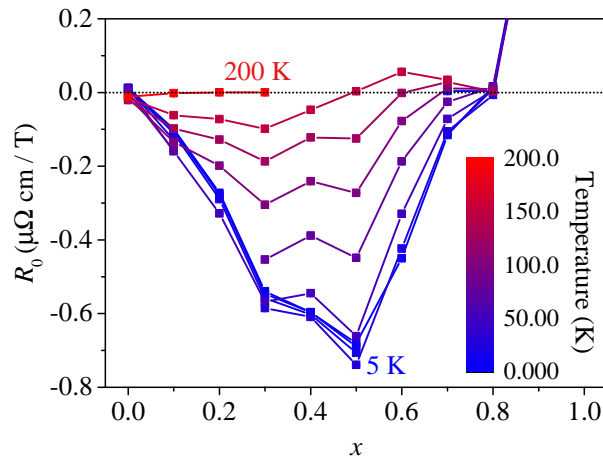
Figure 6.12: Magnitude of the ordinary Hall coefficient R_0 as a function of concentration x for temperatures up to 200 K.
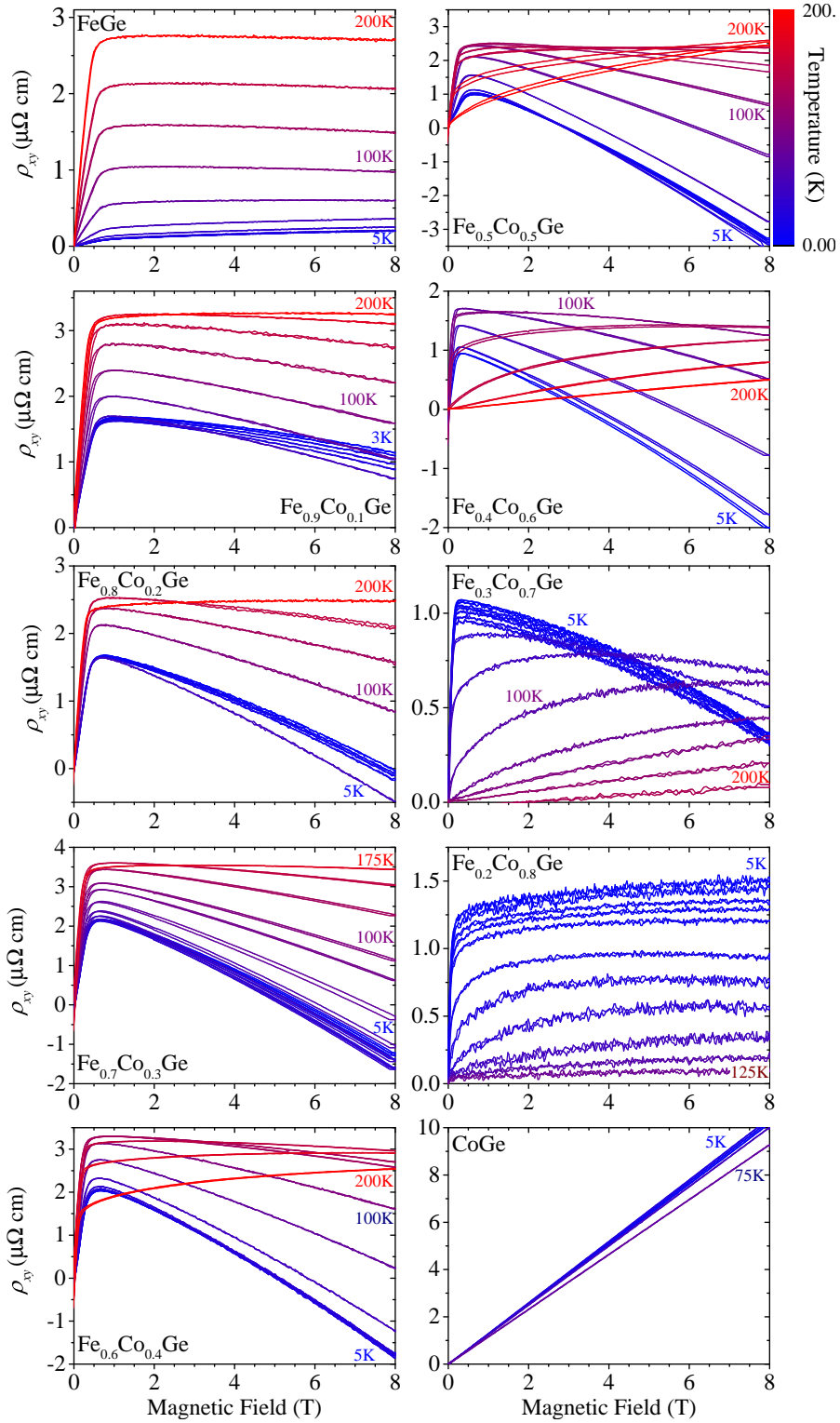
Figure 6.13: Measured Hall resistivity with applied field ± 8 T for 20 μm Hall bars of $Fe_{1-x}Co_xGe$ for all concentrations of x from 5 K to 200 K. Minor splitting is seen in some measurements due to temperature drift.

6.4.2 Anomalous Hall effect

The AHE is present in ferromagnetic materials and comprises three mechanisms [87]:

$$\rho_{xy}^{\mathrm{AHE}} = \left(\alpha\rho_{xx} + \beta\rho_{xx}^2 + b\rho_{xx}^2 \right) M(H). \tag{6.8}$$

The first two terms, with pre-factors α and β are called the skew and side-jump scattering respectively and are extrinsic effects which arise from electron scattering within the crystal due to disorder. The skew scattering arises from asymmetric scattering due to spin-orbit coupling with other electrons or impurities [87]. The side-jump scattering is due to the deflection of the electron by the opposite electric fields it experiences when approaching and leaving an impurity [87]. The final term is called the intrinsic scattering and is related to the Berry curvature. An applied electric field gives rise to an additional velocity perpendicular to the field direction which can contribute to the Hall signal.

Using Eq. 6.7 and extrapolation to zero-field the value of ρ_{xy}^{AHE} can be determined. The results as function of temperature for each composition of x up to 200 K are shown in Fig. 6.14. For FeGe the AHE is seen to increase with temperature and approaches a maximum at 200 K, consistent with previous experiments [42]. For the intermediate $Fe_{1-x}Co_xGe$ compositions, on introduction of Co a sudden jump in the AHE at 5 K is seen as it increases from 0.11 $\mu\Omega$ cm for FeGe to 1.74 $\mu\Omega$ cm for $x = 0.1$. At 5 K the AHE is seen to increase with x up to a maximum at $x = 0.4$, beyond this it starts to decreases. For CoGe no sign of an AHE is seen which is consistent with the magnetometry results presented in Chapter 5, which show the material is non-magnetic. As the temperature is varied the behaviour of the AHE is found to show a peak that decreases in temperature as $x \to 1$. The maximum AHE value is found for $x = 0.3$ of 3.83 $\mu\Omega$ cm.
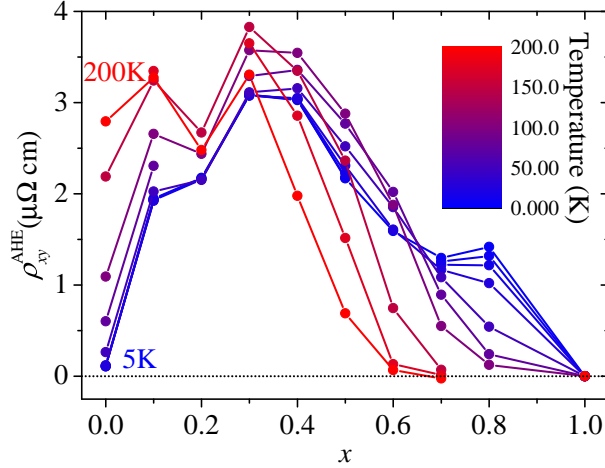
Figure 6.14: Temperature dependence of the anomalous Hall effect ρ_{xy}^{AHE} for all concentrations of x.

6.4.3 Scaling of the anomalous Hall effect in $\mathrm{Fe}_{1-x}\mathrm{Co}_x\mathrm{Ge}$

To investigate the AHE scaling measured in $\mathrm{Fe}_{1-x}\mathrm{Co}_x\mathrm{Ge}$, we first look at the components α, β and b as and give the ρ_{xy}^{AHE} as just a function of the resistivity ρ_{xx}

$$\rho_{AH} = \alpha\rho_{xx} + (\beta + b)\rho_{xx}^2, \tag{6.9}$$

where ρ_{AH} takes the value of ρ_{xy}^{AHE}. To look at the individual components, a plot of

$$\rho_{\mathrm{AH}}/\rho_{xx} = \alpha + (\beta + b)\rho_{xx} \tag{6.10}$$

can be used to separate the contributions. By using Eq. 6.10 we observe distinct regions in the $\mathrm{Fe}_{1-x}\mathrm{Co}_x\mathrm{Ge}$ films $0.1 \leq x \leq 0.8$ where linear behaviour as described by Eq. 6.10 applies only within certain temperature regions.

To highlight the dependence of the AHE scaling on the inflection points found in the $\rho_{xx}(T)$ data (shown in Fig. 6.1) we have identified regions of temperature where the scaling between the AHE and ρ_{xx} changes and found the crossover between regions correspond to the residual resistivity ρ_{xx0} and near the resistivity peak ρ_{peak}. The $\rho_{xx}(T)$ and scaled anomalous Hall resistivity for selected x are shown in Fig. 6.15. The compositions of x chosen are $x = 0$, 0.3, 0.5, and 0.7 which demonstrate the onset of the ρ_{peak} and tracks how its position in temperature decreases as x is increased which corresponds to the decreasing T_{c}, as demonstrated in Fig. 6.1. In Fig. 6.15 a) for FeGe,

no ρ_{peak} is seen, however looking at the scaling between ρ_{AH} and ρ_{xx} shown in e) it is linear up to ~ 200 K before changing. This area is shown in a) by the dashed line as region 2. On increasing x to 0.3 in b) and 0.5 in c) a peak can be seen to emerge in $\rho_{xx}(T)$ and the corresponding scaling shown in f) and g) shows a linear response is seen below ρ_{peak} and above ρ_{xx0}. In these compositions region 1 emerges and is found to coincide with the residual resistivity ρ_{xx0}. In d) for $x = 0.7$ we observe the position of ρ_{peak} has decreased significantly and the scaling shown in g) shows two distinct regions.

From these observations we can expect that since region 1 aligns with ρ_{xx0} the effect causing the increase in resistivity at low temperature is also responsible for the change in scaling. For the linear scaling in region 2, since this extends up to just below ρ_{peak} which is related to T_{c} this is a magnetic region which also aligns with the high-field background MR region, seen in Sect. 6.3.1. At higher temperatures it appears the scaling also changes, again with similarity to Sect. 6.3.1 and may arise from the spin fluctuations seen there.
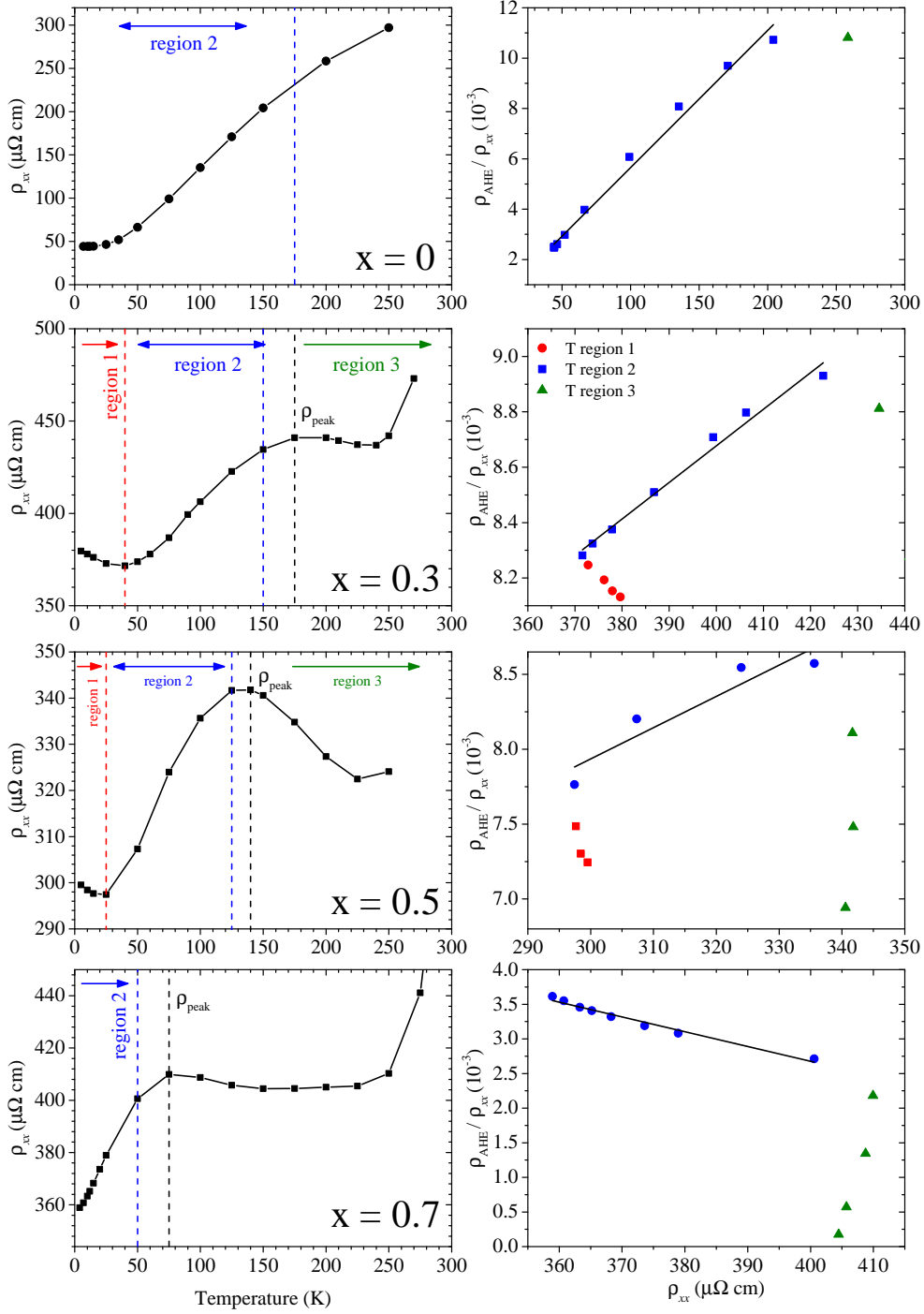
Figure 6.15: Temperature dependent resistivity $\rho_{xx}(T)$ a-d) and anomalous Hall effect scaling e-h) for selected values of $x = 0$, 0.3, 0.5, and 0.7, highlighting a change in scaling as different temperature regions are examined. a-d) Dashed lines indicate crossover regions and ρ_{peak}. e-h) change in symbol correspond to $T <$ region 1 (square), $T =$ region 2 (circle) and $T >$ region 3 (triangle).

Using Eq. 6.10 the parameters for the skew α and the side-jump and intrinsic $(\beta + b)$ can be found. By restricting our analysis to region 2 for the $Fe_{1-x}Co_xGe$ films, linear fits using Eq. 6.10 have been plotted for $x = 0 \leq x \leq 0.8$ in Fig. 6.16.

The values from the fits are summarised in Fig. 6.17. Fig. 6.17 shows α and $(\beta + b)$ as a function of x. From this graph we can see the two parameters tracking each other, however α can be seen to rise with x along with $(\beta + b)$. The initial jump in AHE between FeGe and $Fe_{0.9}Co_{0.1}Ge$ may be explained by the large increase in the skew-scattering term shown in Fig. 6.17 which could be indicative of a sudden increase in disorder. To further investigate the AHE, we look at the ρ_{xy} scaled by the saturation magnetisation. Plots of each sample are shown in Fig. 6.18 and the inset shows the corresponding M_s used for each sample. The solid lines show the fit using Eq. 6.8 and the dashed line shows a fit dependent only on a ρ_{xx}^2 term. This dependence was used to identify the scaling in FeGe [42] and describes the data well at low x, whereas a fit of the form $b\rho_{xx}$ shows a large deviation at higher x.

In recent work, theoretical calculations for the AHE in $Fe_{1-x}Co_xGe$ have been made in collaboration with this study and are presented in Ref. [86]. The experimental values shown here are compared to theoretical values and a general agreement is seen between the anomalous Hall conductivity.

By looking at the scattering contributions to the AHE it was hoped that an accurate value for the AHE could be determined for subtraction from the total resistivity in calculating the THE. However, as will be seen in Sect. 6.4.4, despite the varying proportion of *alpha* and $(\beta + b)$, the introduction of a skew-scattering term had negligible effect on the resulting THE results.
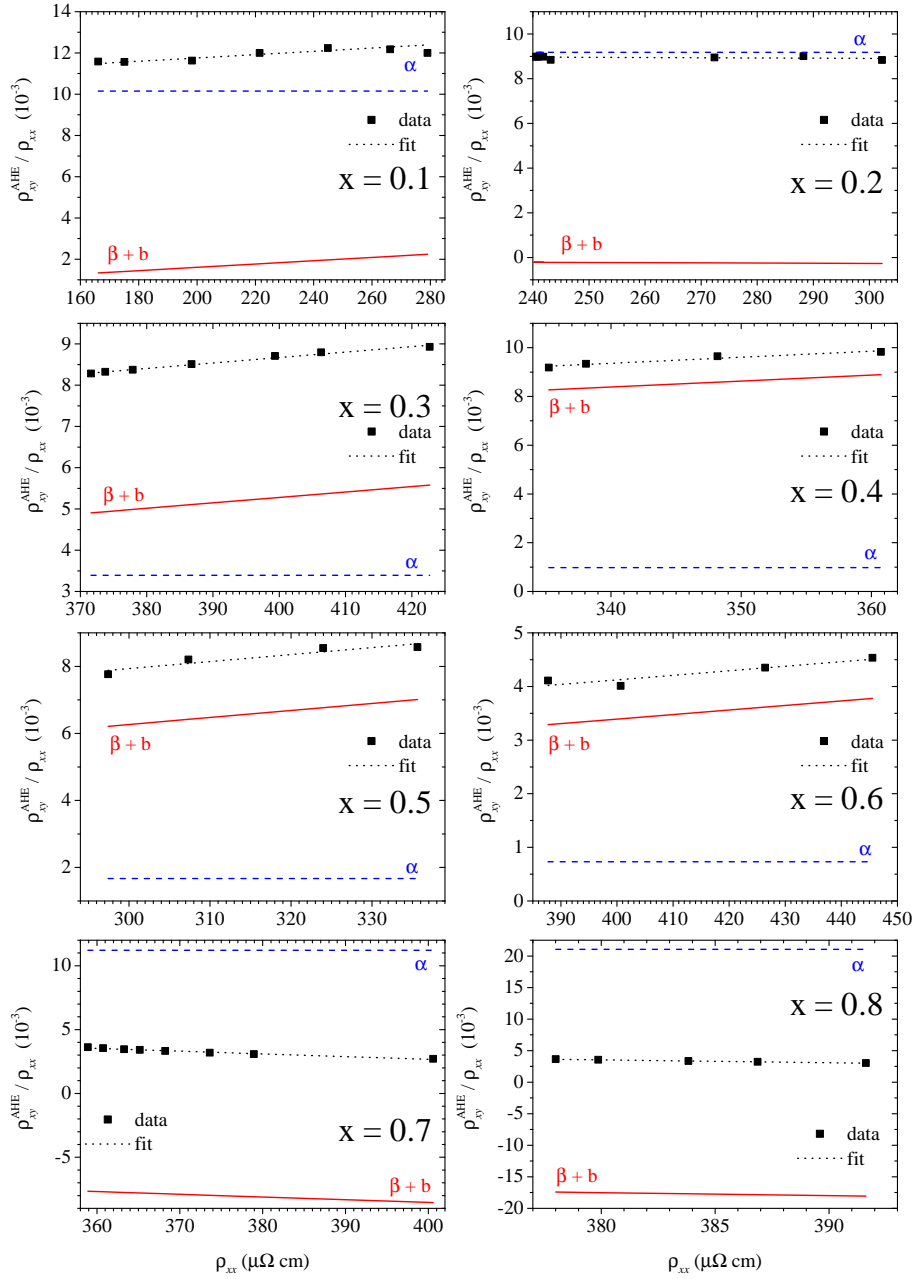
Figure 6.16: Scaling of ρ_{AH} with ρ_{xx} for Fe$_{1-x}$Co$_x$Ge films with $0.1 \leq x \leq 0.8$ within the linear region between ρ_{peak} and ρ_{xx0}.
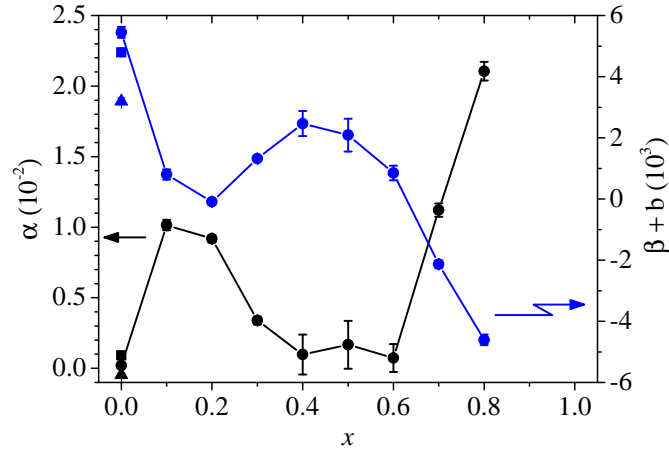
Figure 6.17: Anomalous Hall effect scaling parameters, α, $(\beta + b)$ as a function of $Fe_{1-x}Co_xGe$ film composition x.
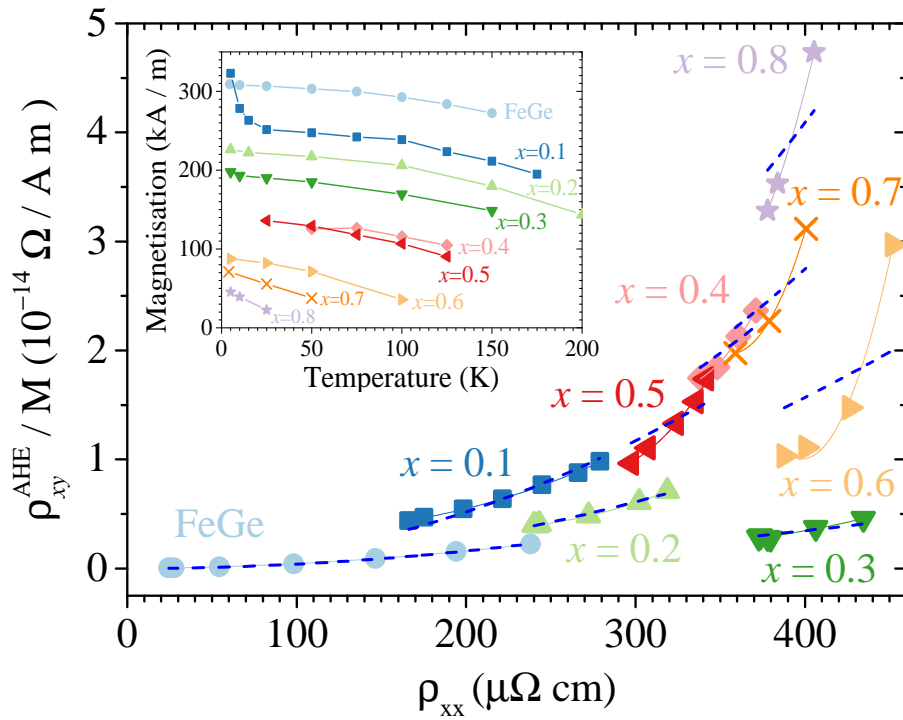
Figure 6.18: Anomalous Hall effect scaled by the saturation magnetisation for $Fe_{1-x}Co_xGe$ with $0 \leq x \leq 0.8$. Lines show fit to data using Eq. 6.8 and dashed lines show $b\rho_{xx}^2$ dependence only. Inset shows out-of-plane saturation magnetisation used. Note that scaling works well for low x, but breaks down for $x = 0.4$ and higher.

6.4.4 Topological Hall effect

In the B20 group, magnetic skyrmions have been observed in the parent materials, transition metal monosilicides and germanides and their intermediary compositions. It is expected that a material hosting these magnetic textures will display the topological Hall effect and this has been observed in bulk crystals MnSi [47, 88], MnGe [74], and epitaxial films of MnSi [89] and FeGe [41–43].

The THE appears in materials that exhibit topologically non-trivial spin textures such as skyrmions. In B20 materials which host magnetic skyrmions this effect arises from electrons passing through these structures and experiencing an emergent field produced by the skyrmion. The additional resistivity has been estimated to be given by [47]

$$\rho_{xy}^{\text{THE}} = PR_0 B_{\text{eff}}, \tag{6.11}$$

where P is the charge carrier spin polarisation and B_{eff} is the emergent field. B_{eff} is the emergent field associated with the Berry phase arising from the topological winding of the skyrmion spin texture [47]. It is quantised to one magnetic flux quantum per skyrmion and is given by

$$B_{\text{eff}} = \frac{h}{e} \left(\frac{\sqrt{3}}{2\lambda_{\text{s}}^2} \right), \tag{6.12}$$

where λ_{s} is the skyrmion lattice wavelength, assuming a hexagonal lattice structure [88] and is related to the helical wavelength through, $\lambda_{\text{s}} \approx \lambda_{\text{h}}$. This effective field depends on the size of the magnetic skyrmions and the density of the structures when packed in a lattice. An electron passing through this spin texture experiences this effective magnetic field, which acts to deflect it causing an additional component to the Hall resistivity.

Above magnetic saturation H_{c} all moments are collinear and any topological structure is expected to be destroyed, thus the measured resistivity ρ_{xy} is expected to only contain contributions from the $\rho_{xy}^{\text{OHE}} + \rho_{xy}^{\text{AHE}}$. By finding the OHE and AHE contributions at high field above H_{c} and subtracting the result from the measured data, the low field topological contribution can be found [47].

For FeGe it has been previously shown the skew scattering component is negligible [42] and the AHE was found to depend only on the ρ_{xx}^2 components. In the previous section we observed the scaling dependence of these components and verified this negligible relationship for FeGe. In the case of $\text{Fe}_{1-x}\text{Co}_x\text{Ge}$ we find a significant change in the scaling for higher x, where the skew scattering α increases. However, when applied

to the THE fit as described below, it had only a minimal effect, indicating the scaling relations are more sensitive to temperature than applied field. Assuming the total resistivity comprises ρ_{xy}^{OHE}, ρ_{xy}^{AHE} and ρ_{xy}^{THE} as per Eq. 6.6 the Hall resistivity is given by

$$\rho_{\text{xy}} = R_0 H + R_s M(H) + \rho_{\text{xy}}^{\text{THE}}, \tag{6.13}$$

where the scaling of R_s is given by $S_A \rho_{\text{xx}}^2$ where S_A is the scaling factor for longitudinal resistivity. Above H_c the ρ_{xy}^{THE} vanishes, so

$$\rho_{\text{xy}}(H > H_c) = R_0 H + R_s M(H) = R_0 H + S_A \rho_{\text{xx}}^2 M(H), \tag{6.14}$$

and from this form the coefficients R_0 and S_A can be determined by rearranging Eq. 6.14 by dividing through by H giving

$$\rho_{xy}/H = R_0 + S_A \rho_{xx}^2 M/H. \tag{6.15}$$

By plotting ρ_{xy}/H against $\rho_{xx}^2 M/H$ the coefficients R_0 and S_A can be found. This procedure has been used to determine the THE previously in bulk crystal [47, 74, 89] and epitaxial films [41, 42, 77].

An example of applying this method to our data is shown in Fig. 6.19. Here the data measured from $x = 0.1$ is shown. In a) the required magnetization M and longitudinal resistivity ρ_{xx} is shown. In b) a plot of ρ_{xy} / H versus $\rho_{\text{xx}}^2 M(H)/H$ is shown and a linear fit is used to obtain R_0 and R_s. c) shows the measured ρ_{xy} and the fit produced using eqn. 6.14 extrapolated back to zero field. d) shows the resulting ρ_{xy}^{THE} by subtracting the fit produced from the measured Hall data $\rho_{xy}^{\text{THE}} = \rho_{xy}$ - $\rho_{\text{xy}}(H > H_c)$.

The measured ρ_{xy} and fits for $0.1 \leq x \leq 0.8$ at 5 K are given in Fig. 6.20. The data was fitted using Eq. 6.15 above saturation H_c, which was set at $H_c = 0.8$ T for consistency across the group. In Fig. 6.20 the ρ_{xy}^{THE} magnitude, taken from the maximum in the peak, can be seen to increase from $x = 0.1$ to $x = 0.4$. On increasing x it starts to decrease and a crossover from negative to positive is seen at $x = 0.7$. The maximum seen at $x = 0.4$ gives a ρ_{xy}^{THE} of -0.39 $\mu\Omega$ cm. The resulting fitting parameters from Fig. 6.20 are shown in Fig. 6.21. a) shows the AHE fitting parameters S_A and R_S. S_A was multiplied by the zero-field ρ_{xx}^2 to obtain R_S. b) shows a comparison between the R_0 coefficients found from the fits (circles) and the values obtained from high-field fits of ρ_{xy} (triangles). The general trend of the two curves are similar, with larger values at the middle compositions, however the magnitude has increased significantly. This could
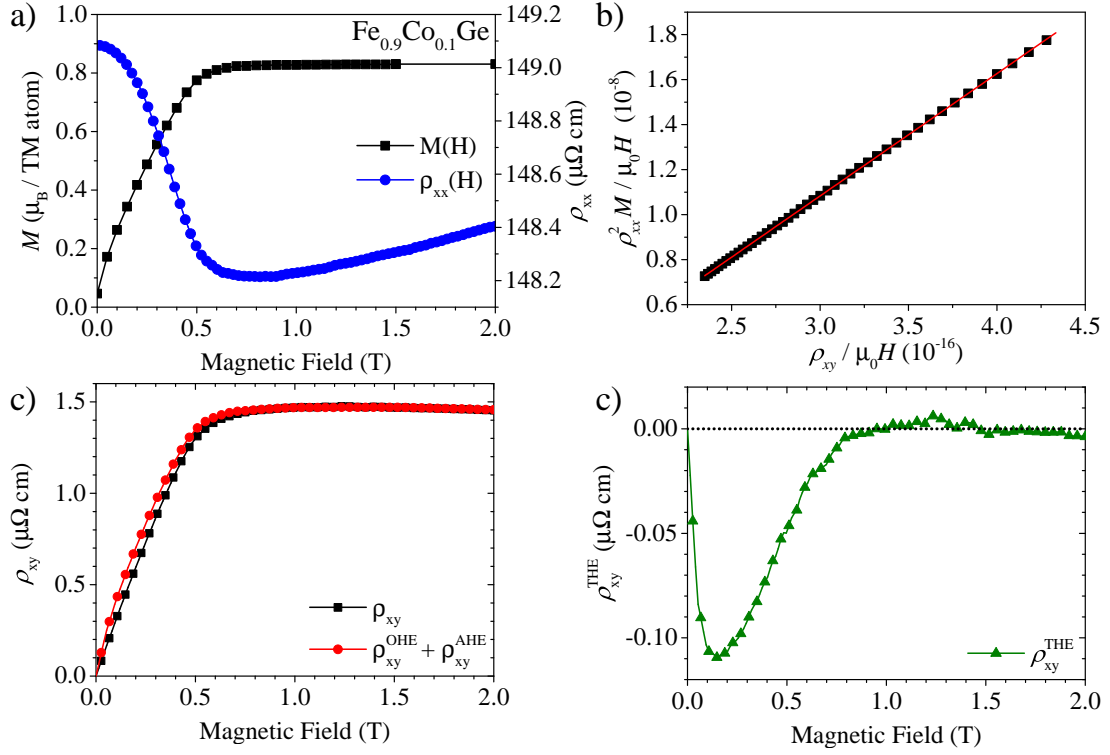
Figure 6.19: Fitting procedure for extraction of ρ_{xy}^{THE}, example shown for $\mathrm{Fe_{0.9}Co_{0.1}Ge}$ at 5 K. a) Magnetization $M(H)$ and longitudinal resistivity ρ_{xx}. b) Plot of $\rho_{xy}/\mu_0 H$ versus $\rho_{xx}^2 M/\mu_0 H$. c) Measured Hall resistivity ρ_{xy} and scaled magnetisation data using the fitting parameters from b) above H_{c} using coefficients from b). d) Resulting difference between measured data and model.

indicate the ρ_{xy} has not fully saturated after H_{c} or is slightly non-linear above H_{c} and so the high-field data may not fully capture R_0. Fig. 6.21 c) shows the magnitude of ρ_{xy}^{THE} as a function of x.
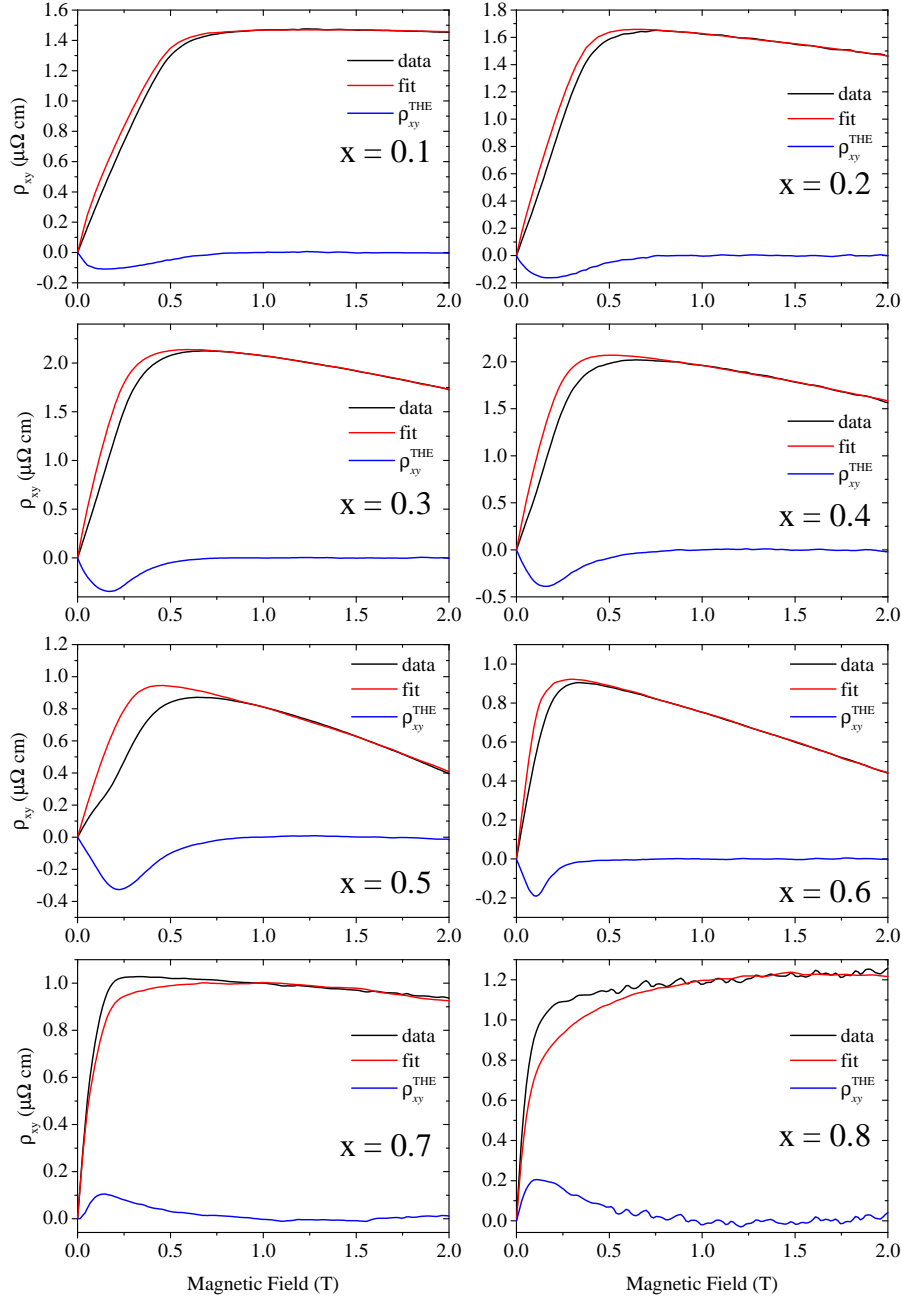
Figure 6.20: Measured Hall resistivity and fit using Eq. 6.14 with resulting topological Hall resistivity ρ_{xy}^{THE} at 5 K for $\mathrm{Fe}_{1-x}\mathrm{Co}_x\mathrm{Ge}$ with $0.1 \leq x \leq 0.8$ in a)-h) respectively.
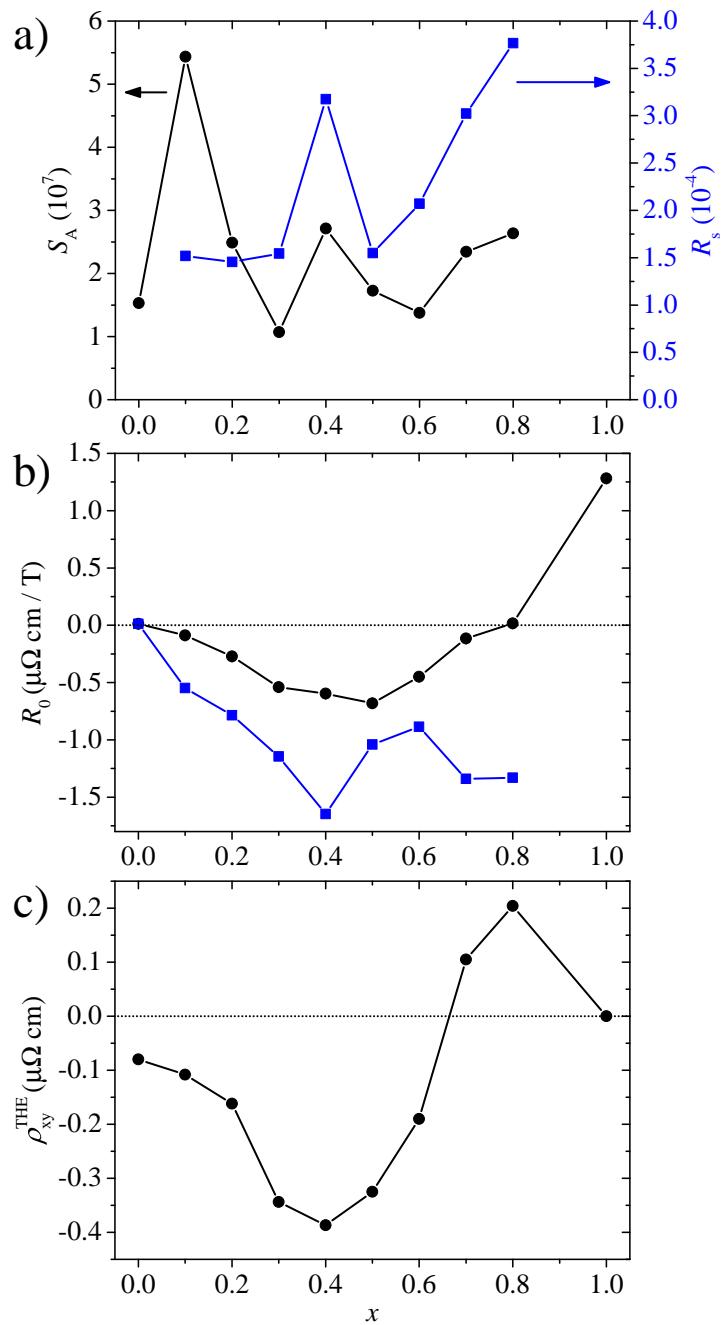
Figure 6.21: Parameters taken from fits to ρ_{xy} shown in Fig. 6.20. a) resulting S_A (circles) and R_S (squares) from fits to ρ_{xy} . b) R_0 (circles) from high field data and R_0 (squares) from fits to ρ_{xy} . c) Magnitude of ρ_{xy}^{THE} as a function of x.

We also investigated the temperature dependence to ρ_{xy}^{THE} from 5 K to 150 K for selected samples of $Fe_{1-x}Co_xGe$. The resulting THE for various temperatures are shown in Fig. 6.22 for $Fe_{0.9}Co_{0.1}Ge$, $Fe_{0.8}Co_{0.2}Ge$, $Fe_{0.6}Co_{0.4}Ge$, $Fe_{0.5}Co_{0.5}Ge$, $Fe_{0.4}Co_{0.6}Ge$ and $Fe_{0.2}Co_{0.8}Ge$. It can be seen that the peak magnitude and position in field is both temperature and composition dependent.
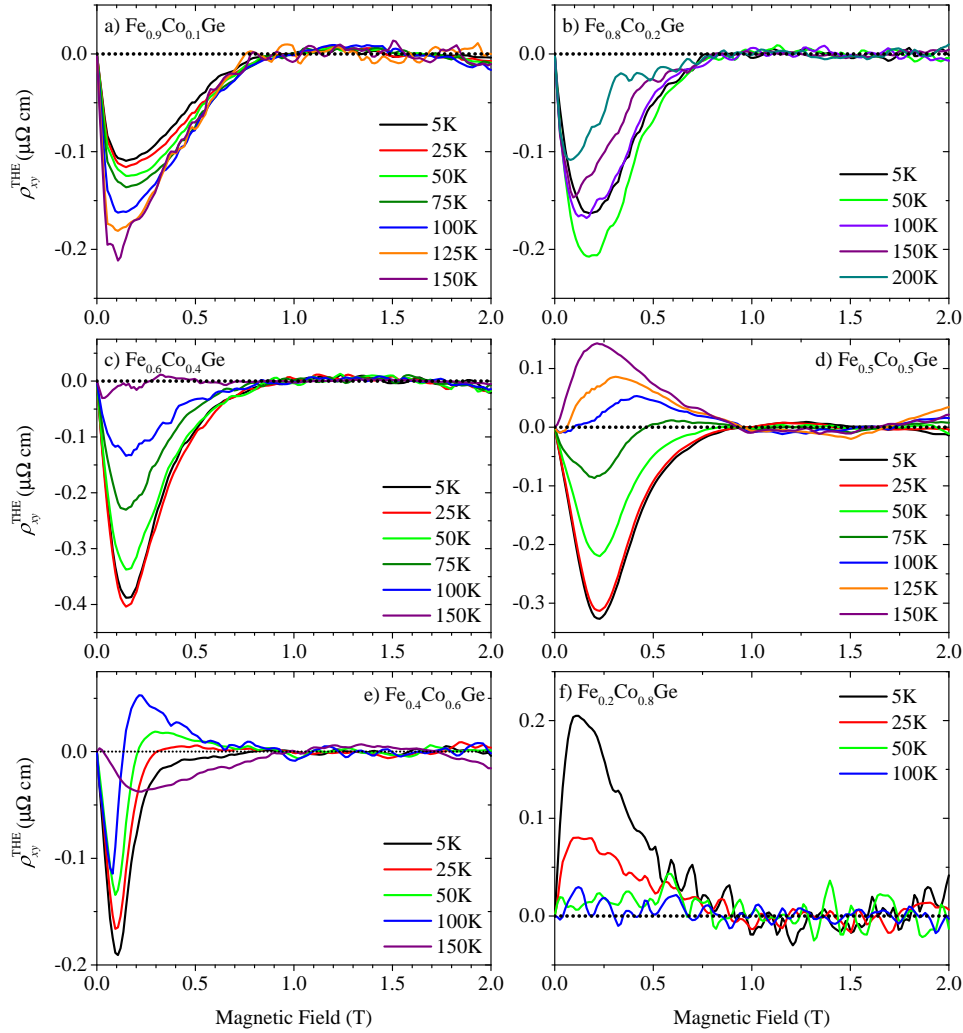
Figure 6.22: Topological Hall effect resistivity ρ_{xy}^{THE} at various temperatures from 5 K to 200 K for a) $Fe_{0.9}Co_{0.1}Ge$, b) $Fe_{0.8}Co_{0.2}Ge$, c) $Fe_{0.6}Co_{0.4}Ge$, d) $Fe_{0.5}Co_{0.5}Ge$, e) $Fe_{0.4}Co_{0.6}Ge$ and f) $Fe_{0.2}Co_{0.8}Ge$.

6.4.5 Discussion of the topological Hall effect in B20 materials

The topological Hall effect has been shown to exist previously in bulk crystal B20 materials and films of TM monosilicides and germanides. However in B20 materials with mixed compositions, the THE has been reported in $Mn_{1-x}Fe_xSi$ [90] and $Fe_{1-x}Co_xSi$ [65], but has not been reported in any of the germanide compounds, although transport properties have been investigated [46]. The Hall resistivity has been investigated in bulk polycrystalline $Mn_{1-x}Fe_xGe$ [46] using the same analysis method used here (using Eq. 6.13 without a ρ_{xy}^{THE} component) however, low-field discrepancies attributed to the THE were reported to not exist, while MnGe shows a large signal, -0.16 $\mu\Omega$ cm.

In literature there are several examples of measuring THE from a B20 thin film, however there are several contradictions. The original THE measurement in MnSi [47] was given as complementary evidence to support picture of magnetic skyrions in the so-called A-phase of MnSi. The additional resistivity that was detected in this phase corresponded extremely well with the prediction from Eq. 6.11. By using the resistivity experimentally measured and the known λ_h for MnSi, the ρ_{xy}^{THE} value of -0.0045 $\mu\Omega$ cm was explained well using a B_{eff} of -2.5 T, $P = 0.1$, and R_0 value taken at room temperature of 0.017 $\mu\Omega$ cm/T to produce a predicted value of -0.004 $\mu\Omega$ cm.

However, it was later recognised by the same authors [88] that the original values used were incorrect and the B_{eff} had been underestimated and the correct value was -13.15 T. Also it was recognised that the R_0 used should be at the corresponding temperature which was -0.008 $\mu\Omega$ cm/T at low temperature which produced an estimated value of 0.011 $\mu\Omega$ cm which was now twice the size and the sign had changed. Although an explanation for having a smaller ρ_{xy}^{THE} could be that the SkL was incomplete, as B_{eff} here assumes a packed hexagonal lattice.

From further investigation into reported THE values, FeGe is the most widely reported B20 germanide and all reports have used thin films [41–43, 77]. The values of ρ_{xy}^{THE} reported vary wildly from -0.04 $\mu\Omega$ cm to -0.92 $\mu\Omega$ cm across different t_{film} and temperature showing a large range, values for R_0 and ρ_{xy}^{THE} are given in Fig. 6.23 a) and b) respectively. For FeGe a well defined λ_h is known of 70 nm, using Eq. 6.12 with $P = 1$, $B_{eff} = $ -0.73 T. The first report by Huang *et al.* [41] approximated this value to 1 T and used 6.11 to calculate an expected ρ_{xy}^{THE}. The experimental ρ_{xy}^{THE} was -0.08 $\mu\Omega$ cm for a 300 nm thick film at 150 K, Using R_0 from 380 K of 0.072 $\mu\Omega$ cm/T and the approximate B_{eff}, 1 T, they produced a value of 0.072 $\mu\Omega$ cm/T which again agrees nicely, however

R_0 has be used from a completely different temperature and the calculated value is the incorrect sign. From these studies it can be seen that care needs to be taken when using Eq. 6.11, which although a simple and intuitive model may not be able to fully explain the effects observed.

Another point of contention is the fitting procedure for the ρ_{xy}^{THE} that has been contested by Meynell *et al.* [91] where they attribute the additional resistivity to $\rho_{xy}^{\mathrm{other}}$, which is explained as additional scattering due to the conical phase itself and non-topological.

To examine our results we start by looking at the largest result. The largest ρ_{xy}^{THE} found was for $x = 0.4$ which is considerably larger than expected, due to larger λ_{h} that would lead to a larger skyrmion size and hence decreased B_{eff}. From this line of reasoning, strangely the largest ρ_{xy}^{THE} are seen near the middle of the group in x, which we have seen $\lambda_{\mathrm{h}} \to \infty$, and so should stretch any skyrmion until the B_{eff} disappears. This composition range does correspond to the samples where a distinct change in resistivity scaling was seen at low temperatures, below ρ_{xx0} (see Fig. 6.15) and an additional scattering process could be the origin, however as shown in the temperature study Fig. 6.22 the magnitude of ρ_{xy}^{THE} stays comparable up to 50 K, which is above ρ_{xx0}. Another inconsistency we observe is that in our samples we have a racemic mixture of left-handed and right-handed chiral grains, as shown by Fig. 4.6, and due to this grain structure it is unlikely for a fully dense hexagonal SkL phase to form. With skyrmions only being able to form where grains are large enough to support them, B_{eff} should drop as the density of the skyrmions decrease. This should then lead to a reduced ρ_{xy}^{THE} when compared to the predicted outcome from Eq. 6.11. However we observe the opposite, as the grain sizes remained consistent with varying x, Fig. 4.6, as λ_{h} increases fewer grains will be able to fully support a skyrmion structure and this would add an additional decrease in the ρ_{xy}^{THE}, but we still observe a peak in the ρ_{xy}^{THE} around $x = 0.4$.

Another interesting result we find is the change in sign of ρ_{xy}^{THE} in Fig. 6.20 for $x = 0.7$ and 0.8. Positive ρ_{xy}^{THE} was observed in MnSi by Li *et al.* [89] and the sign was found to change with decreasing temperature. They attribute the sign change in the ρ_{xy}^{THE} to a change in spin polarisation due to sensitivity to the Fermi level in MnSi. In our results we find the positive ρ_{xy}^{THE} remains for the temperatures measured for $x = 0.8$. Although recent theoretical calculations for the band structure in $\mathrm{Fe}_{1-x}\mathrm{Co}_x\mathrm{Ge}$ [86] have predicted a half-metal crossing point at $x = 0.6$, possibly explaining the transition from negative

to positive ρ_{xy}^{THE} if the Fermi level sweeps from one polarisation to the other.

From our findings it is clear that there is an additional component to the Hall resistivity below H_{c}. By inspection of the ρ_{xy} data at $H < H_{\text{c}}$, kinks in the ρ_{xy} can be seen at low field that are most prominent in $0.3 \leq x \leq 0.5$ and these features would not be expected for a ferromagnet described by Eq. 6.7. However without complementary evidence it is impossible to say for certain that it is from purely topological origin.
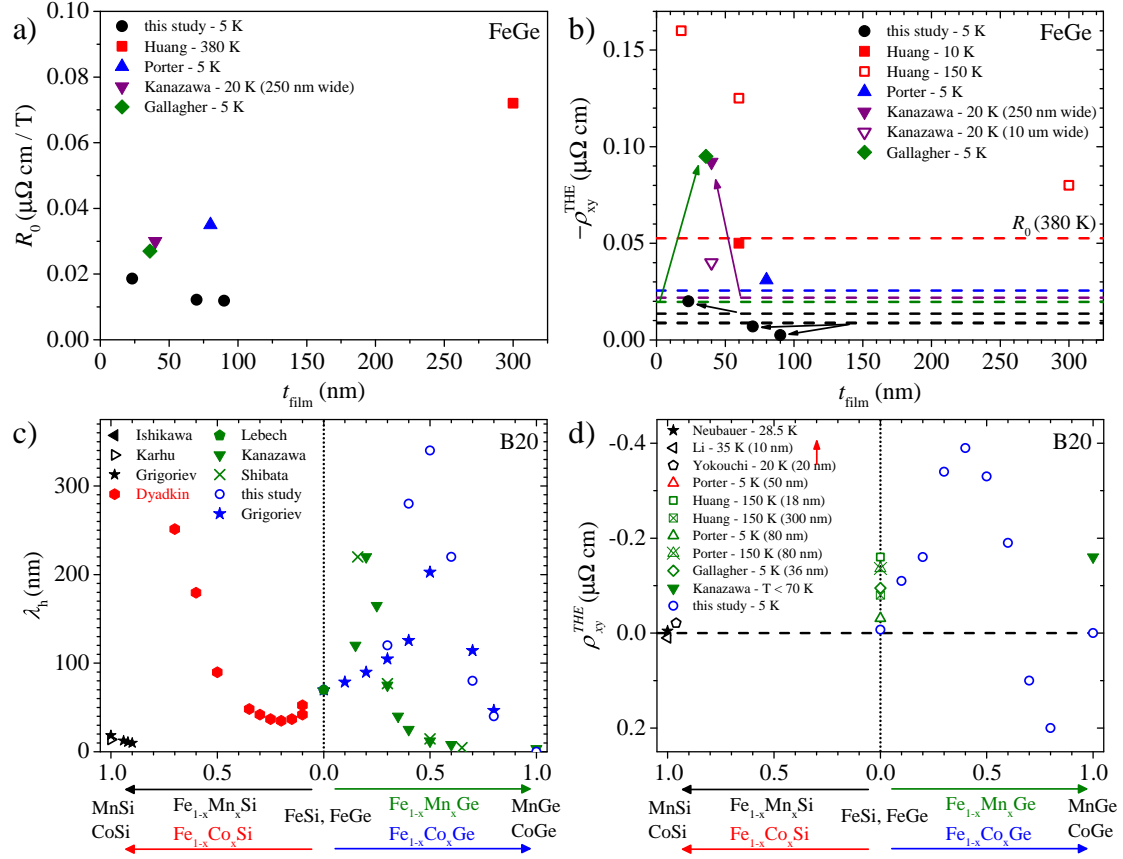
Figure 6.23: Review of transport, THE and helix wavelength λ_h for bulk crystal and thin film B20 materials. a) R_0 and b) ρ_{xy}^{THE} for various FeGe films. c) Helix wavelength for B20 materials, closed (open) symbols show bulk crystal (thin film) samples and blue (red) colour indicates germanides (silicides). (Sources for figures values a-b), d) Huang [41], Porter [44], Gallagher [43], Kanazawa [77], c) Dyadkin [92], Kanazawa [74], Grigoriev [28, 29], Neubauer [47] d) Yokouchi [90]).

6.5 Summary

In this chapter the transport properties of $Fe_{1-x}Co_xGe$ were examined across the whole range of compositions by varying x and over a range of temperatures from 5 K to room temperature. The temperature dependent resistivity of the $Fe_{1-x}Co_xGe$ samples showed all films to be metallic with ρ_{xx} decreasing with temperature. FeGe and CoGe both showed a classic $\rho_{xx}(T)$ curve whereas intermediate compositions, $0.1 \leq x \leq 0.8$, all showed a broad peak feature that was temperature dependent. The broad peak was found to occur below T_c, and as x was increased the peak occurred at lower temperatures corresponding to the reduction in T_c. The origin of this feature has not been identified, but thought to be magnetic as the onset of the peak occurs just below T_c for each composition.

The MR $\rho_{xx}(H)$ was measured at various temperatures and showed a diversity of behaviour with increasing x. The temperature dependent, high-field (H $> H_c$), behaviour for FeGe described in Ref. [42] was applied to $Fe_{1-x}Co_xGe$ and found to generally explain the results shown for temperature regimes scaled to T_c for $0.1 \leq x \leq 0.6$. However within these results there were discrepancies. The low-temperature (T $< T_c/4$) regime showing a change from quadratic to linear dependence on applied field with $x \to 0.6$. There was also a pocket of high-temperature (T = 200-290 K) measurements for $x = 0.2$-0.5 that showed a change of sign in the model coefficients, not seen in before, but generally the temperature regimes used to describe FeGe were applicable. However for large x this was not the case, for $x = 0.8$ no agreement was found below T_c and for CoGe only a background orbital MR was seen for 10 K and above.

For the low-field (H $< H_c$) region the conical MR described in Ref [42] was applied and a good agreement was found for $0.1 \leq x \leq 0.5$, this evidence further supports the presence of a helical structure, as described in Sect. 5.3, observed via an alternate method. The results show the initial dip in low-field resistivity is attributed to the helix structure being deformed into a conical state and the decreasing magnitude of the effect ρ_{cone} corresponds well to the increasing wavelength ($\lambda \to \infty$) we have observed as $x \to 0.5$. However for $x = 0.6$ and above the change in MR is not consistent with these findings and as x increases the behaviour of the MR changes significantly and no longer permits this type of analysis.

The Hall effect observed in $Fe_{1-x}Co_xGe$ shows distinct change when x is increased. On introduction of Co, the Hall constant R_0 greatly increases indicating a reduction in

the carrier concentration, the gradient also changes sign from positive (FeGe) to negative ($Fe_{1-x}Co_xGe$ $0.1 \leq x \leq 0.7$) indicating a change in carrier type. The largest R_0 is seen for $x = 0.5$ which corresponds to the most mixed phase of the material.

The anomalous Hall effect is found to have a large contribution and on introduction of Co an immediate jump is seen between FeGe and $Fe_{1-x}Co_xGe$ $x = 0.1$. The AHE is found to peak in FeGe at 200 K and for $Fe_{1-x}Co_xGe$ the peak position in temperature decreases with T_c as x is increased.

The topological Hall measurements presented here are made under the presumption that a topological structure such as skyrmions are present. The $Fe_{1-x}Co_xGe$ range of material show the prerequisite behaviour found in other helimagnetic materials with chiral interactions producing a helical magnetic state that can be deformed, which have a region in which the skyrmion structure is stable. Using the methods applied to many other systems the results show a significant deviation between the measured Hall resistivity ρ_{xy} and the predicted Hall resistivity at low-fields which is attributed to the THE. In $Fe_{1-x}Co_xGe$ this effect was found to be large compared to FeGe, but on a similar scale to MnGe, However the expected skyrmion size is much larger for $Fe_{1-x}Co_xGe$ which would lead to an expected decrease in ρ_{xy}^{THE}. Nevertheless, unlike in MnGe and FeGe, in $Fe_{1-x}Co_xGe$ a low carrier density is observed and a potentially high degree of spin polarisation stemming from the half-metal like band structure recently calculated as $x \to 0.6$ [86] may explain additional sensitivity to any topological structures present.

From these results, it can be seen that $Fe_{1-x}Co_xGe$ presents a system rich in physical effects that can be tuned with composition.

CHAPTER 7

Conclusion

In this thesis we have studied the magnetic and magnetotransport property dependence for epitaxial B20 $Fe_{1-x}Co_xGe$ films by varying the Co content through x. To verify the samples grown would be suitable for study, the films were first characterised as shown in Chapter 4. First the method of growth was examined. MBE was chosen as it provided a suitable method of composition control and environment for producing high quality crystalline films. By varying the ratio of Fe to Co deposition rate, the whole range of $Fe_{1-x}Co_xGe$ was produced in steps of $x = 0.1$. RHEED was used during the growth procedure to monitor the crystal phase produced and LEED was used before and after to verify epitaxial growth, both methods verified the presence of the B20 phase. By monitoring the growth procedure we were able to enhance the quality of the films produced and the repeatability. TEM was used to directly view the sample lattice structure and we were able to view the chiral grain structure directly. Chiral grains sizes were found to remain approximately consistent from FeGe to $Fe_{0.5}Co_{0.5}Ge$ or $\sim$ 100-200 nm, although larger ones were present, indicating the growth requirements stayed consistent as x was varied. The B20 phase was confirmed by XRD indicating single phase films were able to be produced. These films were then measured using XRR and verified to be single homogeneous layers. The substrate/film and surface interfaces roughness were found to be approximately 1-2 nm which allowed later PNR measurements. From these findings we were satisfied the films grown were suitable for further magnetic and magnetotransport study which accomplished our first goal of producing B20 $Fe_{1-x}Co_xGe$ films.

The magnetic properties of these films are given in Chapter 5. We first identify the general magnetic properties by examining T_c and M_s as a function of composition. We find both of these to decrease with increasing x, indicating a reduction in magnetic interaction with a larger concentration of Co. From the $M(H)$ measurements we observe an easy-plane anisotropy that has been seen previously for FeGe [44]. The variation in magnetisation was examined for a range of FeGe film thickness and the characteristic change in inflection points was found to correspond with t_{film} indicating a change in the number of helix rotations contained as a function of film thickness. A direct comparison of the M_r/M_s ratio to t_{film} was unable to identify the helix wavelength as shown previously for MnSi [40]. For $0.1 \leq x \leq 1$ with constant t_{film} the shape of the $M(H)$ was found to vary, with a square loop forming at $Fe_{0.5}Co_{0.5}Ge$. This change in shape would be consistent with non-collinear FM state to FM, which we later found to be the

case. PNR was used to measure the magnetic depth profile of the $Fe_{1-x}Co_xGe$ films. We find, using a helicoid model that the magnetisation profiles found can be explained to have a helix structure and the wavelength was found to vary with the composition x. We also found a divergence of λ_h at $x_c = 0.5$ which was consistent with the change in $M(H)$ behaviour we had previously seen for $x = 0.5$. Although our resolution of $x = 0.1$ steps prevents us for determining the exact position, $x_c = 0.5$ is seen as the most likely. Using the relation of $\lambda_h \approx J/D$ we explain the changing λ_h is due to a variation in D as x is increased. After examining the magnetic properties we were satisfied that a helical magnetic structure was present and the discovery of a divergence in the helix wavelength was consistent with previous bulk crystal studies [29]. This result is also consistent with the neighbouring $Mn_{1-x}Fe_xGe$ where the divergence corresponded to a change in the sign of the DMI [30] which also has been shown theoretically [31]. From these results we have shown a study of the magnetic properties in $Fe_{1-x}Co_xGe$ and observe DMI is present in the system due to the helical magnetic structure.

The magnetotransport measurements are given in Chapter 6. We first look at the $\rho_{xx}(T)$ measurements where we observe all the compositions of $Fe_{1-x}Co_xGe$ to be metallic. For the intermediate compositions $0.2 \leq x \leq 0.7$ we observe a broad peak in the resistivity, ρ_{peak}, that was found to occur just below T_c. The origin of the ρ_{peak} was found to be magnetic and attributable to the B20 structure. The inflection points in $\rho_{xx}(T)$ were also later shown to describe different regions it AHE scaling. The MR at low-fields (below H_c) for $0 \leq x \leq 0.5$ was found to display M^2 scaling consistent with a conical giant magnetoresitance type model which was consistent with previous FeGe measurements [42]. The results are additional evidence for the helical structure present in these films. However for $0.8 \leq x \leq 0.8$ the same analysis could not be performed due to significant changes in the MR response. The Hall resistivity measurements showed a range of effects happening with increasing Co content. The ordinary Hall effect was found to increase with x to a peak at $x = 0.5$, before decreasing. A large increase in AHE is also seen on the introduction of Co. Finally the possible THE is explored for all values of x at 5 K and the temperature dependence up to 200 K for selected x. The THE extraction method used is consistent with what is reported in the literature and a low field discrepancy between the measured ρ_{xy} and the calculated ρ_{xy} is found. This difference is then explained as being produced by topological structures, such as skyrmions. In our results the values we find are larger than those previously seen in FeGe

and we find a discrepancy between the predicted theory and our experimental results. The values of ρ_{xy}^{THE} found for $0.1 < x < 0.8$ are found to peak at $x = 0.5$ with -0.39 $\mu\Omega$ cm, which is inconsistent if the idea of B_{eff} being at its weakest when $\lambda_{\mathrm{h}} \rightarrow \infty$. This forces us to question the applicability of this analysis to these intermediate compounds and conclude the THE measured using electrical transport requires complementary direct evidence to verify its topological origin. From these findings we are satisfied that the transport properties have been explored in $\mathrm{Fe}_{1-x}\mathrm{Co}_x\mathrm{Ge}$. This section shows the transport behaviour found in $\mathrm{Fe}_{1-x}\mathrm{Co}_x\mathrm{Ge}$ is consistent in many ways with FeGe but the changing composition and the resulting change in electronic and magnetic structure affects the properties significantly

7.1 Future outlook

The findings presented in the thesis have shown films of B20 $\mathrm{Fe}_{1-x}\mathrm{Co}_x\mathrm{Ge}$ offer a wide range of physical properties to be explored. However, many questions remain unanswered.

From the PNR results shown in Sect. 5.3.3, the identified divergence in the helix wavelength at $\mathrm{Fe}_{0.5}\mathrm{Co}_{0.5}\mathrm{Ge}$, is shown by a uniform magnetisation profile at close to zero-field. As we have measured in steps of $x = 0.1$, more samples could be grown at closer spaced intervals to more directly observe the change in wavelength and a more accurate divergence point. Also as we identified λ_{h} to lengthen as x is increased, thicker films could be grown ($t_{\mathrm{film}} \approx \lambda_{\mathrm{h}}$ for associated x value) and the PNR could be performed again to see if the ground state observed is consistent with previous FeGe measurements.

In Sect. 6.2 we presented the results of $\rho_{xx}(T)$ as a function of x. The observed data shows an unexpected peak in resistivity that spanned the range of x and occurred just below T_{c} for each film. We were able to confirm it had magnetic origins and was due to the B20 ordering, however it still requires more investigation.

At the time of writing, theoretical studies into $\mathrm{Fe}_{1-x}\mathrm{Co}_x\mathrm{Ge}$ have been performed in collaboration with this work [86]. The first principle calculations have been used calculate the magnetisation, OHE and AHE which agree remarkably well with the experimental results presented here. The DMI sign change is predicted at $x_c \sim 0.45$ which corresponds well with our measured value of $x_c = 0.5$. However the THE still remains elusive and the values measured experimentally are two orders of magnitude larger than the predicted values. However, despite these inconsistencies, the major result is that

the B20 $Fe_{1-x}Co_xGe$ system can be modelled accurately and the experimental results presented in this thesis have allowed the models for this B20 system to be tested. Future work from this point would be to attempt the direct observation of skyrmions in this material. By observing them directly, the THE evidence we have shown, could be unambiguously attributed to any topological structures present and may allow the discrepancy between experiment and theory to be uncovered.

$Fe_{1-x}Co_xGe$ remains an interesting material that poses many questions to be answered. The work presented here shows a systematic study into the production, characterisation and physical properties of $Fe_{1-x}Co_xGe$ films that hopefully fills the gap left in the literature surrounding the B20 TM silicides and germanides.

REFERENCES

[1] N. Nagaosa and Y. Tokura, Topological properties and dynamics of magnetic skyrmions, *Nature Nanotechnology* **8**, 899 (2013)

[2] A. Fert, V. Cros and J. Sampaio, Skyrmions on the track, *Nature Nanotech.* **8**, 152 (2013)

[3] H. J. Williams, J. H. Wernick, R. C. Sherwood and G. K. Wertheim, Magnetic Properties of the Monosilicides of Some 3 d Transition Elements, *Journal of Applied Physics* **37**, 1256 (1966)

[4] L. Lundgren, K. Blom and O. Beckman, Magnetic susceptibility measurements on cubic FeGe, *Physics Letters A* **28**, 175 (1968)

[5] R. Wäppling and L. Häggström, Mössbauer study of cubic FeGe, *Physics Letters A* **28**, 173 (1968)

[6] G. Wertheim, V. Jaccarino, J. Wernick, J. Seitchik, H. Williams et al., Unusual electronic properties of FeSi, *Physics Letters* **18**, 89 (1965)

[7] L. Lundgren, O. Beckman, V. Attia, S. P. Bhattacheriee and M. Richardson, Helical Spin Arrangement in Cubic FeGe, *Physica Scripta* **1**, 69 (1970)

[8] Y. Ishikawa, K. Tajima, D. Bloch and M. Roth, Helical spin structure in manganese silicide MnSi, *Solid State Communications* **19**, 525 (1976)

[9] T. Moriya, Anisotropic Superexchange Interaction and Weak Ferromagnetism, *Physical Review* **120**, 91 (1960)

[10] I. Dzyaloshinskii, Theory of helicoidal structures in antiferromagnets. 1. Nonmetals, *Soviet Physics JETP* **19**, 960 (1964)

[11] O. Nakanishi, A. Yanase, A. Hasegawa and M. Kataoka, The origin of the helical spin density wave in MnSi, *Solid State Communications* **35**, 995 (1980)

[12] P. Bak and M. H. Jensen, Theory of helical magnetic structures and phase transitions in MnSi and FeGe, *Journal of Physics C: Solid State Physics* **13**, L881 (1980)

[13] T. Ericsson, W. Karner, L. Häggström and K. Chandra, Magnetic Structure of Cubic FeGe, *Physica Scripta* **23**, 1118 (1981)

[14] G. Shirane, R. Cowley, C. Majkrzak, J. B. Sokoloff, B. Pagonis et al., Spiral magnetic correlation in cubic MnSi, *Physical Review B* **28**, 6251 (1983)

[15] M. L. Plumer and M. B. Walker, Wavevector and spin reorientation in MnSi, *Journal of Physics C: Solid State Physics* **14**, 4689 (1981)

[16] J. Beille, J. Voiron and M. Roth, Long period helimagnetism in the cubic B20 $Fe_xCo_{1-x}Si$ and $Co_xMn_{1-x}Si$ alloys, *Solid State Communications* **47**, 399 (1983)

[17] H. Takizawa, T. Sato, T. Endo and M. Shimada, High-pressure synthesis and electrical and magnetic properties of MnGe and CoGe with the cubic B20 structure, *Journal of Solid State Chemistry* **73**, 40 (1988)

[18] B. Lebech, J. Bernhard and T. Freltoft, Magnetic structures of cubic FeGe studied by small-angle neutron scattering, *Journal of Physics: Condensed Matter* **1**, 6105 (1989)

[19] M. L. Plumer, Wavevector and spin-flop transitions in cubic FeGe, *Journal of Physics: Condensed Matter* **2**, 7503 (1990)

[20] C. Gregory, *Magnetic properties of the Itinerant helimagnets MnSi and FeGe*, Ph.d., University of Durham (1992)

[21] S. Muhlbauer, B. Binz, F. Jonietz, C. Pfleiderer, A. Rosch et al., Skyrmion Lattice in a Chiral Magnet, *Science* **323**, 915 (2009)

[22] U. K. Rößler, a. N. Bogdanov and C. Pfleiderer, Spontaneous skyrmion ground states in magnetic metals, *Nature* **442**, 797 (2006)

[23] T. Skyrme, A unified field theory of mesons and baryons, *Nuclear Physics* **31**, 556 (1962)

[24] A. Bogdanov and D. Yablonshii, Thermodynamically stable "vortices" in magnetically ordered crystals. The mixed state of magnets, *Soviet Physics JETP* **68**, 101 (1989)

[25] A. Bogdanov and A. Hubert, Thermodynamically stable magnetic vortex states in magnetic crystals, *Journal of Magnetism and Magnetic Materials* **138**, 255 (1994)

[26] S. V. Grigoriev, S. V. Maleyev, A. I. Okorokov, Y. O. Chetverikov, P. Böni et al., Magnetic structure of MnSi under an applied field probed by polarized small-angle neutron scattering, *Physical Review B* **74**, 214414 (2006)

[27] S. Grigoriev, V. Dyadkin, D. Menzel, J. Schoenes, Y. Chetverikov et al., Magnetic structure of $Fe_{1-x}Co_xSi$ in a magnetic field studied via small-angle polarized neutron diffraction, *Physical Review B* **76**, 224424 (2007)

[28] S. V. Grigoriev, D. Chernyshov, V. A. Dyadkin, V. Dmitriev, S. V. Maleyev et al., Crystal Handedness and Spin Helix Chirality in $Fe_{1-x}Co_xSi$, *Physical Review Letters* **102**, 037204 (2009)

[29] S. V. Grigoriev, S. A. Siegfried, E. V. Altynbayev, N. M. Potapova, V. Dyadkin et al., Flip of spin helix chirality and ferromagnetic state in $Fe_{1-x}Co_xGe$ compounds, *Physical Review B* **90**, 174414 (2014)

[30] K. Shibata, X. Z. Yu, T. Hara, D. Morikawa, N. Kanazawa et al., Towards control of the size and helicity of skyrmions in helimagnetic alloys by spin orbit coupling, *Nature Nanotechnology* **8**, 723 (2013)

[31] J. Gayles, F. Freimuth, T. Schena, G. Lani, P. Mavropoulos et al., Dzyaloshinskii-Moriya Interaction and Hall Effects in the Skyrmion Phase of $Mn_{1-x}Fe_xGe$, *Physical Review Letters* **115**, 036602 (2015)

[32] H. Yamada, K. Terao, H. Ohta and E. Kulatov, Electronic structure and magnetism of FeGe with B20-type structure, *Physica B: Condensed Matter* **329-333**, 1131 (2003)

[33] J. F. DiTusa, S. B. Zhang, K. Yamaura, Y. Xiong, J. C. Prestigiacomo et al., Magnetic, thermodynamic, and electrical transport properties of the noncentrosymmetric B20 germanides MnGe CoGe, *Physical Review B* **90**, 144404 (2014)

[34] M. Uchida, Real-Space Observation of Helical Spin Order, *Science* **311**, 359 (2006)

[35] X. Z. Yu, Y. Onose, N. Kanazawa, J. H. Park, J. H. Han et al., Real-space observation of a two-dimensional skyrmion crystal, *Nature* **465**, 901 (2010)

[36] P. Milde, D. Kohler, J. Seidel, L. M. Eng, A. Bauer et al., Unwinding of a Skyrmion Lattice by Magnetic Monopoles, *Science* **340**, 1076 (2013)

[37] S. L. Zhang, A. Bauer, D. M. Burn, P. Milde, E. Neuber et al., Multidomain Skyrmion Lattice State in Cu_2OSeO_3, *Nano Letters* **16**, 3285 (2016)

[38] E. Karhu, S. Kahwaji, T. L. Monchesky, C. Parsons, M. D. Robertson et al., Structure and magnetic properties of MnSi epitaxial thin films, *Physical Review B* **82**, 184417 (2010)

[39] E. A. Karhu, S. Kahwaji, M. D. Robertson, H. Fritzsche, B. J. Kirby et al., Helical magnetic order in MnSi thin films, *Physical Review B* **84**, 060404 (2011)

[40] E. A. Karhu, U. K. Rößler, a. N. Bogdanov, S. Kahwaji, B. J. Kirby et al., Chiral modulations and reorientation effects in MnSi thin films, *Physical Review B* **85**, 094429 (2012)

[41] S. X. Huang and C. L. Chien, Extended Skyrmion Phase in Epitaxial FeGe(111) Thin Films, *Physical Review Letters* **108**, 267201 (2012)

[42] N. A. Porter, J. C. Gartside and C. H. Marrows, Scattering mechanisms in textured FeGe thin films: Magnetoresistance and the anomalous Hall effect, *Physical Review B* **90**, 024403 (2014)

[43] J. C. Gallagher, K. Y. Meng, J. T. Brangham, H. L. Wang, B. D. Esser et al., Robust Zero-Field Skyrmion Formation in FeGe Epitaxial Thin Films, *Physical Review Letters* **118**, 1 (2017)

[44] N. A. Porter, C. S. Spencer, R. C. Temple, C. J. Kinane, T. R. Charlton et al., Manipulation of the spin helix in FeGe thin films and FeGe/Fe multilayers, *Physical Review B* **92**, 1 (2015)

[45] S. L. Zhang, I. Stasinopoulos, T. Lancaster, F. Xiao, A. Bauer et al., Room-temperature helimagnetism in FeGe thin films, *Scientific Reports* **7**, 123 (2017)

[46] N. Kanazawa, *Charge and Heat Transport Phenomena in Electronic and Spin Structures in B20-type Compounds*, Ph.d., Tokyo (2015)

[47] A. Neubauer, C. Pfleiderer, B. Binz, A. Rosch, R. Ritz et al., Topological Hall Effect in the A Phase of MnSi, *Physical Review Letters* **102**, 186602 (2009)

[48] H. Wilhelm, M. Baenitz, M. Schmidt, U. K. Rößler, A. A. Leonov et al., Precursor Phenomena at the Magnetic Ordering of the Cubic Helimagnet FeGe, *Physical Review Letters* **107**, 127203 (2011)

[49] Y. Onose, Y. Okamura, S. Seki, S. Ishiwata and Y. Tokura, Observation of Magnetic Excitations of Skyrmion Crystal in a Helimagnetic Insulator Cu_{2}OSeO_{3}, *Physical Review Letters* **109**, 037603 (2012)

[50] X. Yu, N. Kanazawa, W. Zhang, T. Nagai, T. Hara et al., Skyrmion flow near room temperature in an ultralow current density, *Nature Communications* **3**, 988 (2012)

[51] A. B. Butenko, A. A. Leonov, U. K. Rößler and A. N. Bogdanov, Stabilization of skyrmion textures by uniaxial distortions in noncentrosymmetric cubic helimagnets, *Physical Review B* **82**, 052403 (2010)

[52] M. N. Wilson, A. B. Butenko, A. N. Bogdanov and T. L. Monchesky, Chiral skyrmions in cubic helimagnet films: The role of uniaxial anisotropy, *Physical Review B* **89**, 094411 (2014)

[53] N. A. Porter, G. L. Creeth and C. H. Marrows, Magnetoresistance in polycrystalline and epitaxial $Fe_{1-x}Co_xSi$ thin films, *Physical Review B.* **86**, 064423 (2012)

[54] F. N. Rybakov, A. B. Borisov, S. Blügel and N. S. Kiselev, New Type of Stable Particlelike States in Chiral Magnets, *Physical Review Letters* **115**, 117201 (2015)

[55] M. N. Wilson, E. A. Karhu, D. P. Lake, A. S. Quigley, S. Meynell et al., Discrete helicoidal states in chiral magnetic thin films, *Physical Review B* **88**, 214420 (2013)

[56] E. A. Karhu, *Structural and Magnetic Properties of Epitaxial MnSi(111) Thin Films*, Ph.d., Dalhousie University, Halifax, Nova Scotia (2012)

[57] J. Als-Nielsen and D. McMorrow, *Elements of modern X-ray physics*, John Wiley & Sons, Ltd, second edi edition (2011)

[58] M. Björck and G. Andersson, GenX : an extensible X-ray reflectivity refinement program utilizing differential evolution, *Journal of Applied Crystallography* **40**, 1174 (2007)

[59] L. G. Parratt, Surface Studies of Solids by Total Reflection of X-Rays, *Physics Review* **95**, 359 (1954)

[60] V. A. Ukleev, N. A. Grigoryeva, E. A. Dyadkina, A. A. Vorobiev, D. Lott et al., Magnetic properties of the $SiO_2(Co)/GaAs$ interface: Polarized neutron reflectometry and SQUID magnetometry, *Physical Review B.* **86**, 134424 (2012)

[61] W. S. Rasband and K. W. Eliceiri, NIH Image to ImageJ: 25 years of image analysis, *Nature Methods* **9**, 671 (2012)

[62] S. M. Stishov, A. E. Petrova, S. Khasanov, G. K. Panova, A. A. Shikov et al., Magnetic phase transition in the itinerant helimagnet MnSi: Thermodynamic and transport properties, *Phys. Rev. B* **76**, 052405 (2007)

[63] L. J. Van der Pauw, A method of measuring specific resistivity and Hall effect of discs of arbitrary shape, *Phillips Research Reports* **13**, 1 (1958)

[64] A. I. Arbab, Drude, Hall and Maximal Conductivities: A Unified Complex Model, *Journal of Modern Physics* **03**, 1040 (2012)

[65] N. A. Porter, P. Sinha, M. B. Ward, A. N. Dobrynin, R. M. D. Brydson et al., Giant topological Hall effect in strained $Fe_{0.7}Co_{0.3}Si$ epilayers, arXiv:1312.1722 (2013)

[66] Q. Zhang, M. Tanaka, M. Takeguchi and K. Furuya, Analytical UHV transmission electron microscopy studies of electronic structure changes between as-deposited Mn and Mn silicide on Si(111) surface, *Surface Science* **507-510**, 453 (2002)

[67] T. B. Massalski, H. Okamoto, P. Subramanian and L. Kacprzak, Binary alloy phase diagrams. vol. 3, *ASM International* p. 1704 (1990)

[68] S. Hasegawa, *Reflection High-Energy Electron Diffraction*, John Wiley & Sons, Inc. (2002)

[69] M. M. R. Evans, J. C. Glueckstein and J. Nogami, Epitaxial growth of manganese on silicon: Volmer-Weber growth on the Si(111) surface, *Physical Review B* **53**, 4000 (1996)

[70] W. Kraus and G. Nolze, POWDER CELL a program for the representation and manipulation of crystal structures and calculation of the resulting X-ray powder patterns, *Journal of Applied Crystallography* **29**, 301 (1996)

[71] A. R. Denton and N. W. Ashcroft, Vegard's law, *Physical Review A* **43**, 3161 (1991)

[72] S. V. Maleyev, Cubic magnets with Dzyaloshinskii-Moriya interaction at low temperature, *Physical Review B* **73**, 174402 (2006)

[73] S.-a. Siegfried, *Chirality effects in transition metal monogermanides and -silicides*, Ph.d., University of Hamburg (2016)

[74] N. Kanazawa, Y. Onose, T. Arima, D. Okuyama, K. Ohoyama et al., Large Topological Hall Effect in a Short-Period Helimagnet MnGe, *Physical Review Letters* **106**, 156603 (2011)

[75] N. Kanazawa, K. Shibata and Y. Tokura, Variation of spinâ€"orbit coupling and related properties in skyrmionic system $Mn_{1-x}Fe_xGe$, *New Journal of Physics* **18**, 045006 (2016)

[76] P. Sinha, N. A. Porter and C. H. Marrows, Strain-induced effects on the magnetic and electronic properties of epitaxial $Fe_{1-x}Co_xSi$ thin films, *Physical Review B* **89**, 134426 (2014)

[77] N. Kanazawa, M. Kubota, A. Tsukazaki, Y. Kozuka, K. S. Takahashi et al., Discretized topological Hall effect emerging from skyrmions in constricted geometry, *Physical Review B* **91**, 041122 (2015)

[78] N. Kanazawa, Y. Onose, Y. Shiomi, S. Ishiwata and Y. Tokura, Band-filling dependence of thermoelectric properties in B20-type CoGe, *Applied Physics Letters* **100**, 9 (2012)

[79] P. Sinha, *Highly Spin-Polarised Chiral Transition Metal Silicide Epilayers*, Ph.d., University of Leeds (2015)

[80] M. E. Fisher and J. S. Langer, Resistive anomalies at magnetic critical points, *Phys. Rev. Lett.* **20**, 665 (1968)

[81] A. Bauer, M. Garst and C. Pfleiderer, Specific Heat of the Skyrmion Lattice Phase and Field-Induced Tricritical Point in MnSi, *Phys. Rev. Lett.* **110**, 177207 (2013)

[82] Y. Suezaki and H. Mori, Dynamic Critical Phenomena in Magnetic Systems. II, *Prog. Theor. Phys.* **41**, 1177 (1969)

[83] J. Stankiewicz, J. Bartolomé and D. Fruchart, Spin Disorder Scattering in Magnetic Metallic Alloys, *Physical Review Letters* **89**, 106602 (2002)

[84] J. Guevara, V. Vildosola, J. Milano and A. M. Llois, Half-metallic character and electronic properties of inverse magnetoresistant $Fe_{1-x}Co_xSi$ alloys, *Physical Review B* **69**, 184422 (2004)

[85] Y. Onose, N. Takeshita, C. Terakura, H. Takagi and Y. Tokura, Doping dependence of transport properties in $Fe_{1-x}Co_xSi$, *Phys. Rev. B* **72**, 224431 (2005)

[86] C. S. Spencer, J. Gayles, N. A. Porter, S. Sugimoto, Z. Aslam et al., Helical magnetic structure and the anomalous and topological Hall effects in epitaxial B20 $Fe_{1-x}Co_xGe$ films, arXiv:1803.03281 (2018)

[87] N. Nagaosa, J. Sinova, S. Onoda, a. H. MacDonald and N. P. Ong, Anomalous Hall effect, *Reviews of Modern Physics* **82**, 1539 (2010)

[88] R. Ritz, M. Halder, C. Franz, A. Bauer, M. Wagner et al., Giant generic topological Hall resistivity of MnSi under pressure, *Physical Review B* **87**, 134424 (2013)

[89] Y. Li, N. Kanazawa, X. Z. Yu, A. Tsukazaki, M. Kawasaki et al., Robust Formation of Skyrmions and Topological Hall Effect Anomaly in Epitaxial Thin Films of MnSi, *Physical Review Letters* **110**, 117202 (2013)

[90] T. Yokouchi, N. Kanazawa, A. Tsukazaki, Y. Kozuka, M. Kawasaki et al., Stability of two-dimensional skyrmions in thin films of $Mn_{1-x}Fe_xSi$ investigated by the topological Hall effect, *Physical Review B* **89**, 064416 (2014)

[91] S. A. Meynell, M. N. Wilson, J. C. Loudon, A. Spitzig, F. N. Rybakov et al., Hall effect and transmission electron microscopy of epitaxial MnSi thin films, *Physical Review B* **90**, 224419 (2014)

[92] V. A. Dyadkin, S. V. Grigoriev, D. Menzel, D. Chernyshov, V. Dmitriev et al., Control of chirality of transition-metal monosilicides by the Czochralski method, *Physical Review B* **84**, 014435 (2011)